COS-Weak: Probing the CGM using analogs of weak Mg II absorbers at $z < 0.3$

S. Muzahid[1,2]⋆, G. Fonseca[1,3], A. Roberts[1,4], B. Rosenwasser[1,5], P. Richter[6,7], A. Narayanan[8], C. Churchill[9], and J. Charlton[1],

[1] *Department of Astronomy & Astrophysics, The Pennsylvania State University, 525 Davey Lab, University Park, State College, PA 16802, USA*
[2] *Leiden Observatory, Leiden University, PO Box 9513, NL-2300 RA Leiden, the Netherlands*
[3] *Department of Physics, University of Connecticut, Storrs, CT 06269, USA*
[4] *Departamento de Astronomía, Universidad de Chile, Camino del Observatorio 1515, Las Condes, Santiago, Chile*
[5] *Department of Astronomy, University of Wisconsin-Madison, 475 N. Charter Street, Madison, WI 53706, USA*
[6] *Institut für Physik und Astronomie, Universität Potsdam, Haus 28, Karl-Liebknecht-Str. 24/25, 14476 Golm (Potsdam), Germany*
[7] *Leibniz-Institute for Astrophysics Potsdam (AIP), An der Sternwarte 16, D-14482 Potsdam, Germany*
[8] *Indian Institute of Space Science and Technology, Thiruvananthapuram 695547, Kerala, India*
[9] *Department of Astronomy, New Mexico State University, Las Cruces, NM 88003, USA*

ABSTRACT

We present a sample of 34 weak metal line absorbers at $z < 0.3$ selected by the simultaneous $> 3\sigma$ detections of the Si IIλ1260 and C IIλ1334 absorption lines, with $W_r(\text{Si II}) < 0.2$ Å and $W_r(\text{C II}) < 0.3$ Å, in archival HST/COS spectra. Our sample increases the number of known low-z "weak absorbers" by a factor of > 5. The column densities of H I and low-ionization metal lines obtained from Voigt profile fitting are used to build simple photoionization models. The inferred densities and line of sight thicknesses of the absorbers are in the ranges of $-3.3 < \log n_H/\text{cm}^{-3} < -2.4$ and ~1 pc – 50 kpc (median ≈ 500 pc), respectively. Most importantly, 85% (50%) of these absorbers show a metallicity of [Si/H] > -1.0 (0.0). The fraction of systems showing near-/super-solar metallicity in our sample is significantly higher than in the H I-selected sample (Wotta et al. 2016) and the galaxy-selected sample (Prochaska et al. 2017) of absorbers probing the circum-galactic medium at similar redshift. A search for galaxies has revealed a significant galaxy-overdensity around these weak absorbers compared to random positions with a median impact parameter of 166 kpc from the nearest galaxy. Moreover, we find the presence of multiple galaxies in ≈ 80% of the cases, suggesting group environments. The observed $d\mathcal{N}/dz$ of 0.8 ± 0.2 indicates that such metal-enriched, compact, dense structures are ubiquitous in the halos of low-z group galaxies. We suggest that these are transient structures that are related to galactic outflows and/or stripping of metal-rich gas from galaxies.

Key words: galaxies: formation – galaxies: haloes – quasar: absorption line

1 INTRODUCTION

Metal absorption lines detected in quasar spectra are thought to arise from the circum-galactic medium (CGM) of intervening galaxies close to the lines of sight (e.g., Bergeron 1986; Bergeron & Boissé 1991; Steidel & Sargent 1992; Adelberger et al. 2005; Kacprzak et al. 2008, 2015; Chen & Mulchaey 2009; Steidel et al. 2010; Stocke et al. 2013; Werk et al. 2013; Bordoloi et al. 2014; Turner et al. 2014; Johnson et al. 2015; Keeney et al. 2017). The absorption strength of a metal line depends primarily on the metallicity and on the ionization parameter of the absorbing gas. The metallicity of an absorber is an important diagnostic of the physical processes at play. For example, high metallicity gas is likely to observe in galactic outflows (Tripp et al. 2011; Muzahid 2014; Muzahid et al. 2015b), whereas the gas infalling from the inter-galactic medium (IGM) on to a galaxy halo is expected to be metal-poor (Ribaudo et al. 2011; Churchill et al. 2012; Kacprzak et al. 2012a). The ionization parameter, usually determined from the ratio of two consecutive ionic

states of the same element, provides the density of the absorbing gas, provided the intensity of the incident radiation is known. It is generally assumed that the extra-galactic ultraviolet (UV) background radiation (UVB; Haardt & Madau 1996, 2012; Khaire & Srianand 2015a) prevails in the CGM of a $\sim L_*$ galaxy at impact parameters greater than several tens of kpc (Werk et al. 2014; Narayanan et al. 2010). The relative abundances of heavy elements in an absorption system provide important clues regarding the star formation history and the initial mass function of the host-galaxy (Pettini et al. 1999, 2002; Becker et al. 2012; Zahedy et al. 2017). Metal lines are, thus, essential for determining the physical conditions of the otherwise invisible, diffuse gas in the CGM and for inferring the physical processes that determine the evolution of a galaxy.

The rest-frame wavelengths of the Mg II $\lambda\lambda$2796,2803 doublet transitions are such that it is easily observable using ground based optical telescopes for a wide redshift range ($0.3 \lesssim z \lesssim 2.5$). Consequently, Mg II absorbers have been studied for the last couple of decades by a significant number of authors (e.g., Lanzetta et al. 1987; Petitjean & Bergeron 1990; Steidel & Sargent 1992; Charlton & Churchill 1998; Churchill et al. 1999, 2003; Rigby et al. 2002; Nestor et al. 2005; Kacprzak et al. 2008;

⋆ E-mail: sowgat@strw.leidenuniv.nl

Chen et al. 2010; Zhu & Ménard 2013; Nielsen et al. 2013a,b; Joshi et al. 2017; Dutta et al. 2017, and references therein). In addition, recent infrared surveys have identified Mg II absorbers all the way up to $z \approx 7$ (Matejek & Simcoe 2012; Chen et al. 2016; Bosman et al. 2017; Codoreanu et al. 2017). In all these studies, Mg II absorbers are found to probe a wide variety of astrophysical environments. Based on the rest-frame equivalent width of the $\lambda 2796$ transition (W_r^{2796}) Mg II absorbers are historically classified into weak ($W_r^{2796} < 0.3$ Å) and strong ($W_r^{2796} \geqslant 0.3$ Å) groups. The strong absorbers are sometimes categorized into very strong ($W_r^{2796} \geqslant 1$ Å) and ultrastrong ($W_r^{2796} \geqslant 3$ Å) systems (Nestor et al. 2005, 2007). The very strong/ultrastrong Mg II absorbers are generally found to be associated with luminous galaxies ($L \gtrsim 0.1 L_*$). They often show velocities spread over several hundreds of km s^{-1} and hence are thought to be related to galactic superwind driven by supernova and/or starburst (e.g., Bond et al. 2001; Prochter et al. 2006; Zibetti et al. 2007, but see Gauthier (2013) for an alternate scenario).

In a detailed study of the Mg II absorbing CGM, Nielsen et al. (2013b) have found a covering fraction (C_f) of 60–100% (15–40%) for systems with $W_r^{2796} > 0.1$ Å ($W_r^{2796} > 1.0$ Å) out to 100 kpc. The C_f does not change significantly with the host-galaxy's color and/or luminosity (see also Werk et al. 2013). However, a bimodality in the azimuthal angle distribution of Mg II absorbing galaxies has been reported in the literature, such that the gas is preferentially detected near the projected major and minor axes of star-forming galaxies (Kacprzak et al. 2012b; Bouché et al. 2012). Galaxies with little star-formation do not show any such preference. The observed bimodality is thought to be driven by gas accreted along the major axis and outflowing along the minor axis.

The weak absorbers with $W_r^{2796} < 0.3$ Å, that are distinct from the strong population in several aspects (e.g. Rigby et al. 2002), are of particular interest in this paper. The first systematic survey of weak Mg II absorbers was conducted by Churchill et al. (1999) in the redshift range $0.4 < z < 1.4$ using HIRES/Keck spectra. They found that the number of weak absorbers per unit redshift of $dN/dz \approx 1.74 \pm 0.10$ is ≈ 4 times higher than that of the Lyman Limit Systems (LLSs) which have neutral hydrogen column density $N(\text{H I}) > 10^{17.2}$ cm^{-2}. Therefore it is suggested that a vast majority of the weak Mg II absorbers must arise in sub-LLS environments. The evolution of the dN/dz for the weak absorbers shows a peak at $z = 1.2$ (Narayanan et al. 2005, 2007) which was thought to be connected with the evolution of the cosmic star-formation rate density of dwarf galaxies (see also Fig. 9 of Mathes et al. 2017). However, in a recent survey, Codoreanu et al. (2017) have found that the dN/dz of 1.35 ± 0.58 for the weak absorbers with $0.1 < W_r < 0.3$ Å at $z \approx 2.3$, increases to 2.58 ± 0.67 by $z \approx 4.8$ (see also Bosman et al. 2017). The number of weak absorbers exceeds the number expected from an exponential fit to strong systems with $W_r^{2796} > 0.3$ Å. The dN/dz at these high redshifts, however, is consistent with cosmological evolution of the population, suggesting that the processes responsible for weak absorbers are already in place within the first 1 Gyr of cosmic history. One of the most intriguing properties of the weak absorbers is that, in most cases, they exhibit near-solar to super-solar metallicities (Rigby et al. 2002; Lynch & Charlton 2007; Misawa et al. 2008; Narayanan et al. 2008) in spite of the fact that luminous galaxies are rarely found within a ~50 kpc impact parameter (Churchill et al. 2005; Milutinović et al. 2006). Studying weak absorbers at low-z ($z \approx 0.1$) is advantageous since it is relatively easy to search for the host-galaxies.

Because of the atmospheric cutoff of optical light, a direct search for the Mg II doublet at $z < 0.3$ is not viable. Instead,

Narayanan et al. (2005), for the first time, used weak Si II $\lambda 1260$ ($W_r^{1260} < 0.2$ Å) and C II $\lambda 1334$ ($W_r^{1334} < 0.3$ Å) lines as proxies for the weak Mg II absorbers. Both Si_{14}^{28} and Mg_{12}^{24} are α-process elements. The creation and destruction ionization potentials of Si II (i.e., 8.1 and 16.3 eV, respectively) are very similar to Mg II (i.e., 7.6 and 15.0 eV, respectively). The abundance of Si in the solar neighborhood (i.e., [Si/H] = -4.49) is also very similar to that of Mg, i.e., [Mg/H] = -4.40 (Asplund et al. 2009). All these facts indicate that Si II and Mg II arise from the same gas phase and Si II is a good proxy for Mg II (see also Narayanan et al. 2005; Herenz et al. 2013). In Appendix A we have shown that the weak metal line absorbers studied here are indeed analogous to the known weak Mg II absorbers based on our model predicted Mg II column densities.

The only known previous systematic survey for weak absorbers at low-z was conducted by Narayanan et al. (2005). They searched for weak Si II $\lambda 1260$ and C II $\lambda 1334$ absorbers in high resolution *HST* STIS Echelle spectra of 25 quasars. They found only six weak Mg II analog absorbers over a redshift pathlength of $\Delta z \approx 5.3$. Their estimated dN/dz of ≈ 1.0 is consistent with cosmological evolution of the population. By considering the effect of the change in the UVB on an otherwise static absorbing gas, their photoionization models suggested that the low-z weak Mg II population is likely composed of both kiloparsec-scale, low density structures that only gave rise to C IV absorption at $z \approx 1$ and parsec-scale, higher density structures that produced weak Mg II absorption at $z \approx 1$. Clearly the constancy of dN/dz need not necessarily suggest the same physical origin for the population at different redshifts, and it warrants a detailed ionization modelling of the absorbers.

In this paper we have studied weak Mg II absorber analogs detected in *HST*/COS spectra via the Si II $\lambda 1260$ and C II $\lambda 1334$ transitions. With 34 absorbers in total, here we present the first-ever statistically significant sample of weak absorbers at low-z. The paper is organized as follows: In Section 2 we provide the details of the observations, data reduction, absorber search techniques, and absorption line measurements. In Section 3 we present our analysis which includes estimating dN/dz, measuring H I and ionic column densities, and building photoionization models. The main results based on the ionization models are presented in Section 4. In Section 5 we discuss our main results, followed by a summary in Section 6. Throughout this study we adopt a flat ΛCDM cosmology with $H_0 = 71$ km s^{-1} Mpc^{-1}, $\Omega_M = 0.3$, $\Omega_\Lambda = 0.7$, and $\Omega_b h^2 = 0.02$. Abundances of heavy elements are given in the notation [X/Y] = log(X/Y) $-$ log(X/Y)$_\odot$ with solar relative abundances taken from Asplund et al. (2009). All distances given are in physical units.

2 DATA

2.1 Observations and data reduction

We have searched for weak Mg II analogs in 363 medium resolution, far-UV (FUV) spectra of active galactic nuclei (AGN)/quasars (QSOs) observed with the *Hubble Space Telescope*/Cosmic Origins Spectrograph (*HST*/COS). These spectra were available in the public *HST* archive before February, 2016. Note that all these spectra were obtained under programs prior to the *HST* Cycle-22. The properties of COS and its in-flight operations are discussed in Osterman et al. (2011) and Green et al. (2012). We have used only spectra that were obtained with the medium resolution ($R \approx 20000$) FUV COS gratings (i.e. G130M and/or G160M). The data were retrieved from the *HST* archive and reduced using CALCOS
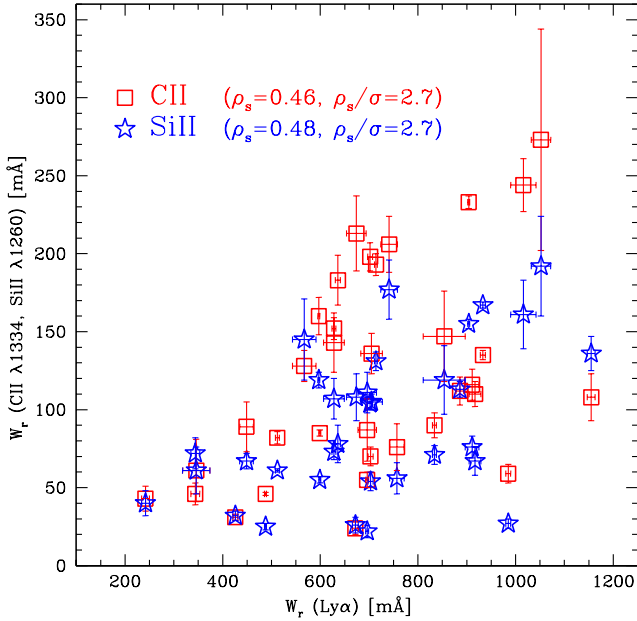
Figure 1. The rest-frame equivalent widths of the low-ionization metal lines (C II and Si II) against $W_r(\text{Ly}\alpha)$. All the "weak" absorbers have $W_r(\text{Si II } \lambda1260) < 200$ mÅ and $W_r(\text{C II } \lambda1334) < 300$ mÅ by design. A mild 2.7σ correlation between $W_r(\text{C II, Si II})$ and $W_r(\text{Ly}\alpha)$ is present. An upper envelope with an apparent lack of data points in the upper-left corner (i.e. the region with $W_r(\text{Ly}\alpha) < 600$ mÅ and $W_r(\text{C II, Si II}) > 100$ mÅ) is evident.
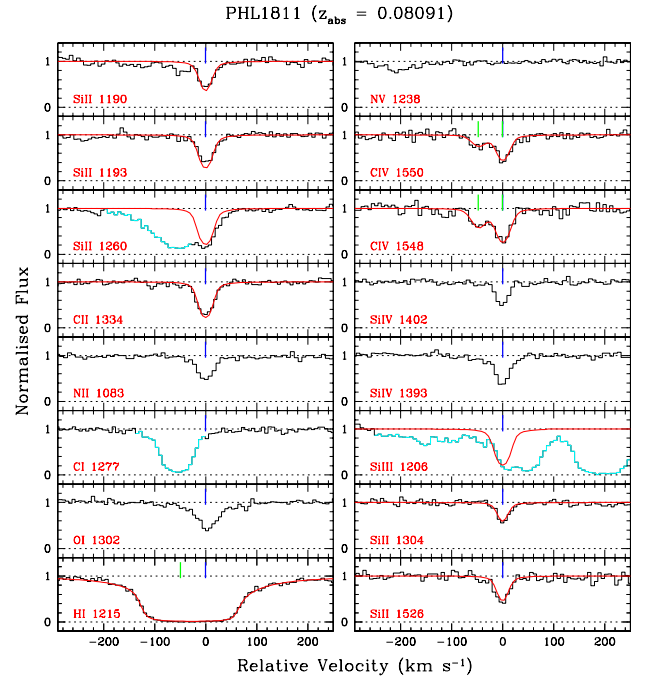

Figure 2. Velocity plot of a weak absorber at $z_{\text{abs}} = 0.08091$ detected towards PHL1811. The smooth solid red curves over-plotted on top of data (black histogram) are the best fitting model profiles. Unrelated absorption lines are shown in cyan. Since the Si III line is blended with the Galactic Si II$\lambda1304$ line, we have generated a synthetic profile corresponding to the maximum allowed column density. Single component C II and Si II lines are detected at ~ 0 km s^{-1}. The C IV absorption shows another component at ~ -50 km s^{-1}. Both the C IV and Lyα lines are fitted with two Voigt profile components. The line centroids of the individual components are marked by the vertical ticks in each panel. Velocity plots, Voigt profile fits, and comments about each absorbers can be found in Appendix C as online material.

pipeline software. The pipeline reduced data ('*x1d*' files) were flux calibrated. The individual exposures were aligned and co-added using the IDL code ('*coadd_x1d*'), developed by Danforth et al. (2010) and subsequently improved by Keeney et al. (2012) and Danforth et al. (2016), in order to increase the spectral signal-to-noise ratio (S/N). The final co-added spectra typically have spectral coverage of ≈ 1150–1450 Å for the G130M grating and ≈ 1450–1800 Å for the G160M grating. Since these archival spectra come from various different observing programs, they show a wide range in S/N (i.e., 2–60 per resolution element). In our analysis, we do not include 67 spectra that show S/N < 5 per resolution element over most of it spectral coverage. The details of the remaining 296 spectra used in this study are given in Table B1. There are 174 spectra with data from both the G130M and G160M gratings, 114 spectra with only G130M grating data, and 8 spectra with only G160M grating data. The median S/N of the 288 G130M grating spectra is 9 per resolution element. The median S/N of the 182 G160M grating spectra is 7 per resolution element. In Table B2 we list the 67 spectra that are available in the archive but are not used in this study due to poor S/N (i.e. < 5 per resolution element). The COS FUV spectra are highly oversampled with 6 raw pixels per resolution element. We, thus, binned the spectra by three pixels. All our measurements and analyses are performed on the binned data. We note that while the binning improves S/N per pixel by a factor of $\sqrt{3}$, it does not affect the absorption line measurements (i.e. W_r and N). For each spectrum continuum normalization was done by fitting the line-free regions with smooth low-order polynomials.

2.2 Search techniques and the sample

Our search for the weak absorbers relies on the simultaneous presence of the Si II$\lambda1260$ and C II$\lambda1334$ lines. Note that the presence of C II$\lambda1334$ restricts our survey to a maximum redshift of $z_{\text{max}} \approx 0.35$. First, we assume every detected absorption in a spectrum above $\lambda_{\text{obs}} > 1260$ Å is due to the Si II$\lambda1260$ line from redshift $z_{\text{abs}} = (\lambda_{\text{obs}}/\lambda_{\text{rest}}) - 1$, where λ_{rest} is the rest-frame wavelength of the Si II$\lambda1260$ transition [1]. Next we check for the presence of the corresponding C II$\lambda1334$ line using the z_{abs}. We build a "primary" list of absorbers using each of the identified coincidence. We then check for the presence of other common transitions (e.g., Lyα, Si II$\lambda1193$, C II$\lambda1036$, Si III). Since some amount of neutral hydrogen is expected to be associated with these weak low-ionization absorbers, we have excluded any "primary" system that does not exhibit any detectable Lyα absorption. The presence of other metal lines would depend on the phase structure, ionization parameter, and metallicity of the absorber. We, therefore, do not impose the detection of any other metal line as a necessary criterion to confirm a weak absorber. Next, we investigate if the identified Si II$\lambda1260$ and/or C II$\lambda1334$ lines can have any other identity (i.e. other lines from other redshifts). We include a system in our "secondary" list when both the lines are free from significant contamination.

---

[1] In this work, λ_{rest} and oscillator strengths f_{osc} of different lines are taken from Morton (2003)

Table 1. List of 34 weak Mg II analogs.

QSO	RA (J2000)	Dec (J2000)	z_{qso}	z_{abs}	Gratings	(S/N) (G130M)	(S/N) (G160M)	W_r(mÅ) Lyα	C II	Si II	Flag	PID
(1)	(2)	(3)	(4)	(5)	(6)	(7)	(8)	(9)	(10)	(11)	(12)	(13)
PG0003+158	1.49683	16.16361	0.451	0.16512	3	15	9	696±3	55± 5	22± 4	1	12038
Q0107-025A	17.55475	-2.33136	0.960	0.22722	3	10	12	696±19	87±20	111±13	1	11585
HE0153-4520	28.80500	-45.10333	0.451	0.22597	3	20	13	628±4	152±7	73±5	1	11541
3C57	30.48817	-11.54253	0.670	0.32338	3	17	10	636±5	183±16	78±12	1	12038
SDSSJ0212-0737	33.07633	-7.62217	0.174	0.01603	3	7	4	1016±26	244±17	161±22	0	12248
SDSSJ0212-0737	33.07633	-7.62217	0.174	0.13422	3	7	4	449±14	89±16	67±5	0	12248
UKS-0242-724^a	40.79000	-72.28011	0.102	0.06376	3	11	8	886±8	112±9	113±5	1	12263
Q0349-146	57.86900	-14.48556	0.616	0.07256	3	10	6	1155±8	108±15	136±11	0	13398
PKS0405-123	61.95180	-12.19344	0.573	0.16710	3	50	22	904±2	233±4	155±3	1	11508/11541
IRAS-F04250-5718	66.50321	-57.20031	0.104	0.00369	3	40	22	488±2	46±1	25±2	1	11686/11692
FBQS-0751+2919	117.80129	29.32733	0.916	0.20399	3	23	23	702±5	198±9	104±4	1	11741
VV2006J0808+0514	122.16187	5.24444	0.360	0.02930	1	5	–	741±17	206±18	177±19	0	12603
PG0832+251	128.89917	24.99472	0.329	0.02811	3	7	8	344±9	46±7	72±10	1	12025
SDSSJ0929+4644	142.29080	46.74000	0.240	0.06498	3	11	6	242±8	43±8	40±8	0	12248
PMNJ1103-2329	165.90667	-23.49167	0.186	0.08352	3	9	6	917±12	110±8	67±9	1	12025
PG1116+215	169.78583	21.32167	0.176	0.13850	3	25	18	512±4	82±4	61±1	1	12038
SDSSJ1122+5755	170.68704	57.92861	0.906	0.05319	3	5	4	346±28	61±20	61±15	0	12248
PG1121+422	171.16324	42.02917	0.225	0.19238	3	11	7	705±22	136±13	105±5	1	12024
3C263	174.98746	65.79700	0.646	0.06350	3	23	17	985±5	59±6	27±3	1	11541
PG1202+281	181.17599	27.90331	0.165	0.13988	3	4	6	757±15	76±15	56±10	0	12248
PG-1206+459	182.24171	45.67653	1.163	0.21439	3	16	17	597±2	160±12	119±5	1	11741
SDSSJ1210+3157	182.65650	31.95167	0.389	0.05974	3	5	5	567±24	128±10	145±26	0	12248
SDSSJ1210+3157	182.65650	31.95167	0.389	0.14964	3	5	5	674±20	213±24	108±15	0	12248
SDSSJ1214+0825^a	183.62729	8.41892	0.585	0.07407	1	5	–	628±21	143±19	107±13	1	11698
RXJ1230.8+0115	187.70834	1.25597	0.117	0.00575	3	30	19	599±2	85±2	55±2	1	11686
PKS1302-102	196.38750	-10.55528	0.278	0.09495	3	18	11	703±5	70±6	54±6	1	12038
SDSSJ1322+4645	200.59450	46.75978	0.374	0.21451	3	5	4	1052±20	273±71	192±32	0	11598
SDSSJ1357+1704	209.30254	17.07892	0.150	0.09784	3	10	7	911±14	116±10	76±7	0	12248
SDSSJ1419+4207	214.79250	42.12969	0.873	0.17885	3	5	4	854±43	147±29	119±22	0	11598
PG1424+240	216.75163	23.80000	> 0.6	0.12126	3	14	12	672±6	24±4	26±5	1	12612
PG1424+240	216.75163	23.80000	> 0.6	0.14683	3	14	12	834±4	90±8	71±6	1	12612
PG-1630+377	248.00466	37.63055	1.479	0.17388	3	26	11	714±3	193±7	131±6	1	11741
PHL1811	328.75623	-9.37361	0.190	0.07774	3	25	14	426±5	31±2	32±3	1	12038
PHL1811	328.75623	-9.37361	0.190	0.08091	3	25	14	933±5	135±3	167±2	1	12038

Notes– (1) QSO name; (2) Right-ascension (J2000); (3) Declination (J2000); (4) QSO redshift from NED except for QSO PG1424+240, which is from Furniss et al. (2013); (5) Absorption redshift; (6) COS gratings used for observations, 1: G130M, 2: G160M, 3: G130M+160M; (7) S/N of the G130M data estimated near 1400 Å; (8) S/N of the G160M data estimated near 1600 Å (blank when data are not available); (9) Rest-frame equivalent width of Lyα in mÅ (10) Rest-frame equivalent width of C II λ1334 in mÅ (11) Rest-frame equivalent width of Si II λ1260 in mÅ (12) Spectrum flag, 1: part of the statistical sample, 0: not part of the statistical sample; (13) *HST* proposal ID. Besides these systems we found two tentative systems that are not part of this study. These are: (a) z_{abs} = 0.06206 towards QSO-B2356-309 in which Si II is noisy and barely detected at 3σ level. In addition, what would be the C IIλ1334 of this system has been identified as Lyα of z_{abs} = 0.1659 by Fang et al. (2014). (b) z_{abs} = 0.06206 towards Q2251+155 in which the profiles of C IIλ1334 and λ1036 are not consistent with each other and with the Si IIλ1260/λ1193 lines. ^{a}These systems are not used for photoionization model due to the lack of Si III coverage (see text).

For each absorber in the "secondary" list we measure rest-frame equivalent widths (W_r) of Si IIλ1260 and C IIλ1334 lines. We consider only systems in which both the lines are detected with $\geqslant$ 3σ significance. Next we impose the W_r threshold criteria so that each system in our final sample, listed in Table 1, has W_r(Si IIλ1260) < 200 mÅ and W_r(C IIλ1334) < 300 mÅ. The equivalent widths of the C II and Si II lines of our final sample are plotted against the W_r(Lyα) in Fig. 1. A mild correlation between the equivalent widths of low-ionization metal lines and Lyα is apparent. A Spearman rank correlation test suggests a correlation coefficient, ρ_s, of $\approx$ 0.47 with a 2.7σ significance. We notice an upper envelope in the figure which is likely due to a metallicity effect. In particular, the systems with W_r(Lyα) $\lesssim$ 600 mÅ would require unreasonably high metallicities in order to produce Si II and/or C II absorption with W_r $\gtrsim$ 100 mÅ. The systems with W_r(Lyα) > 600 mÅ, on the other hand, show a wide range in Si II and C II equivalent widths. This could be because of poor small scale metal mixing so that the observed H I

need not entirely be associated with the low-ionization metal line (e.g., Schaye et al. 2007). This is certainly the case for systems for which the H I is not centered in velocity around the low ionization absorption (see e.g., Fig. 2).

The Si II/C II systems that show W_r higher than our thresholds, i.e. the strong absorbers, are listed in Table B3 for completeness. The systems with z_{abs} within 5000 km s^{-1} of the emission redshift (z_{em}) of the background AGN/QSOs, as listed in Table B4, are excluded for this study since they might have different origins (see e.g., Muzahid et al. 2013) than the intervening absorbers we are interested in. Additionally, the systems with cz < 1000 km s^{-1} are not considered here, since they are likely to be related to our own Galaxy and/or local group galaxies. We refer the reader to Richter et al. (2016a) for a detailed analysis of such absorbers. There are a total of 34 weak Mg II absorber analogs in our sample satisfying all of the above requirements.
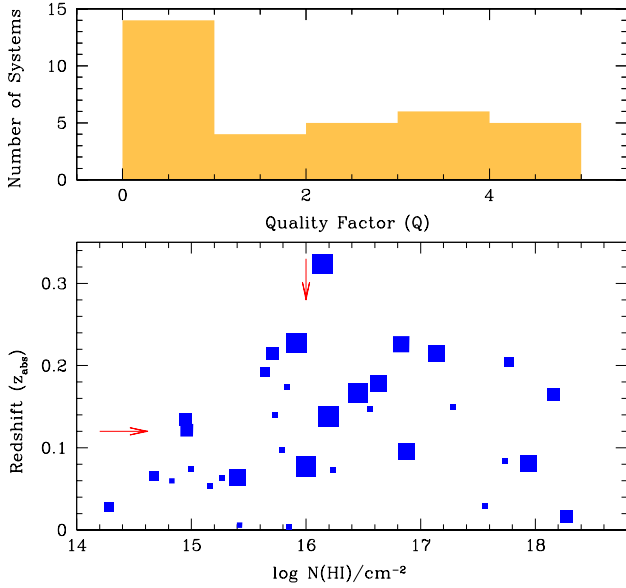
Figure 3. The absorption redshifts plotted against the $N(\text{H\,\textsc{i}})$ values estimated for individual systems. The median values of z_{abs} and $\log N(\text{H\,\textsc{i}})$ are indicated by the horizontal and vertical arrows, respectively. Symbol sizes are scaled by the corresponding quality factors (Q). The Q distribution is shown in the top panel. In total there are 16 systems with $Q \geqslant 3$ for which $N(\text{H\,\textsc{i}})$ estimates are reliable.

2.3 Absorption Line Measurements

Besides measuring equivalent widths, we used vpfit [2] to obtain column densities of H\,\textsc{i}, Si\,\textsc{ii}, and C\,\textsc{ii}. The column densities of Si\,\textsc{iii}, C\,\textsc{iv}, and O\,\textsc{vi} are also measured whenever available. Since the line spread function (LSF) of the COS spectrograph is not a Gaussian, we use the LSF given by Kriss (2011). The LSF was obtained by interpolating the LSF tables at the observed central wavelength for each absorption line and was convolved with the model Voigt profile while fitting absorption lines or generating synthetic profiles. For fitting an absorption line, we have used the minimum number of components required to achieve a reduced $\chi^2 \approx 1$. However, owing to the limited resolution of the COS spectrograph, we may be missing the "true" component structure. As a consequence, the Doppler parameters generally turn out to be larger compared to the high-z weak absorbers detected in high-resolution *VLT*/UVES spectra (e.g., Narayanan et al. 2008). For a strong line this would lead to an underestimation of the corresponding column density. Nevertheless, the column density can be accurately measured for a weak line that falls on the linear part of the curve-of-growth (COG). COS wavelength calibration is known to have uncertainties at the level of $\approx 5 - 15$ km s^{-1} (Savage et al. 2011; Muzahid et al. 2015a). We do see velocity misalignments of the same order between different absorption lines from the same system. An example of a weak absorber with the model profiles is shown in Fig. 2. System plots with Voigt profiles fits of the full sample are available in Appendix C.

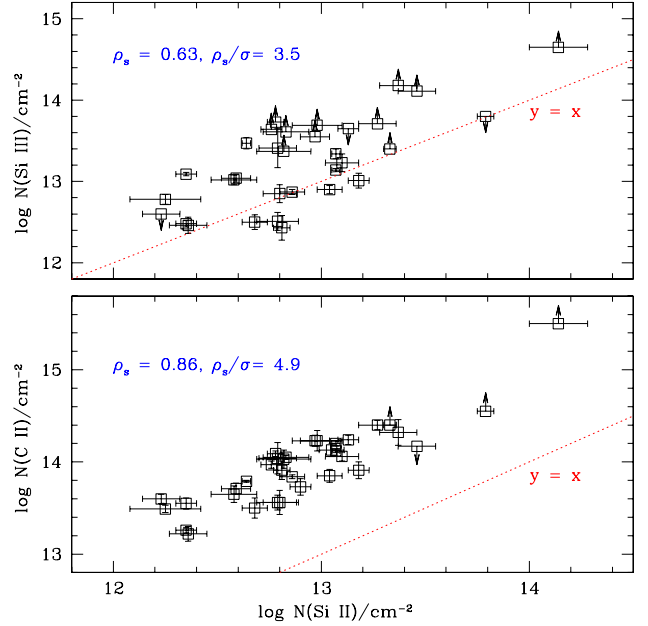**Figure 4.** $\log N(\text{C\,\textsc{ii}})$ versus $\log N(\text{Si\,\textsc{ii}})$ (bottom) and $\log N(\text{Si\,\textsc{iii}})$ versus $\log N(\text{Si\,\textsc{ii}})$ (top) for each absorber. Note that $N(\text{Si\,\textsc{ii}})$ is more tightly correlated with $N(\text{C\,\textsc{ii}})$ as compared to $N(\text{Si\,\textsc{iii}})$ in our sample. The $y = x$ (dotted) line is shown just for comparing the relative strengths of the low-ionization metal lines. The tight correlation between $N(\text{C\,\textsc{ii}})$ and $N(\text{Si\,\textsc{ii}})$ indicates that they trace the same phase of the absorbing gas. The somewhat larger scatter in the top panel possibly suggests that Si\,\textsc{iii} might have an additional contribution from the high-ionization gas phase for a fraction of the absorbers.

3 ANALYSIS

3.1 Absorber's Frequency, $d\mathcal{N}/dz$

We have read through the titles and the abstracts of all the relevant program IDs, under which the 296 COS spectra were obtained, in order to inspect whether the spectra were taken to probe the CGM of known foreground galaxies. The spectra obtained from dedicated CGM programs (e.g. PID: 11598, 12248) were assigned to "flag = 0", meaning that they are not part of our statistical sample. The remaining spectra with "flag = 1" constitute our statistical sample. There are 178 (118) "flag = 1" ("flag = 0") spectra in our sample. The redshift path-length covered for simultaneously detecting Si\,\textsc{ii}λ1260 ($\approx$0.2 Å) and C\,\textsc{ii} λ1334 ($\approx$0.3 Å) in the 178 spectra in our statistical sample is $\Delta z = 27.8$. There are 22 bona fide weak absorbers identified in these spectra (see Table 1). This yields the number density of weak absorbers, $d\mathcal{N}/dz = 0.8 \pm 0.2$ at $z < 0.3$. This is consistent with the value (1.00 ± 0.20) obtained by Narayanan et al. (2005) using a much smaller sample size. We note that the $d\mathcal{N}/dz$ of H\,\textsc{i} absorbers (Danforth et al. 2016) with $N(\text{H\,\textsc{i}}) \approx 10^{16}$ cm^{-2} at $z \approx 0.1$ (the median redshift of our sample) matches with that of the weak absorbers. Interestingly, the median $N(\text{H\,\textsc{i}})$ in our sample is 10^{16} cm^{-2}, as we describe in the next section. This re-confirms the finding of Churchill et al. (1999) that the majority of the weak absorbers arise in a sub-LLS environment.

Recently Richter et al. (2016b) have presented a sample of Si\,\textsc{iii} absorbers at similar redshift using archival COS spectra. They have found $d\mathcal{N}/dz$ of 2.5±0.4 for Si\,\textsc{iii} down to a $N(\text{Si\,\textsc{iii}})$ of $10^{12.2}$ cm^{-2}. Comparing this to the frequency of weak absorbers, we suggest that roughly half of the Si\,\textsc{iii} population should show associated weak

Si II absorption. From the middle panel of Fig. 6 of Richter et al. (2016b), there are 24 Si II absorbers with $W_r(\text{Si II}\lambda1260) < 200$ mÅ. This leads to a $d\mathcal{N}/dz$ of 1.0 ± 0.2 (using $\Delta z = 24$ for their sample) which is consistent with our estimate.

In Table 1, there are 12 absorbers that are detected in the "flag = 0" spectra. We did not use them for the $d\mathcal{N}/dz$ calculation in order to avoid any possible observational bias. However, those systems are considered in all other analyses related to the chemical/physical conditions of the absorbing gas.

3.2 Neutral Hydrogen Column Density, $N(\text{H I})$

Owing to the low redshifts of the weak absorbers ($z < 0.3$), higher order Lyman series lines are not covered by the COS spectra for most cases. 17/34 systems have only Lyα and 7/34 systems have both Lyα and Lyβ coverages. The remaining 10 systems have Lyα, Lyβ, and Lyγ (or higher order lines) coverages. Estimating reliable $N(\text{H I})$ values in the absence of unsaturated higher order Lyman series lines is challenging. We, thus, assign a quality factor "Q" for each of our $N(\text{H I})$ measurements based on the absorption strength (level of saturation) and the presence (or absence) of the higher order lines. The quality factor can take values from 1–5, with 5 being the best/secure measurements. $N(\text{H I})$ values with $Q = 1$ and 2 are not well constrained. For each absorber listed in Table 1, we checked the literature to see if a $N(\text{H I})$ measurement is available from FUSE data. For 7 systems we have adopted $N(\text{H I})$ values from the literature that were well constrained from higher-order Lyman series lines covered by the FUSE spectra. These systems are $z_{\text{abs}} = 0.22597$ towards HE0153-4520 (Savage et al. 2011), $z_{\text{abs}} = 0.16710$ towards PKS0405-123 (Prochaska et al. 2004), $z_{\text{abs}} = 0.13850$ towards PG1116+215 (Sembach et al. 2004), $z_{\text{abs}} = 0.06350$ towards 3C263 (Savage et al. 2012), $z_{\text{abs}} = 0.09495$ towards PKS1302-102 (Cooksey et al. 2008), $z_{\text{abs}} = 0.07774$ towards PHL1811 (Lacki & Charlton 2010), and $z_{\text{abs}} = 0.08091$ towards PHL1811 (Jenkins et al. 2005). There are 3 additional systems for which we have adopted $N(\text{H I})$ values from the literature. These systems are $z_{\text{abs}} = 0.22722$ towards Q0107–025A (Muzahid 2014), $z_{\text{abs}} = 0.21451$ towards SDSSJ1322+4645, and $z_{\text{abs}} = 0.17885$ towards SDSSJ1419+4207. The $N(\text{H I})$ estimates for the latter two systems are obtained from the Lyman limit breaks seen in the G140L, G130/1222 grating observations using COS (see Prochaska et al. 2017). For all of these 10 systems we assign $Q \geqslant 3$. The absorption redshifts and $N(\text{H I})$ estimates are shown in Fig. 3. The median $N(\text{H I})$ is $10^{16.0}$ cm^{-2} for the full sample. The median value becomes $10^{15.9}$ cm^{-2} for the systems with $Q \geqslant 3$. The median value of redshifts changes from 0.12 to 0.22 when we consider the systems with $Q \geqslant 3$ as opposed to the full sample. This follows from the fact that the most of the lower redshift systems do not have higher order Lyman series lines covered.

3.3 Metal Column Densities

Besides H I, we have measured the column densities of C II, Si II, Si III, C IV and O VI when available. All the measured total column densities (i.e. the sum of the component column densities) are listed in Table 2. The systems in our sample are weak by design and therefore it is expected that the C II and Si II lines are not saturated in most cases. In fact, for 29/34 cases we could measure the $N(\text{C II})$ adequately. The minimum and maximum values of $\log N(\text{C II})/\text{cm}^{-2}$ for these systems are 13.22 and 14.40, respectively, with a median value of 13.9. The median value increases only by ≈ 0.1 dex for the
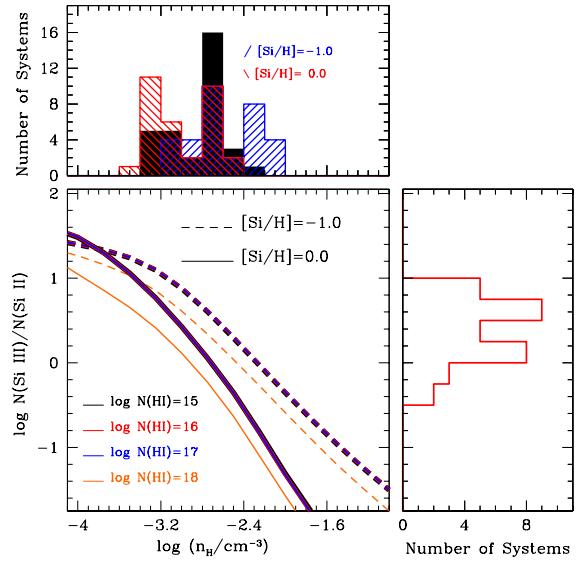

Figure 5. Bottom: CLOUDY predicted Si III to Si II ratios against the gas density for two different metallicities as indicated by the two different line styles. For each metallicity, four different models are run corresponding to four different $N(\text{H I})$ values as shown by different colors. Clearly, the ratio is degenerate with respect to the assumed model metallicity. The distribution of observed $N(\text{Si III})/N(\text{Si II})$ ratio is shown in the right panel. Top: The density distribution corresponding to the observed $N(\text{Si III})/N(\text{Si II})$ ratio distribution for the two different model metallicities. The solid black histogram indicates the final density distribution after correcting for the metallicity degeneracies (see text).

full sample. For all 34 systems we could measure $N(\text{Si II})$ reliably. The minimum and maximum values of $\log N(\text{Si II})/\text{cm}^{-2}$ are 12.23 and 14.14, respectively, with a median value of 12.9. The median value of $N(\text{Si II})$ is an order of magnitude lower than that of $N(\text{C II})$.

Owing to the large $f_{\text{osc}}\lambda_{\text{rest}}$ value (i.e. 2027) of the Si IIIλ1206 transition, the Si III absorption lines in our sample are saturated for nearly half (15/32) of the systems. We note that for two systems (i.e. $z_{\text{abs}} = 0.06376$ towards UKS-0242-724 and $z_{\text{abs}} = 0.07407$ towards SDSSJ1214+0825) Si III lines fall in the spectral gap and hence no $N(\text{Si III})$ information is available. The minimum and maximum values of $\log N(\text{Si III})/\text{cm}^{-2}$ are, respectively, 12.43 and 13.47 for the 18 systems in which we could measure $N(\text{Si III})$ adequately. The median value of the $N(\text{Si III})$ distribution is $10^{13.0}$ cm^{-2}, which is close to that of the $N(\text{Si II})$ distribution but a factor of ≈ 10 smaller than the $N(\text{C II})$ distribution. The median value of $\log N(\text{Si III})/\text{cm}^{-2}$ increases to ≈ 13.2 for the full sample.

In the bottom panel of Fig. 4, the C II column densities are plotted against $N(\text{Si II})$. Note that when multiple components are present, we have summed the component column densities. The $N(\text{C II})$ values are tightly correlated with $N(\text{Si II})$. A Spearman rank correlation test gives $\rho_s = 0.86$ with a 4.9σ significance. If we consider only systems in which both $N(\text{C II})$ and $N(\text{Si II})$ are measured adequately (i.e. excluding the limits) we obtain $\rho_s = 0.81$ with a 4.4σ significance. The strong correlation coefficient ensures that the C II and Si II arise from the same phase of the absorbing gas.

In the top panel of Fig. 4, the Si III column densities are plotted against $N(\text{Si II})$. A statistically significant correlation between $N(\text{Si III})$ and $N(\text{Si II})$, with $\rho_s = 0.63$ (3.5σ), is apparent from the figure. Nevertheless, there is more scatter in this plot compared to the bottom panel ($N(\text{C II})$ vs $N(\text{Si II})$). It is likely due to the fact that
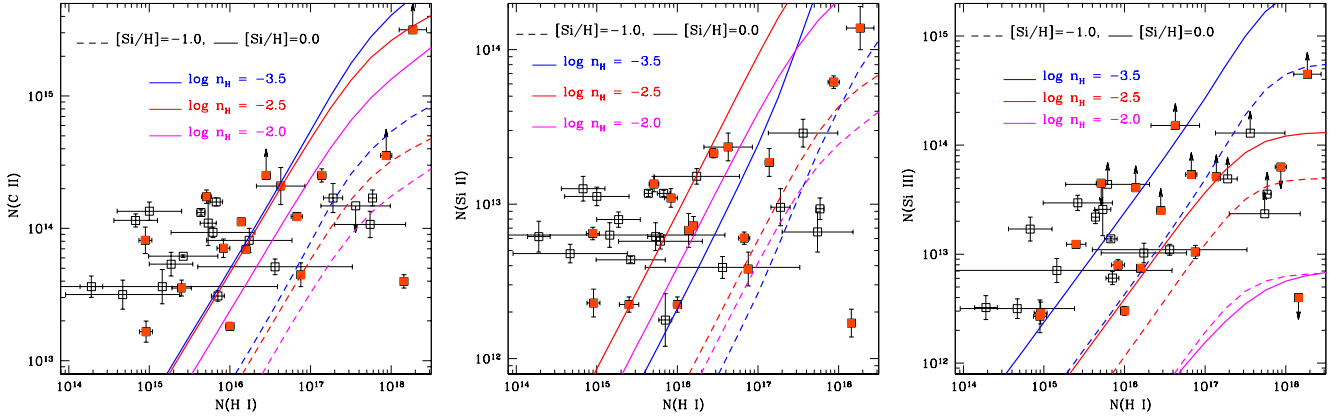
Figure 6. The C II (left), Si II (middle), and Si III (right) column densities against $N(\text{H I})$, as measured in different systems. The filled squares represent systems with $Q \geqslant 3$. The PI model curves corresponding to two different metallicities are shown in two different line-styles. For each model, we show three curves in three different colors corresponding to three representative densities (i.e., $\log n_H = -2.0, -2.5, \& -3.5$).

some amount of Si III might be contributed by the high-ionization gas phase giving rise to C IV/O VI absorption for at least some fraction of the systems. We will discuss this issue in more detail in the following section.

3.4 Ionization Modeling

We use the photoionization (PI) simulation code CLOUDY (v13.03, last described by Ferland et al. 2013) to infer the overall physical and chemical properties of the weak absorbers in our sample. In our constant density PI models, we have assumed that (a) the absorbing gas has a plane parallel geometry, (b) the gas is subject to the extragalactic UV background (UVB) radiation at $z = 0.1$ as computed by Khaire & Srianand (2015a, KS15 hereafter)[3], (c) the relative abundances of heavy elements in the absorbing gas are similar to the solar values as measured by Asplund et al. (2009), and (d) the gas is dust free. Models are run for two different gas-phase metallicities, i.e., $[X/H] = -1.0$ and $[X/H] = 0.0$. The KS15 UVB calculations make use of an updated QSO emissivity and star-formation rate density (see Khaire & Srianand 2015b, for details). Their models with escape fraction (of H I ionizing photons from galaxies, f_{esc}) of 0% provide H I photoionization rates ($\Gamma_{H I}$) at $z < 0.5$ that are consistent with the measurements of Shull et al. (2015) and Gaikwad et al. (2016). We therefore use their model corresponding to $f_{esc} = 0\%$.

PI models for all the absorbers are done in a uniform fashion. First, we assume that the Si II and Si III absorption lines originate in the same phase of the absorbing gas and hence the ratio of $N(\text{Si III})/N(\text{Si II})$ uniquely fixes the $\log U$ (or $\log n_H$) of the absorber. We, however, note that the Si III need not entirely stem from the low-ionization gas phase that produces Si II. If some amount of Si III arise from high-ionization gas phase, the Si III to Si II ratio would provide an upper limit on the ionization parameter (a lower limit on density). Next, we use the ionization corrections of H I and

Si II ($f_{H I}$ and $f_{Si II}$, respectively) at the derived n_H and calculate the Si abundance, $[Si/H] = \log N(\text{Si II})/N(\text{H I}) - \log f_{Si II}/f_{H I} - \log (Si/H)_{\odot}$, of the absorber using the observed $N(\text{H I})$ and $N(\text{Si II})$. The $f_{Si II}/f_{H I}$ ratio shows a relatively flat peak for a large range in density of $10^{-3.4} - 10^{-2.4} \text{cm}^{-3}$, and falls off rapidly at both below and above this density range. Thus, even if the measured $N(\text{Si III})$ has some contribution from a high ionization gas phase, our inferred metallicity will essentially be unaltered (see also Section 5.3).

4 RESULTS BASED ON THE PI MODELS

4.1 The density (ionization parameter) distribution

In the bottom panel of Fig. 5 we show the variation of the model predicted $N(\text{Si III})/N(\text{Si II})$ ratio with density for two different model metallicities, i.e., solar and 1/10th of solar values. We note that the $N(\text{Si III})/N(\text{Si II})$ ratio depends on the metallicity assumed in the CLOUDY model. This is likely due to the increased electron density in high metallicity gas increasing the recombination/cooling rate for a fixed density and temperature. For each model metallicity we have used four different $\log N(\text{H I})/\text{cm}^{-2}$ values (i.e., 15, 16, 17, and 18) as the stopping conditions for the simulations. Note that, for a given metallicity, the ratio is independent of the $N(\text{H I})$ values as long as the gas is optically thin to the hydrogen ionizing photons (i.e., $N(\text{H I}) \lesssim 10^{17.2} \text{cm}^{-2}$). We, however, used the observed $N(\text{H I})$ values as stopping conditions for CLOUDY for each of the absorbers in order to derive individual constraints.

---

[3] Ideally one should use different UVBs corresponding to the z_{abs} of the different absorbers. Since the majority of the systems in our sample have z_{abs} in the range 0.0–0.2 (only one system at $z_{abs} > 0.3$) with a median z_{abs} of ≈ 0.1, we have used the UVB at $z = 0.1$ for all the absorbers. We have found that the use of $z = 0.1$ UVB for all the absorbers could lead to a maximum uncertainty in the ionization parameter, $\log U$, of ≈ 0.2 dex, where $\log U = \log n_{\gamma} - \log n_H$, is the ratio of number density of H I ionizing photons to the number density of protons.

Table 2. Summary of column density measurements and photoionization model parameters.

QSO	z_{abs}	$\log N(\text{H\,I})$	$\log N(\text{C\,II})$	$\log N(\text{Si\,II})$	$\log N(\text{Si\,III})$	Q	$\log n_{\text{H}}(U)$ $(1/\text{cm}^{-3})$	[Si/H]	$\log N_{\text{H}}$ $(1/\text{cm}^{-2})$	L (kpc)	$\log N(\text{C\,IV})$ (observed)	(model)	$\log N(\text{O\,VI})$ (observed)	(model)	$\log N(\text{Mg\,II})$ (model)
PG0003+158	0.16512	18.16 ± 0.03	13.60 ± 0.05	12.23 ± 0.09	<12.60	3	−2.9 (−3.1)	−2.5	19.9	2.02E+01	NA	12.2	13.82 ± 0.12	9.7	11.8
Q0107-025A	0.22722	15.92 ± 0.08	13.85 ± 0.07	13.04 ± 0.06	12.90 ± 0.05	5	−2.6 (−3.4)	0.2	17.7	6.91E-02	14.24 ± 0.12^a	12.4	14.57 ± 0.23	9.2	12.4
HE0153-4520	0.22597	16.83 ± 0.07	14.09 ± 0.03	12.78 ± 0.04	>13.73	4	−3.1 (−2.9)	−0.7	19.2	6.34E+00	NA	13.9	14.24 ± 0.02	11.9	12.3
3C57	0.32338	16.14 ± 0.02	14.05 ± 0.02	12.83 ± 0.11	>13.61	5	−3.3 (−2.7)	0.0	18.6	2.47E+00	NA	14.2	<13.4	12.6	12.2
SDSSJ0212-0737	0.01603	18.27 ± 0.17	>15.50	14.14 ± 0.14	>14.65	3	−3.1 (−2.9)	−0.7	20.2	5.33E+01	15.03 ± 0.25	14.5	NA	12.3	13.8
SDSSJ0212-0737	0.13422	14.95 ± 0.08	13.91 ± 0.10	12.81 ± 0.04	12.43 ± 0.15	3	−2.5 (−3.5)	0.9	16.6	3.59E-03	<13.4	11.8	<13.7	8.1	12.2
UKS-0242-724	0.06376	15.27±0.27	13.73 ± 0.09	12.90 ± 0.05	NA	1	...	...	...	...	<13.3	...	NA	...	...
Q0349-146	0.07256	16.24 ± 0.53	13.91 ± 0.09	13.18 ± 0.05	13.01 ± 0.09	1	−2.6 (−3.4)	0.0	18.0	1.34E-01	<13.5	12.5	NA	9.3	12.5
PKS0405-123	0.16710	16.45 ± 0.05	>14.40	13.33 ± 0.03	>13.40	5	−2.8 (−3.2)	−0.1	18.4	4.56E-01	14.16 ± 0.05^b	13.1	14.73 ± 0.13	10.3	12.7
IRAS-F04250-5718	0.00369	15.85 ± 0.08	13.49 ± 0.04	12.25 ± 0.17	12.78 ± 0.06	1	−3.1 (−2.9)	−0.4	18.1	4.92E-01	13.21 ± 0.15	13.0	NA	10.9	11.6
FBQS-0751+2919	0.20399	17.77 ± 0.05	14.23 ± 0.06	12.97 ± 0.07	>13.55	2	−2.8 (−3.2)	−1.5	19.8	1.40E+01	NA	13.1	14.35 ± 0.07	10.5	12.6
VV2006J0808+0514	0.02930	17.56 ± 0.43	<14.17	13.46 ± 0.09	>14.11	1	−2.8 (−3.2)	−0.8	19.7	9.66E+00	NA	13.7	NA	11.1	13.1
PG0832+251	0.02811	14.28 ± 0.14	13.56 ± 0.08	12.79 ± 0.10	12.51 ± 0.11	2	−2.5 (−3.5)	1.6	16.0	1.01E-03	<13.3	11.9	NA	8.5	12.2
SDSSJ0929+4644	0.06498	14.67 ± 0.71	13.50 ± 0.11	12.68 ± 0.06	12.50 ± 0.09	2	−2.6 (−3.4)	1.1	16.4	3.35E-03	<13.1	12.0	NA	8.7	12.0
PMNJ1103-2329	0.08352	17.74 ± 0.44	14.03 ± 0.10	12.82 ± 0.13	>13.37	1	−2.8 (−3.2)	−1.6	19.7	1.15E+01	14.43 ± 0.06	12.9	NA	10.2	12.5
PG1116+215	0.13850	16.20 ± 0.05	13.84 ± 0.02	12.86 ± 0.06	12.87 ± 0.03	5	−2.7 (−3.3)	−0.3	18.1	2.07E-01	13.19 ± 0.08	12.5	13.84 ± 0.02	9.6	12.2
SDSSJ1122+5755	0.05319	15.16 ± 1.43	13.56 ± 0.13	12.80 ± 0.08	12.85 ± 0.11	1	−2.7 (−3.3)	0.7	17.1	2.03E-02	13.71 ± 0.15	12.5	NA	9.6	12.1
PG1121+422	0.19238	15.64 ± 0.05	14.12 ± 0.02	13.07 ± 0.02	13.34 ± 0.06	2	−2.9 (−3.1)	0.5	17.7	1.26E-01	NA	13.2	<13.4	10.8	12.4
3C263	0.06350	15.40 ± 0.12	13.55 ± 0.06	12.35 ± 0.05	13.09 ± 0.02	4	−3.2 (−2.8)	0.3	17.8	3.66E-01	14.13 ± 0.15	13.6	NA	11.9	11.8
PG1202+281	0.13988	15.73 ± 0.10	14.04 ± 0.17	12.79 ± 0.09	13.41 ± 0.24	1	−3.1 (−2.9)	0.3	18.1	5.15E-01	<13.9	13.8	<13.6	11.8	12.2
PG-1206+459	0.21439	15.71 ± 0.06	14.24 ± 0.05	13.13 ± 0.05	<13.65	3	−3.1 (−2.9)	0.6	18.0	3.44E-01	NA	13.9	NA	11.8	12.5
SDSSJ1210+3157	0.05974	14.83 ± 0.27	14.06 ± 0.05	13.10 ± 0.08	13.23 ± 0.11	1	−2.8 (−3.2)	1.3	16.8	1.23E-02	14.50 ± 0.10	13.0	NA	10.2	12.4
SDSSJ1210+3157	0.14964	17.28 ± 0.12	14.23 ± 0.11	12.98 ± 0.12	>13.69	1	−2.8 (−3.2)	−1.0	19.4	5.95E+00	14.35 ± 0.13	13.4	14.72 ± 0.11	10.8	12.6
SDSSJ1214+0825	0.07407	15.00 ± 0.40	14.13 ± 0.07	13.05 ± 0.06	NA	1	...	...	...	...	NA	...	NA	...	...
RXJ1230.8+0115	0.00575	15.42 ± 0.43	13.79 ± 0.01	12.64 ± 0.02	13.47 ± 0.07	1	−3.3 (−2.7)	0.6	17.9	5.48E-01	13.32 ± 0.19	14.2	NA	12.6	12.0
PKS1302-102	0.09495	16.88 ± 0.03	13.65 ± 0.09	12.58 ± 0.11	13.02 ± 0.06	4	−2.6 (−3.4)	−1.1	18.8	7.78E-01	<13.0	12.3	<13.9	9.2	12.2
SDSSJ1322+4645	0.21451	17.14 ± 0.05	14.40 ± 0.05	13.27 ± 0.09	>13.71	4	−2.6 (−3.4)	−0.6	19.0	1.46E+00	NA	13.0	14.55 ± 0.08	9.9	12.9
SDSSJ1357+1704	0.09784	15.79 ± 0.52	13.97 ± 0.04	12.76 ± 0.05	>13.64	1	−3.3 (−2.7)	0.4	18.3	1.60E+00	13.92 ± 0.12	14.4	<14.1	13.0	12.2
SDSSJ1419+4207	0.17885	16.63 ± 0.30	14.32 ± 0.14	13.37 ± 0.09	>14.18	4	−3.3 (−2.7)	0.1	19.2	9.34E+00	NA	14.9	14.43 ± 0.05	13.2	12.8
PG1424+240	0.12126	14.96 ± 0.08	13.22 ± 0.08	12.36 ± 0.09	12.46 ± 0.10	3	−2.8 (−3.2)	0.4	16.9	1.50E-02	13.70 ± 0.06	12.2	14.44 ± 0.05	9.4	11.7
PG1424+240	0.14683	16.56 ± 0.96	13.71 ± 0.06	12.59 ± 0.07	13.04 ± 0.05	1	−2.6 (−3.4)	−0.7	18.5	3.84E-01	14.18 ± 0.06	12.4	14.04 ± 0.13	9.3	12.2
PG-1630+377	0.17388	15.83 ± 0.08	14.20 ± 0.03	13.07 ± 0.02	13.14 ± 0.02	1	−2.8 (−3.2)	0.3	17.7	1.03E-01	NA	12.8	13.86 ± 0.03	10.0	12.4
PHL1811	0.07774	16.00 ± 0.05	13.26 ± 0.03	12.35 ± 0.05	12.48 ± 0.04	5	−2.4 (−3.6)	−0.4	17.6	3.24E-02	<13.0	11.4	NA	6.6	11.9
PHL1811	0.08091	17.94 ± 0.07	>14.55	13.79 ± 0.04	<13.80	4	−2.5 (−3.5)	−0.8	19.4	2.42E+00	14.04 ± 0.04	12.8	NA	8.9	13.3

Notes–

No ionization model is done for the z_{abs} = 0.06376 towards UKS-0242-724 and z_{abs} = 0.07407 towards SDSSJ1214+0825 systems due to the lack of the $N(\text{Si\,III})$ measurements.

"NA" indicates that the line is either severely blended or not covered by the corresponding COS spectrum.

The last column gives the predicted Mg II column densities. The model predicted $N(\text{Mg\,II})$ values reassure that these are indeed analogs of weak Mg II absorbers (see also Appendix A).

While assigning formal 1σ confidence intervals in the inferred densities and metallicities is not straightforward, we find that our metallicity estimates are adequate within 0.2 dex, provided that the $N(\text{H\,I})$ estimates are accurate (see Section 5.3). The densities are very sensitive to the metallicity assumed in the CLOUDY grid, particularly for the metal-rich systems. We find that the densities can be off by a factor of $\approx$3–4.

^{a}From Muzahid (2014), ^{b}From Savage et al. (2010).

The red (135°) hashed histogram in the top panel of Fig. 5 represents the $\log n_{\mathrm{H}}$ distribution corresponding to the observed $N(\mathrm{Si\,III})/N(\mathrm{Si\,II})$ ratios, shown in the bottom-right panel, for an assumed metallicity of $[\mathrm{X/H}] = 0.0$. The blue (45°) hashed histogram, on the other hand, represents the same for an assumed metallicity of $[\mathrm{X/H}] = -1.0$. Clearly, an assumption of any particular model metallicity for all the absorbers in a sample leads to an incorrect density distribution[4]. In order to overcome this problem we have performed our PI modelling in an iterative way. First, we used the density solution corresponding to the $[\mathrm{X/H}] = -1.0$ model and calculate the Si abundances for each absorber. We then select the systems with $[\mathrm{Si/H}] > -0.3$ (i.e. half solar) and redo the density calculation using the $[\mathrm{X/H}] = 0.0$ model. The distribution of our final density solutions is shown by the black histogram in the top panel of Fig. 5. The $\log n_{\mathrm{H}}/\mathrm{cm}^{-3}$ distribution has a median value of -2.8 with minimum and maximum values of -3.3 and -2.4, respectively. For the adopted UVB, this leads to a range in ionization parameter, $\log U$, of -2.7 to -3.6 with a median value of -3.2.

4.2 The column density trends

In the different panels of Fig. 6, column densities of low-ionization metal lines are plotted against the corresponding $N(\mathrm{H\,I})$. A mild trend of increasing low-ionization metal line column densities with increasing $N(\mathrm{H\,I})$ is noticeable. A similar trend has also been reported for the COS-Halos sample (i.e., Werk et al. 2013; Prochaska et al. 2017). A Spearman rank correlation analysis, assuming limits are detections, also confirms the trends with a $\rho_s \gtrsim 0.3$ when the full sample is considered (see Table 3). It is important to note that when we consider the sub-sample with $N(\mathrm{H\,I}) > 10^{16}\ \mathrm{cm}^{-2}$ (median value), the correlation coefficients remain high (i.e. $\rho_s \gtrsim 0.2$). The sub-sample with $N(\mathrm{H\,I}) \leqslant 10^{16}\ \mathrm{cm}^{-2}$, on the contrary, show ρ_s consistent with 0.0. Though the sample size is small, it seems that the mild trends seen in the full sample are mainly driven by the systems with $N(\mathrm{H\,I}) > 10^{16}\ \mathrm{cm}^{-2}$.

In each panel in Fig. 6, six different PI model curves, corresponding to two different metallicities and three different densities, are overplotted. Note that the three representative densities span the density range we obtained from the $N(\mathrm{Si\,III})/N(\mathrm{Si\,II})$ ratios as discussed above. It is apparent from the three panels that the majority of the systems with $\log N(\mathrm{H\,I})/\mathrm{cm}^{-2} < 16.0$ are not reproduced by the models with 1/10th of solar metallicity. Moreover, even the solar-metallicity-models fail to reproduce the systems with $\log N(\mathrm{H\,I})/\mathrm{cm}^{-2} < 15.7$. It is, therefore, clear that the vast majority of the weak absorbers studied here have very high metallicities.

4.3 Trends in the model parameters

The PI model predicted densities (n_{H}), Si-abundances ($[\mathrm{Si/H}]$), total hydrogen column densities (N_{H}), and line of sight thicknesses (L) are listed in columns 8, 9, 10, and 11 of Table 2, respectively. As mentioned before, the densities of the absorbers show a range of $10^{-3.3}$–$10^{-2.4}\ \mathrm{cm}^{-3}$ with a median value of $10^{-2.8}\ \mathrm{cm}^{-3}$. The density range and the median value do not change when only $Q > 2$ systems are considered. The inferred $[\mathrm{Si/H}]$ values show a range of -2.5 to $+1.6$ with a median value of 0.0 (i.e. solar abundance). However, when we considered only $Q > 2$ systems the maximum value drops to $[\mathrm{Si/H}] = 0.9$ (i.e. ≈ 8 times solar) and the median

value becomes -0.1. The total hydrogen column densities for the weak absorbers show a range of 4 orders of magnitude, i.e., $N_{\mathrm{H}} = 10^{16.0-20.3}\ \mathrm{cm}^{-2}$, with a median value of $10^{18.1}\ \mathrm{cm}^{-2}$. The line of sight thicknesses, L, also exhibit a wide range of 1 pc – 53 kpc with a median value of ≈ 500 pc. The median value changes to ≈ 780 pc for the systems with $Q > 2$.

The PI model parameters are plotted against the observed column densities of H I (top row), C II (middle row), and Si II (bottom row) in Fig. 7. The inferred densities do not show any trend with the neutral hydrogen and/or low-ionization metal line column densities. No significant correlation is seen between $[\mathrm{Si/H}]$ and $N(\mathrm{C\,II})$ or $N(\mathrm{Si\,II})$. A strong anti-correlation ($\rho_s = -0.94$, $\rho_s/\sigma = -5.2$) between $[\mathrm{Si/H}]$ and $N(\mathrm{H\,I})$, however, is apparent from the figure. The trend remains statistically significant ($\rho_s = -0.89$, $\rho_s/\sigma = -3.5$) when only systems with $Q > 2$ are considered. A similar trend has been recently reported by Prochaska et al. (2017) in the COS-Halos sample. Such a trend is generally expected in a metal line selected sample of absorbers, because, in practice, there are many low-$N(\mathrm{H\,I})$ systems without any detectable low-ionization metal lines that are not considered in our study. In order to investigate the dependence of the correlation on $N(\mathrm{H\,I})$, we have performed the Spearman rank correlation analysis for two different sub-samples, one with $N(\mathrm{H\,I}) > 10^{16}\ \mathrm{cm}^{-2}$ and the other with $N(\mathrm{H\,I}) \leqslant 10^{16}\ \mathrm{cm}^{-2}$, separately. We obtain $\rho_s = -0.75$ and $\rho_s/\sigma = -2.9$ ($\rho_s = -0.89$ and $\rho_s/\sigma = -3.5$) for the upper-$N(\mathrm{H\,I})$ (lower-$N(\mathrm{H\,I})$) sub-samples, suggesting a statistically significant anti-correlation between $[\mathrm{Si/H}]$ and $N(\mathrm{H\,I})$ for the systems with $N(\mathrm{H\,I}) > 10^{16}\ \mathrm{cm}^{-2}$. Note that, $>80\%$ of the low-z H I absorbers with $N(\mathrm{H\,I}) > 10^{16}\ \mathrm{cm}^{-2}$ exhibit low-ionization metal lines (see Fig. 8 in Danforth et al. 2016). Thus, the strong anti-correlation seen in the full sample *cannot* be fully attributed to sample selection bias (see also the discussion of Misawa et al. 2008). However, we do point out that our survey is limited to weak absorbers only. Inclusion of strong absorbers would introduce more scatter in the relation, particularly at the higher $N(\mathrm{H\,I})$ end.

The strong 5.2σ correlation between N_{H} and $N(\mathrm{H\,I})$ is not surprising since the expected variation in $f_{\mathrm{H\,I}}$ over the inferred narrow density range of $10^{-3.3} - 10^{-2.4}\ \mathrm{cm}^{-3}$ is small and N_{H} ($\equiv N(\mathrm{H\,I})/f_{\mathrm{H\,I}}$) is directly proportional to $N(\mathrm{H\,I})$. The 4.7σ correlation between L ($\equiv N_{\mathrm{H}}/n_{\mathrm{H}}$) and $N(\mathrm{H\,I})$ follows from the fact that N_{H} is strongly correlated with $N(\mathrm{H\,I})$ whereas n_{H} is not. The N_{H} also show a significant (mild) correlation with $N(\mathrm{C\,II})$ ($N(\mathrm{Si\,II})$). If the column density of the (i+1)-th ionization state of an element X, with ionization fraction of $f_{\mathrm{X_i}}$, is $N(\mathrm{X_i})$, then

$$N_{\mathrm{H}} = \frac{N(\mathrm{X_i})}{f_{\mathrm{X_i}} 10^{[\mathrm{X/H}]}(\mathrm{X/H})_{\odot}}, \text{ and} \tag{1}$$

$$L = \frac{N(\mathrm{X_i})}{f_{\mathrm{X_i}} 10^{[\mathrm{X/H}]}(\mathrm{X/H})_{\odot} n_{\mathrm{H}}}. \tag{2}$$

Thus, a correlation between N_{H} (and/or L) and metal line column density is generally anticipated. Any anti-correlation between the metallicity ($[\mathrm{X/H}]$) and the ionic column density, as seen for C II, would further strengthen the correlation. The apparent lack of any correlation between $[\mathrm{Si/H}]$ and $N(\mathrm{Si\,II})$ has been manifested by the mild 1.6σ correlation seen between N_{H} and $N(\mathrm{Si\,II})$ in contrast to the strong 3.0σ correlation seen between N_{H} and $N(\mathrm{C\,II})$.

4.4 High-ionization metal lines

Although the main focus of this paper is the weak absorbers detected via the low-ionization metal lines, in all but a few cases high-

---

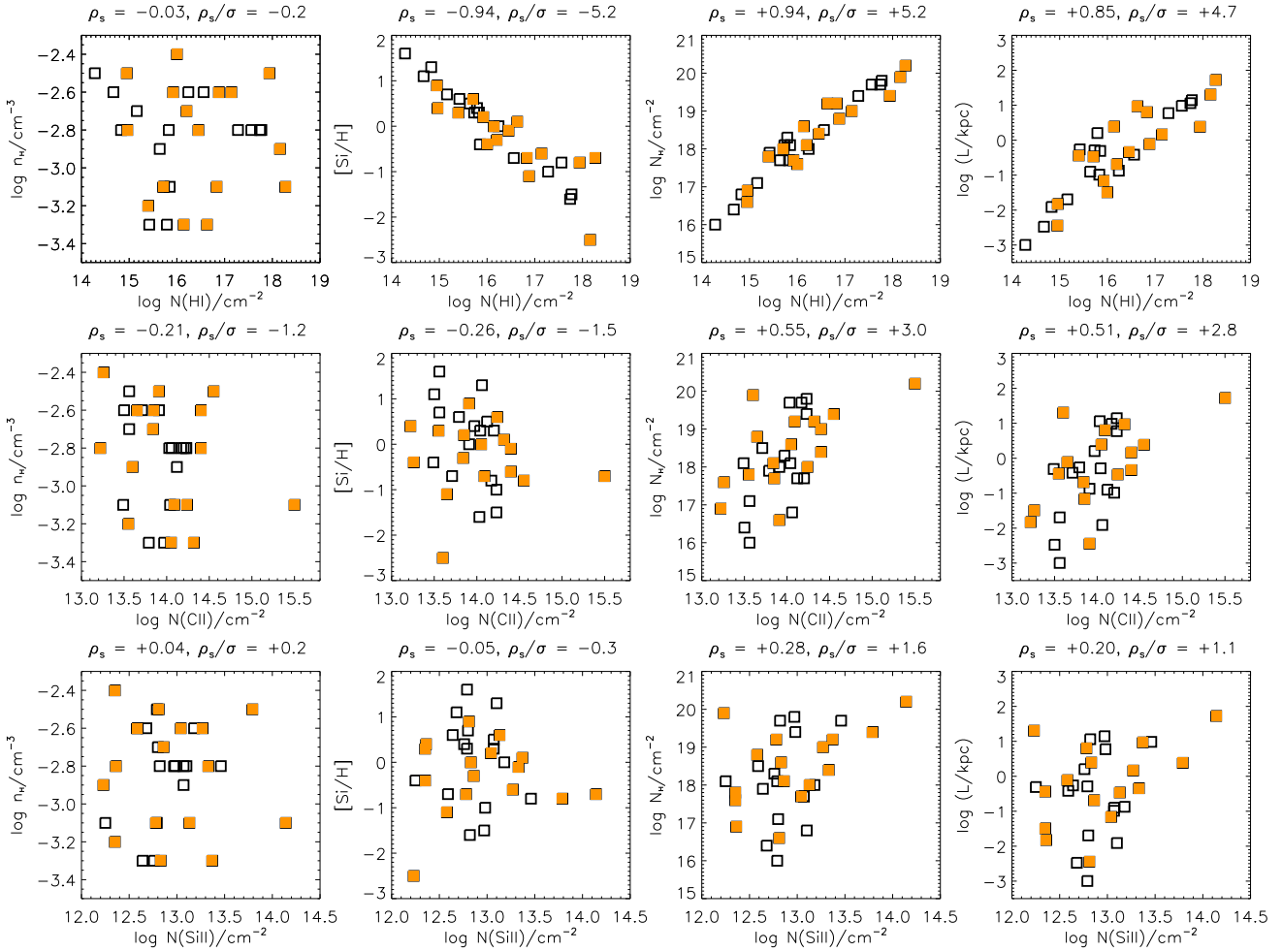[4] We, however, note that the effect is less important for the derived metal abundances.

Figure 7. Scatter plots of PI model parameters (log n_H, 1st column; [Si/H], 2nd column; log N_H, 3rd column; log L, 4th column) and the observed column densities (N(H I), top row; N(C II), middle row; N(Si II), bottom row). The filled squares represent the systems with $Q > 2$. The results of the Spearman rank correlation analysis are mentioned on the top of each panel. Possible origins of the observed correlations are discussed in the text. In particular, we argue that the 5.2σ anti-correlation seen between [Si/H] and log N(H I) *cannot* be entirely attributed to selection bias.

Table 3. The details of Spearman rank correlation analysis

Sample	Data1	Data2	ρ_s	ρ_s/σ
Full	N(H I)	N(C II)	0.48	2.8
Full	N(H I)	N(Si II)	0.28	1.6
N(H I) $> 10^{16}$ cm^{-2}	N(H I)	N(C II)	0.30	1.2
N(H I) $> 10^{16}$ cm^{-2}	N(H I)	N(Si II)	0.20	0.8
N(H I) $\leqslant 10^{16}$ cm^{-2}	N(H I)	N(C II)	0.10	0.4
N(H I) $\leqslant 10^{16}$ cm^{-2}	N(H I)	N(Si II)	−0.12	−0.5

ionization metal lines (e.g. C IV and/or O VI) are also covered. For example, N(C IV) information is available for a total of 23 systems (15 measurements and 8 upper limits, see Table 2). All the upper limits on N(C IV) are consistent with our PI model predictions. For the 15 systems with positive detection of C IV, the column densities are found to be in the range $10^{13.2-15.0}$ cm^{-2} with a median value of $10^{14.1}$ cm^{-2}. Our N(C IV) measurements are at least 0.5 dex higher than the model predicted values for 12/15 systems, suggesting a separate gas phase for C IV absorption in those absorbers. For the $z_{abs} = 0.00369$ system towards IRAS-F04250-5718, the difference is only 0.2 dex, which is well within our PI model uncertainties. For the two other systems ($z_{abs} = 0.00575$ towards RXJ1230.8+0115 and $z_{abs} = 0.09784$ towards SDSSJ1357+1704) the model predicted

C IV column densities are higher than the observed ones. In both these systems the Si IV line is detected. It is likely that the majority of the Si III absorption in these systems arises from the gas phase giving rise to Si IV (and C IV) absorption. In that situation the ionization parameter of the low-ionization phase can be a lot lower which, in turn, will reduce the predicted N(C IV). In the $z_{abs} = 0.09784$ system towards SDSSJ1357+1704, the stronger Si III component at ≈ 0 km s^{-1}, which dominates the total N(Si III), is not seen in the low-ionization lines but is seen in the Si IV line (see Appendix C). We further note that the majority of systems for which the predicted N(C IV) values are considerable (i.e. $> 10^{14.0}$ cm^{-2}) show strong Si IV absorption. These facts demonstrate the need for component-by-component, multi-phase photoionization models (see e.g., Charlton et al. 2003; Milutinović et al. 2006; Misawa et al. 2008), which is beyond the scope of this paper.

The O VI doublet is covered for 18/34 of the weak absorbers, of which 12 show detectable absorption. The O VI column densities in these absorbers vary between $10^{13.8-14.7}$ cm^{-2} with a median value of $10^{14.4}$ cm^{-2}. The maximum predicted N(O VI) by our PI models (i.e., $10^{13.2}$ cm^{-2}) is 0.6 dex lower than the lowest measured N(O VI) value. It clearly indicates that in all these systems O VI must originate from a separate gas phase. In 10/34 of the weak absorbers

both the C IV and the O VI doublets are covered. In 6/10 cases both C IV and O VI are detected, and it is likely that they arise in the same gas phase. In one case ($z_{abs} = 0.09784$ towards SDSSJ1357+1704 discussed in the paragraph above) only C IV is detected. Finally, in 3/10 cases neither C IV or O VI are detected. We conclude that about two thirds of the weak absorbers have a separate, higher ionization or hotter phase.

5 DISCUSSION

5.1 Redshift Evolution

Our sample of 34 weak Mg II absorber analogs at $z < 0.3$ represents a substantial increase over the sample of 6 absorbers found by Narayanan et al. (2005) at low redshift. However, the value of $dN/dz = 0.8 \pm 0.2$ that we have derived is consistent with that earlier study, and a factor of a few smaller than what would be expected if static populations of weak Mg II and C IV absorbers were simply evolved to the present era subject to the decreasing UVB. Narayanan et al. (2005) noted that both pc-scale structures that produce weak Mg II absorption at $z \approx 1$ and kpc-scale structures that are detected in C IV absorption, but not in low ionization transitions, would evolve from $z \approx 1$ to produce weak low ionization absorption at $z \approx 0.1$. To some extent, both populations must be less abundant at low redshift than they were at $z \approx 1$. The present sample of 34 absorbers is large enough that we can attempt to determine how the low redshift population compares to the $z \approx 1$ population, however Narayanan et al. (2005) warned that "hidden phases" would in some cases make it impossible to extract accurate physical properties (see their Figs. 10–12).

We begin by noting that 7/34 of our weak absorbers are very small (< 32 pc) structures with solar or super-solar metallicity and with derived densities $\log n_H/cm^{-3} \approx -2.6$ in the upper half of our sample. Although these overlap with the densities derived by Narayanan et al. (2008) for weak Mg II absorbers (using coverage of Fe II to constrain density), they are at the low end of the range. All but one of these seven small absorbers has only one low ionization component, and C IV is either not detected at all (in 4/7) or it could be in the same phase with, and centered on the low ionization absorption. Even these absorbers, for which the metallicity is inferred to be quite high, could have two phases that contribute roughly equally to the Si II/C II absorption, as in the simulated system in Fig. 11 of Narayanan et al. (2005). However, it is still clear that there is a smaller, higher density phase which has a surprisingly high metallicity.

Furthermore, many of the remaining 27/34 absorbers, though they have larger derived line of sight thicknesses based on our conservative estimates, are likely to have a hidden phase. The inferred density of that phase would be higher than we estimate if some of the Si III is in fact in a lower density phase that produced C IV absorption. The inferred metallicity of that phase would be higher if some of the H I is associated with the higher ionization transitions, C IV and/or O VI.

Thus, despite our larger sample, the situation remains unclear. We can, however, affirm that there are fewer weak, low ionization absorbers at present than we would expect if we took the absorber population at $z \approx 1$ and simply evolved the same structures to the present day subject to a lower UVB. However, as we discuss below, it seems more likely that the weak absorbers are transient, and that the processes that create these small, high metallicity structures faraway from galaxies are less active at present than they were in the past.

5.2 Cosmological Importance

If the comoving number density of the weak absorbers at $z \approx 0.1$ is n_{cl} and the proper cross-section is typically πR_{cl}^2 then dN/dz can be expressed as:

$$\frac{dN}{dz} = n_{cl}\pi R_{cl}^2 \frac{c}{H_0} \frac{(1+z)^2}{\sqrt{(1+z)^3\Omega_M + \Omega_\Lambda}} \ . \tag{3}$$

If we assume a spherical geometry for the weak absorbers with a characteristic radius of $R_{cl} \equiv L/2$, where $L \approx 500$ pc is the median line of sight thickness we obtained from PI model, then the comoving number density becomes $n_{cl} \sim 8 \times 10^2$ Mpc^{-3} for the observed dN/dz of ≈ 0.8. Integrating the r-band luminosity function of $z = 0.1$ galaxies in SDSS (Blanton et al. 2003b), the number density of galaxies down to $0.01L_*$ is $n_{gal} \sim 2 \times 10^{-2} h^3$ Mpc^{-3}. Therefore, the population of weak absorber clouds must have been huge, and outnumbered bright galaxies by tens of thousands to one. Similar conclusions have been drawn for the weak absorber population at high-z (Rigby et al. 2002), for metal-rich C IV absorbers at $z \approx 2.3$ (Schaye et al. 2007), and for Ne VIII absorbers at $z \approx 0.7$ (Meiring et al. 2013).

Under the assumption of spherical geometry, the cloud mass can be expressed as:

$$M_{cl} = \frac{4\pi}{3} R_{cl}^3 n_H \mu m_p \ , \tag{4}$$

where, $\mu \approx 1.4$ is the mean atomic weight. Using the median L and n_H values we derived from the PI models, we obtain $< M_{cl} > \sim 10^3 M_\odot$. The cosmic mass density of the weak absorbers at $z \approx 0.1$ is then $\Omega \equiv n_{cl}M_{cl}/\rho_{cr} \sim 10^{-6}$, where $\rho_{cr} \approx 2 \times 10^{11} M_\odot$ Mpc^{-3} is the critical density of the universe. Clearly, the weak absorbers at $z \approx 0.1$ carry a negligible fraction of cosmic baryons ($\Omega_b \approx 0.04$).

If the weak absorber clouds are associated with the CGM of a galaxy population with comoving number density n_{gal} at $z \approx 0.1$, then the derived dN/dz can, alternatively, be used to estimate the characteristic radius of the halo using the following relation:

$$R_h \approx 130 \text{ kpc} \left(\frac{dN/dz}{0.8}\right)^{1/2} \left(\frac{n_{gal}}{10^{-2}\text{Mpc}^{-3}}\right)^{-1/2} C_f^{-1/2} \ . \tag{5}$$

Here C_f is the covering fraction of the weak absorbers. Note that the halo radius can be much larger if the covering fraction of the weak absorbers is significantly lower than unity. Following the prescription detailed in Section 5 of Richter et al. (2016b), Eqn. 5 can inversely be used to obtain C_f. Assuming that the absorber's population extends out to the virial radii of galaxies with $L/L_* > 0.001$, they have derived a relation: $dN/dz = 3.6C_f$. The observed dN/dz for weak absorbers, thus, corresponds to a covering fraction of ≈ 0.3. This is roughly half of the covering fraction derived for the Si III population studied in Richter et al. (2016b). This is expected since they have noted that about half of the Si III absorber population with $\log n_H/cm^{-3} \gtrsim -3.0$ is associated with Si II absorption.

Following Stocke et al. (2013), the number of metal-rich clouds inside the characteristic radius is $N_{cl} = C_f S(\frac{R_h}{R_{cl}})^2 \approx 3 \times 10^5$, assuming the "shadowing factor" (S) and C_f to be of order unity. The volume filling factor of these clouds is then $N_{cl}(R_{cl}/R_h)^3 \approx 0.002$ (i.e. only $\approx 0.2\%$). The total gas mass ($M_{gas} = N_{cl} < M_{cl} >$) associated with these absorbers is $\sim 3 \times 10^8 M_\odot$. This mass estimate is significantly lower compared to the COS-Halos sample (i.e., $> 6 \times 10^{10} M_\odot$; Werk et al. 2014) but roughly matches with the calculation of Stocke et al. (2013) for their sample of dwarf galaxies. The mass in Silicon
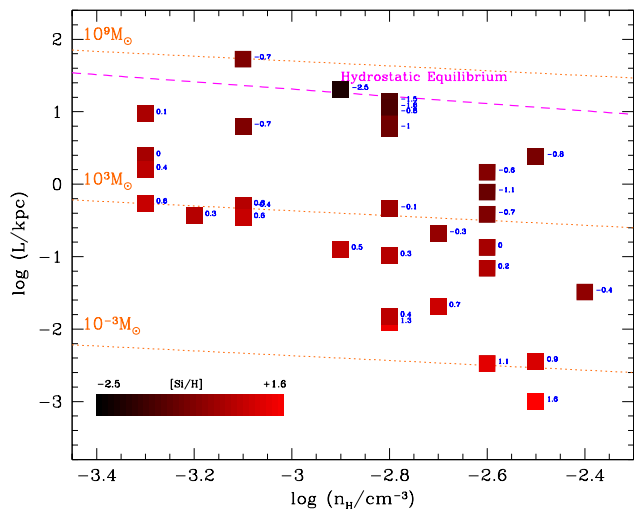
Figure 8. The line of sight thickness versus gas density as obtained from the PI models. Each data point is color-coded by the corresponding metallicity. The dashed line marks the relationship under local hydrostatic equilibrium (Schaye 2001). High metallicity systems are too small to be self-gravitating. The dotted lines indicate the lines of constant masses. The majority of the systems contain gas masses of $\lesssim 10^5 M_\odot$.

$(N_{cl} < M_{cl} >< [Si/H] > (Si/H)_\odot)$ is $\sim 10^4 M_\odot$. It corresponds to an Oxygen mass of $M_O \sim 10^5 M_\odot$, assuming solar relative abundance. This Oxygen mass estimate is ≈ 2 orders of magnitude lower than the estimate of Tumlinson et al. (2011) for the O VI absorbing gas in the COS-Halos sample. Here we note that, all our mass estimates are lower limits in the sense that we do not take the possible contribution from the high-ionization gas phase into account.

From the discussion above, it is clear that the weak absorbers may stem from extended gaseous halos that are filled with large numbers of pc–kpc-scale clouds. Given the high metallicities of the majority of the weak absorbers, it is most natural to think that they arise in large scale galactic outflows. An important question in this context is the stability of the absorbing clouds. Self-gravity and external pressure due to an ambient medium are generally thought to be the two main channels that can confine the small, metal-rich clouds (see e.g. Schaye et al. 2007). The typical size for an optically thin, self-gravitating, purely gaseous cloud with density $\sim 10^{-2.8\pm0.5}$cm^{-3} is ~ 10–30 kpc (see Eqn. 7 in Schaye et al. 2007), whereas, the median line of sight thickness of our sample is ≈ 500 pc. As demonstrated in Fig. 8, a vast majority of the weak absorbers in our sample are too tiny to be supported by self-gravity unless they are significantly dark matter dominated structures.

The presence of another gas phase, giving rise to the high-ionization metal lines, particularly the O VI, is almost certain (see Section 4.4). This phase, presumably with lower density and higher temperature, can, in principle, confine the low-ionization gas phase. However, in cases where detailed ionization modelling has been done the two phases are not found to be in pressure equilibrium (e.g. Meiring et al. 2013; Muzahid 2014; Muzahid et al. 2015b; Hussain et al. 2015). But the high-ionization gas phase traced by O VI could arise from the mixing layers of cool and an ambient medium too hot for UV line diagnostics. This hotter unobserved gas, e.g., hot halo created via accretion shocks and/or shocks due to large-scale galactic outflows, might well be the confining medium (e.g., Mulchaey & Chen 2009; Narayanan et al. 2011). Indeed, X-ray observations have revealed the presence of such a medium with
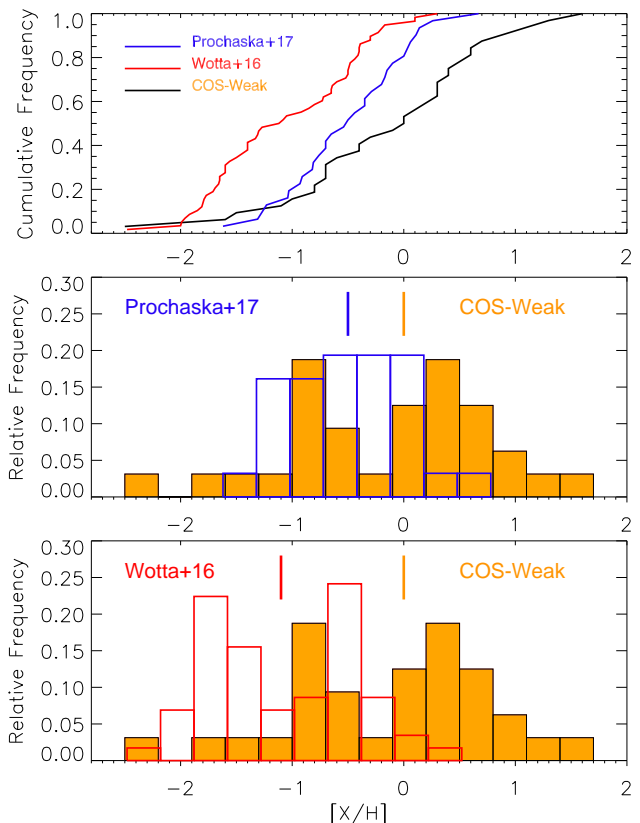
Figure 9. Bottom: Metallicity distribution of the weak absorbers in our sample (black histogram with orange shade). The red histogram in the bottom panel shows the bimodal metallicity distribution of H I-selected low-z Lyman limit systems studied by Wotta et al. (2016). The blue histogram in the middle panel shows the metallicity distribution of the COS-Halos (galaxy-selected) sample from Prochaska et al. (2017). The top panel shows the cumulative distributions of all three sample with respective colors. Both the galaxy-selected and H I-selected absorbers show very different metallicity distributions when compared to the weak absorbers. Our sample shows the highest fraction ($\approx 50\%$) of solar/super-solar metallicity absorbers.

$T > 10^6$ K in the halo of Milky Way (Gupta et al. 2012). In the absence of any confining agent, the clouds will expand freely until they reach pressure equilibrium or will eventually be evaporated. For a $\sim 10^4$ K gas cloud with $R_{cl} \sim 10^2$ pc, the free expansion time scale is $R_{cl}/c_s \sim 10^7$ yr, much shorter than the Hubble time. This suggests that the high metallicity weak absorbers could be transient in nature.

5.3 Metal Abundance

The most interesting physical properties of the weak absorbers is their unusual high metallicities. The median value of the [Si/H] distribution of 0.0 indicates that $\approx 50\%$ of the weak absorbers in our sample show a solar/super solar Si abundance. Moreover, 27/32 absorbers ($\approx 85\%$) show [Si/H] > -1.0. If we consider only $Q > 2$ systems, then the fraction of absorbers showing [Si/H] $\geqslant 0.0$ ($\geqslant -1.0$) is $\approx 44\%$ ($\approx 87\%$). Here we note that the fraction of weak absorbers showing high metallicity is significantly higher compared to the H I-selected sample of Wotta et al. (2016) and the galaxy-selected sample of Prochaska et al. (2017). In Fig. 9 we compare the metallicity distributions of these three samples. The cumulative
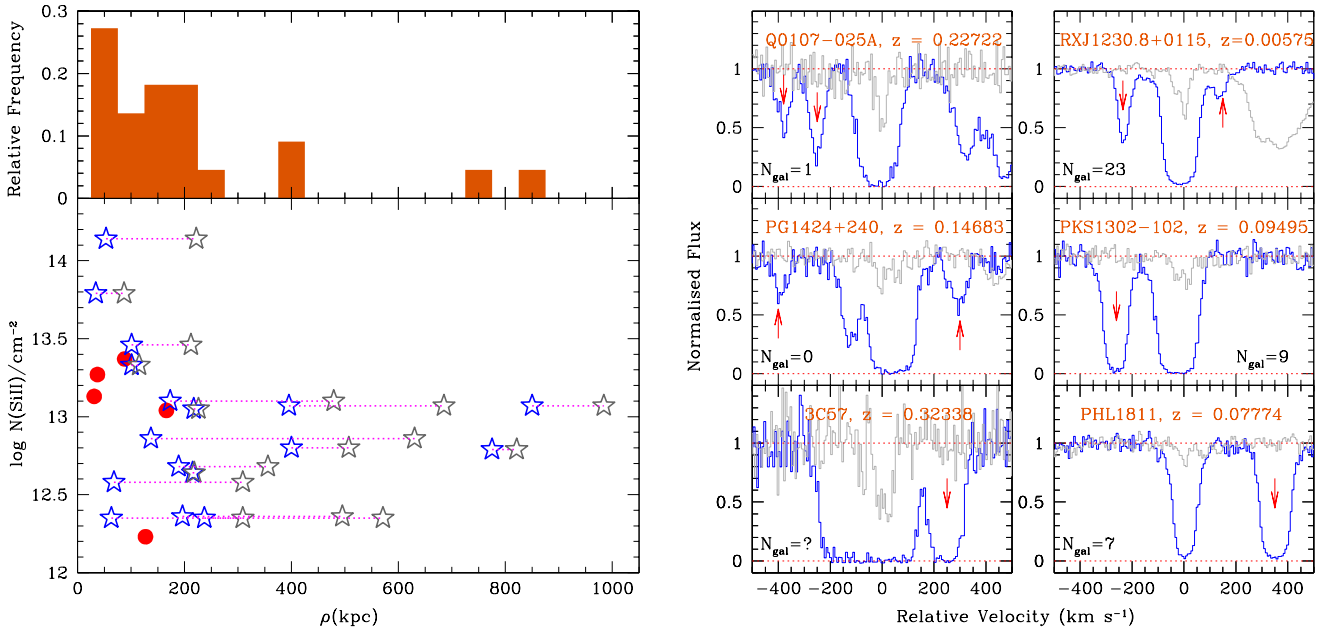
Figure 10. *Left:* The distribution of impact parameters of nearest known galaxies (top) for 22 of the weak absorbers. The impact parameter ranges from 31–850 kpc with a median value of 166 kpc. Only 3/22 absorbers show host-galaxy impact parameters < 50 kpc. In 17/22 cases at least 2 galaxies are found within 1 Mpc from the QSO sightline and within a velocity window of ± 500 km s^{-1} around the absorption redshift. In the bottom panel, the Si II column densities are plotted against the impact parameters of the nearest galaxies (blue star) and the second nearest galaxies (grey star) connected by the dotted (magenta) line. The (red) filled circles represent the galaxies that do not have a known companion. No significant correlation is seen between N(Si II) and ρ. *Right:* The H I absorption profiles of 6 weak absorbers around which different number of galaxies ($N_{\rm gal} = 0$–23) have been identified. No galaxy information is available for the system towards 3C57. The C II absorption profiles are shown in grey. Note that all of them show additional H I absorption within ± 500 km s^{-1} of the absorption redshift (0 km s^{-1}) indicated by the arrows. The presence of additional absorption clouds further suggests that they arise from a group environment (see text).

metallicity distribution, shown in the top panel, of our low-z sample is significantly different compared to that of Wotta et al. (2016). A two-sided KS-test gives $D_{\rm KS} = 0.51$ and $P_{\rm KS} = 2.1 \times 10^{-5}$ confirming that the difference has a 99.99% significance. The significance is somewhat lower ($\approx 98\%$) with a $D_{\rm KS} = 0.37$ when compared with the COS-Halos sample (Prochaska et al. 2017). The median metallicities of Wotta et al. (2016) and Prochaska et al. (2017) samples, i.e., -1.1 and -0.5 dex respectively, are much lower than our sample. Only 3/58 ($\approx 5\%$) of the absorbers in Wotta et al. (2016) and 7/31 ($\approx 22\%$) of the absorbers in Prochaska et al. (2017) have solar/super-solar metallicities. Clearly, the weak absorbers are significantly more metal-rich when compared to the galaxy-selected and H I-selected samples of absorbers probing the CGM at, by and large, similar redshifts [5].

Here we point out that both Wotta et al. (2016) and Prochaska et al. (2017) have used an UVB calculated by Haardt & Madau (2012, HM12 hereafter). The intensity of the HM12 UVB is somewhat lower than that of the KS15 UVB used in this study, for energies > 1 Ryd (see e.g., Fig. 1 of Hussain et al. 2017). In order to assess the effect of the UVB on our metallicity

estimates, we model an imaginary cloud at $z = 0.1$ with column densities of H I, Si II, and Si III equal to the corresponding median values we obtained for our sample (i.e. $10^{16.0}$, $10^{12.9}$, and $10^{13.2}$ cm^{-2}, respectively). Grids of constant density CLOUDY models were run with a solar metallicity and with a stopping N(H I) of $10^{16.0}$ cm^{-2}. The density derived for the HM12 UVB (i.e., $10^{-3.3}$cm^{-3}) is ≈ 0.4 dex lower than that obtained for the KS15 UVB. However, the metallicity obtained for the HM12 UVB (i.e., [Si/H] $= -0.14$) is only ≈ 0.1 dex lower than that derived for the KS15 UVB. Thus, overall, our metallicity estimates are consistent with those expected from the HM12 UVB.

Next, we evaluate the effect on the derived metallicity of the imaginary cloud, if some amount of Si III is contributed by the high ionization gas phase, as it might be the case for some of the absorbers studied here. We found that even if 90% of the N(Si III) is contributed by the high ionization phase (i.e. using log N(Si III)/cm^{-2} of 12.2 instead of 13.2 in the model), the derived metallicity changes only by ≈ 0.1 dex for both KS15 and HM12 incident continua. The density in such a situation is increases by ≈ 0.6 dex, as expected.

In order to investigate whether the inferred abundances of [Si/H] > 0.301 (> 2 times solar) for the 10 systems in our sample remain as high, we recalculate the metallicities and densities using a new CLOUDY grid with a super-solar metallicity of [X/H] = 0.699 (5 times solar). We find that the [Si/H] values are consistent within 0.2 dex. The densities, however, decrease by ≈ 0.6 dex leading to an increase in $N_{\rm H}$ by 0.3 dex and in line-of-sight thickness by 0.9 dex. The decrease in density for the super-solar CLOUDY grid increases the column densities for the high-ions (i.e., C IV, N V, and O VI). Nonetheless, the predicted high-ions column den-

---

[5] Note that the systems in Wotta et al. (2016) sample shows a wide range in redshift (0.08–1.09) with a median value of 0.57, which is somewhat higher than that of our sample. Nonetheless, there is no significant trend between the absorption redshift and metallicity in either sample. Moreover, the median metallicity of the 10 systems in Wotta et al. (2016) sample with $z_{\rm abs} < 0.3$ is -0.65, which is much lower than the median metallicity of our sample. Therefore the observed difference in metallicity distribution can not be attributed to difference in the redshift distributions of the two samples.

sities, particularly the N(O VI) and N(N V), are still very low (e.g., $\log N/\mathrm{cm}^{-2} < 13.5$). The predicted N(C IV) values, although increased by 0.8–1.0 dex, are still consistent with the 3σ upper limits or are lower than the observed values except for the two systems ($z_{\mathrm{abs}} = 0.00575$ towards RXJ1230.8+0115 and $z_{\mathrm{abs}} = 0.09784$ towards SDSSJ1357+1704) as already noted in Section 4.4.

Finally, besides the absolute abundances, the measurements of N(C II) allow us to calculate the relative abundance of Si relative to C, i.e., the [C/Si]. We find [C/Si] = 0.13 ± 0.18(std), which is somewhat higher albeit consistent with solar value. Our estimates of [C/Si] are generally comparable to the [C/α] measurements in solar-type stars in the Galactic disk (Gustafsson et al. 1999).

5.4 Galaxy Environments

In what types of galaxy environments do the low-z weak absorbers reside? In order to investigate, we have searched for galaxies around these absorbers in SDSS and in the literature. We have found host-galaxy information for 22/34 absorbers. In our SDSS search we have queried for galaxies with spectroscopic redshifts consistent within ±500 km s^{-1} of z_{abs} and within 1 Mpc projected separation from the QSO sightline. The SDSS spectroscopic database is 90% complete down to an r-band apparent magnitude, m_r, of 17.77 (Strauss et al. 2002; Blanton et al. 2003a). This corresponds to a luminosity of $> 1.2L_*$ at $z = 0.1$ (Blanton et al. 2003b, no K-correction has been applied). The details of the galaxies around the weak absorbers are listed in Table 4. In the left panel of Fig. 10 we show the impact parameter distribution of the nearest known galaxies which varies from 31–850 kpc. Interestingly, the median impact parameter of 166 kpc is in agreement with the halo radius (R_h) we estimated in Section 5.2. Albeit having high metallicities, only $\approx$ 14% (3/22) of the absorbers have nearest known bright galaxies within 50 kpc. However, for $\approx$ 70% of the cases a galaxy is detected within 200 kpc. We did not find any trend between N(Si II), metallicity (or density) and the impact parameter of the nearest known galaxy.

There are 26/34 fields that are covered in the SDSS footprint. We have found 75 galaxies in total in these fields (< 1 Mpc) around the weak absorbers (±500 km s^{-1}) in contrast to only 6 galaxies detected in random 26 fields[6]. It indicates a significant galaxy-overdensity around the low-z weak absorbers. Furthermore, in about $\approx$ 80% (17/22) of the cases we find 2 or more galaxies within 1 Mpc from the sightline and within a velocity window of ±500 km s^{-1} (see Table 4). All these facts suggest that *the majority of the weak absorbers live in galaxy groups*. Interestingly, as many as 23 galaxies are found around the absorber at $z_{\mathrm{abs}} = 0.00575$ towards RXJ1230.8+0115, in which the sightline passes through the Virgo cluster (Yoon & Putman 2017). In 6/26 cases the SDSS search did not yield even one galaxy that satisfied our criteria. Nonetheless, galaxies with consistent photometric redshifts are identified in all but one case. A detail study of all the galaxies listed in Table 4 will be presented in future.

If a line of sight passes through multiple galaxy halos in a group, then it is more likely to observe more than one absorption clump within the characteristic group velocity. We, thus, re-examine the ±500 km s^{-1} velocity range around the Lyα absorption in each of the weak absorbers to investigate any such possible signs of group environment. The total redshift path-length covered by this velocity

range is ≈ 0.127. From the observed $d\mathcal{N}/dz$ (Danforth et al. 2016), the expected number of random IGM H I clouds with N(H I) $> 10^{13.5}$ at $z \approx 0.1$ is 24. Intriguingly, we have found nearly 60 H I absorbers (including the 34 weak absorbers) which is $\approx$ 2.5 times higher than the number expected from random chance coincidence. As an example, the ±500 km s^{-1} spectral ranges for 6 of the weak absorbers are shown in the right panel of Fig. 10. For all of the 6 cases additional H I absorption has been detected, even when no galaxies have been identified or known in the field. It possibly suggests that all of these weak absorbers may reside in group environments even if the group environment is not apparent from the existing galaxy data. We recall here that the SDSS spectroscopic database is sensitive only to bright ($> 1.2L_*$) galaxies. A systematic survey of galaxies around these fields is thus essential.

Alternatively, or in addition, a group environment may be conducive to processes that give rise to these high metallicity clouds far from galaxy centers. A clue about the processes at work in galaxy groups is provided by the study of O VI absorbers by Pointon et al. (2017). They find that O VI is weaker and has a narrower velocity distribution for lines of sight through groups than for those near isolated galaxies. They interpret this to mean that a group is heated beyond the point where individual O VI halos would be superimposed to produce stronger absorption. They suggest that the O VI that is observed is at the interface between the hot, X-ray gas and the cooler CGM. Weak, low-ionization absorption could also be related to such an interface via thermal/hydrodynamical instabilities.

5.5 Possible Origin(s)

The high metallicity ([Si/H] $\approx$ 0.0) and solar relative abundances of heavy elements ([C/Si] $\approx$ 0.13 ± 0.18) strongly suggest that the absorbing clouds are related to star-forming regions. The impact parameters of the nearest galaxies of > 50 kpc imply that mechanisms such as galactic/AGN winds and/or tidal/ram pressure stripping of the ISM of satellite galaxies at early epochs could give rise to the cool clouds seen in absorption. Recall that the majority of the weak absorbers seems to live in a group environment in which interactions are common, and gas is often stripped from individual galaxies.

The metal-enriched, cool clouds can form in outflows predominantly via two different channels. First, metal-rich ISM clouds can be swept-up by hot wind material to the CGM by means of ram pressure and radiation pressure (e.g., Zubovas & Nayakshin 2014; McCourt et al. 2015; Schneider & Robertson 2017; Heckman et al. 2017). Second, the clouds can form *in-situ*, condensing out of the hot wind due to thermal instabilities (e.g., Field 1965; Costa et al. 2015; Voit et al. 2016; Ferrara & Scannapieco 2016; Thompson et al. 2016). Recently, McCourt et al. (2016) have suggested that an optically thin, $T \sim 10^6$ K cooling perturbation with an initial size $\gg c_s t_{\mathrm{cool}}$ (c_s is the internal sound speed, t_{cool} is the cooling time) will be fragmented quickly to a large number of cloudlets due a process called "shattering", giving rise to a "fog" like structure. These fragments are found to have a characteristic length-scale of $l_{\mathrm{cloudlet}} \sim 0.1$pc $(n_H/\mathrm{cm}^{-3})^{-1}$ as they reach a temperature of $\sim 10^4$ K. The column density of an individual cloudlet is then $N_{\mathrm{cloudlet}} = n_H l_{\mathrm{cloudlet}} \sim 10^{17.5}$ cm^{-2}. It is interesting to note that the median N_H of our sample, $\approx 10^{18.1}$ cm^{-2}, is broadly in agreement with their prediction. Here we also recall that a large number of such clouds is indeed required to match the observed $d\mathcal{N}/dz$ (see Section 5.2). These facts indicate that the "fog" like structure as suggested by McCourt et al. (2016) is consistent with the properties of the weak absorbers.

In both the situations discussed above the clouds will be

---

[6] The random 26 fields were selected by shifting the RA and Dec of the 26 quasars by 10 degree at random but making sure that they do not fall outside the SDSS footprint.

Table 4. List of galaxies around weak absorbers.

QSO	z_{abs}	Galaxy	z_{gal}	ρ(kpc)	Comments/References
PG0003+158	0.16512	SDSSJ000600.63+160908.1	0.16519	127	SDSS+ 2 Photo-z objects at 678 kpc and 876 kpc
Q0107-025A	0.22722	17.56667,-2.32678	0.2272	166	Crighton et al. (2010) + 2 Photo-z objects at 170 kpc and 921 kpc
HE0153-4520	0.22597	...	...	...	Outside SDSS
3C57	0.32338	...	...	...	Outside SDSS
SDSSJ0212-0737	0.01603	SDSSJ021213.92-073500.9	0.017471	53	SDSS
		SDSSJ021202.56-074747.7	0.016501	222	SDSS
		SDSSJ021315.80-073942.6	0.015942	278	SDSS
		SDSSJ021323.81-074355.5	0.016087	340	SDSS
		SDSSJ021327.79-074150.0	0.016701	358	SDSS
		SDSSJ021529.88-071741.5	0.016032	994	SDSS
SDSSJ0212-0737	0.13422	...	...	...	2 Photo-z objects at 796 kpc and 827 kpc
UKS-0242-724	0.06376	...	...	...	Outside SDSS
Q0349-146	0.07256	...	...	...	Outside SDSS
PKS0405-123	0.16710	61.95084, -12.18361	0.1670	101	Prochaska et al. (2006)
		61.83833, -12.19389	0.1670	115	Prochaska et al. (2006)
IRAS-F04250-5718	0.00369	...	...	...	Outside SDSS
FBQS-0751+2919	0.20399	...	...	...	...
VV2006J0808+0514	0.02930	SDSSJ080839.55+051725.9	0.030795	101	SDSS
		SDSSJ080816.43+051258.0	0.030754	212	SDSS
		SDSSJ080901.35+051832.7	0.028036	227	SDSS
		SDSSJ080857.48+052138.0	0.030555	303	SDSS
		SDSSJ080758.11+051223.6	0.029165	360	SDSS
		SDSSJ081009.39+051749.6	0.028946	783	SDSS
		SDSSJ080811.31+053514.4	0.030753	790	SDSS
PG0832+251	0.02811	SDSSJ083720.73+245627.2	0.027126	775	SDSS
		SDSSJ083720.63+250915.8	0.026954	821	SDSS
		SDSSJ083726.34+250338.8	0.028623	862	SDSS
		SDSSJ083736.98+245959.1	0.028897	943	SDSS
SDSSJ0929+4644	0.06498	SDSSJ092855.37+464345.9	0.065031	189	SDSS
		SDSSJ092849.63+464057.5	0.064019	356	SDSS
		SDSSJ092849.95+463912.0	0.064096	454	SDSS
		SDSSJ092841.92+463841.5	0.064556	548	SDSS
PMNJ1103-2329	0.08352	...	...	...	Outside SDSS
PG1116+215	0.13850	169.77779, 21.30785	0.13814	137	Tripp et al. (1998), SDSS
		169.77117, 21.25083	0.13736	630	Tripp et al. (1998)
		169.70834, 21.26972	0.13845	776	Tripp et al. (1998)
SDSSJ1122+5755	0.05319	SDSSJ112225.88+580147.3	0.052616	400	SDSS
		SDSSJ112248.77+580358.3	0.053144	507	SDSS
		SDSSJ112359.26+575248.2	0.052292	622	SDSS
		SDSSJ112227.55+580614.2	0.053132	661	SDSS
		SDSSJ112207.40+580604.3	0.052983	703	SDSS
PG1121+422	0.19238	SDSS 112428.67+420543.8	0.193994	850	SDSS
		SDSS J112445.06+415641.9	0.192222	984	SDSS
3C263	0.06350	175.02154, 65.80042	0.06322	63	Savage et al. (2012)
		174.73408, 65.87654	0.06281	571	Savage et al. (2012)
		174.74136, 65.88236	0.06285	576	Savage et al. (2012)
		175.52030, 65.81338	0.06498	956	Savage et al. (2012)
PG1202+281	0.13988	...	...	...	1 Photo-z object at 912 kpc
PG-1206+459	0.21439	NA	0.2144	31	Rosenwasser et. al, Submitted
SDSSJ1210+3157	0.05974	SDSS J121028.01+315838.1	0.059548	173	SDSS
		SDSS J121012.30+320137.3	0.059628	479	SDSS
		SDSS J121004.05+320115.2	0.060117	567	SDSS
		SDSS J120957.35+320024.6	0.058957	619	SDSS
		SDSS J121013.63+320501.4	0.060975	657	SDSS
		SDSS J121015.27+320854.7	0.059088	862	SDSS
		SDSS J120942.22+320258.8	0.058983	888	SDSS
SDSSJ1210+3157	0.14964	...	...	...	1 Photo-z object at 832 kpc
SDSSJ1214+0825	0.07407	SDSSJ121425.17+082251.8	0.073271	217	SDSS
		SDSSJ121431.23+082225.6	0.074042	226	SDSS
		SDSSJ121428.14+082225.5	0.072431	227	SDSS
		SDSSJ121439.76+082157.4	0.073442	324	SDSS
		SDSSJ121511.53+082444.3	0.073495	842	SDSS
		SDSSJ121511.14+082556.7	0.073064	831	SDSS

Table 4. Cont.

QSO	z_{abs}	Galaxy	z_{gal}	ρ(kpc)	Comments/References
RXJ1230.8+0115	0.00575	SDSSJ123246.60+013408.1	0.005088	215	SDSS
		SDSSJ123246.10+013407.8	0.005166	218	SDSS
		SDSSJ123320.76+013117.7	0.005557	227	SDSS
		SDSSJ122950.57+020153.7	0.005924	353	SDSS
		SDSSJ123227.94+002326.2	0.005051	354	SDSS
		SDSSJ123013.38+023730.5	0.00544	549	SDSS
		SDSSJ123014.49+023717.6	0.005494	553	SDSS
		SDSSJ123821.70+011207.5	0.004152	574	SDSS
		SDSSJ122902.17+024323.8	0.005221	587	SDSS
		SDSSJ123422.01+021931.4	0.005871	596	SDSS
		SDSSJ123238.38+024015.6	0.005692	619	SDSS
		SDSSJ123236.14+023932.5	0.005867	632	SDSS
		SDSSJ123251.28+023741.6	0.005911	633	SDSS
		SDSSJ122803.19+025449.7	0.004871	642	SDSS
		SDSSJ122658.50+022939.4	0.005645	649	SDSS
		SDSSJ122803.67+025434.9	0.004994	657	SDSS
		SDSSJ123434.98+023407.7	0.006155	727	SDSS
		SDSSJ123902.48+005058.9	0.005316	815	SDSS
		SDSSJ123805.17+012839.9	0.006158	832	SDSS
		SDSSJ123642.07+030630.3	0.004861	842	SDSS
		SDSSJ122329.97+020029.0	0.006051	878	SDSS
		SDSSJ122815.88+024202.9	0.007397	885	SDSS
		SDSSJ122323.40+014854.1	0.006295	895	SDSS
PKS1302-102	0.09495	196.38375, -10.56555	0.09358	68	Cooksey et al. (2008)
		196.34417, -10.58000	0.09328	309	Cooksey et al. (2008)
		196.33708, -10.58083	0.09393	350	Cooksey et al. (2008)
		196.34874, -10.50694	0.09331	386	Cooksey et al. (2008)
		196.30041, -10.57250	0.09531	548	Cooksey et al. (2008)
		196.28833, -10.61417	0.09523	715	Cooksey et al. (2008)
		196.31500, -10.46389	0.09442	728	Cooksey et al. (2008)
		196.42292, -10.44000	0.09332	756	Cooksey et al. (2008)
		196.36833, -10.42083	0.09402	852	Cooksey et al. (2008)
SDSSJ1322+4645	0.21451	NA	0.2142	37	Werk et al. (2014) + 2 Photo-z objects at 395 kpc and 821 kpc
SDSSJ1357+1704	0.09784	...	...	...	2 Photo-z objects at 303 kpc and 491 kpc
SDSSJ1419+4207	0.17885	NA	0.1792	88	Werk et al. (2014)
PG1424+240	0.12126	SDSSJ142701.72+234630.9	0.121177	196	SDSS
		SDSSJ142714.52+235007.4	0.119514	495	SDSS
PG1424+240	0.14683	...	...	...	2 Photo-z objects at 940 kpc and 950 kpc
PG-1630+377	0.17388	SDSSJ163155.09+373556.5	0.175373	395	SDSS
		SDSSJ163149.79+373438.7	0.17391	685	SDSS
PHL1811	0.07774	J215450.8-092235	0.078822	237	Keeney et al. (2017)
		J215447.5-092254	0.077671	309	Keeney et al. (2017)
		SDSSJ215506.02-091627.0	0.078655	526	SDSS
		SDSSJ215453.14-091559.2	0.077813	584	SDSS
		SDSSJ215434.62-091632.7	0.078369	766	SDSS
		SDSSJ215536.27-092017.7	0.077963	766	SDSS
		SDSSJ215437.22-091534.4	0.078117	787	SDSS
PHL1811	0.08091	J21545996-0922249	0.0808	34	Jenkins et al. (2005)
		J21545870-0923061	0.0804	87	Jenkins et al. (2005)

Notes– The impact parameters from the literature are corrected for the adopted cosmology.

metal-rich but will be subject to hydrodynamical (e.g., Rayleigh–Taylor, Kelvin–Helmholtz) instabilities (Klein et al. 1994). Moreover, cloud-wind interactions will also disrupt/shred the clouds on a "crushing" time-scale which is roughly similar to the time-scales of hydrodynamical instabilities. Radiative cooling and the presence of magnetic field can extend the lifetime of the cloud considerably (e.g., Cooper et al. 2009; McCourt et al. 2015). Next generation cosmological hydrodynamical simulations that can resolve pc-scale structures are essential for better theoretical understanding of the origins of these exciting absorbers.

6 SUMMARY

Using archival *HST*/COS spectra we have conducted a survey ("COS-Weak") of low-ionization weak metal line absorbers, with W_r(C IIλ1334) < 0.3 Å and W_r(Si IIλ1260) < 0.2 Å at $z < 0.3$, that are analogous to weak Mg II absorbers which are mostly studied at high-z. We have constructed the largest sample of weak absorber analogs that comprises of 34 absorbers, increasing the number of known/reported weak absorbers by a factor of > 5 at low-z. We have measured column densities of low- and high-ionization metal lines and of H I, performed simple photoionization models using CLOUDY, and have discussed the implications of the observed and inferred

properties of these absorbers and their galaxy environments. Our main findings are as follows:

- We estimate $d\mathcal{N}/dz = 0.8 \pm 0.2$ for our survey at $z < 0.3$, consistent with the previous study of Narayanan et al. (2005). This implies that the processes that produce the weak absorber clouds are less active at low-z than at $z \approx 1$ (Section 3.1 & 5.1).

- Our simple photoionization models assumed Si III and Si II arise in the same phase, and that most/all of the H I absorption is also in this phase. Absorber densities range from $10^{-3.3}$ to $10^{-2.4}$ cm^{-3}, with a median of $10^{-2.8}$ cm^{-3}. Metallicities, represented as [Si/H], ranged from -2.5 to 1.6, with a median of 0.0. The line of sight thicknesses of the clouds ranged from 1 pc to 53 kpc. The neutral hydrogen column densities range from $\log N(\text{H I})/\text{cm}^{-2}$ of 14–18, and the total hydrogen column densities $\log N_{\text{H}}/\text{cm}^{-2}$ from 16–20. There is an anti-correlation between [Si/H] and $N(\text{H I})$. Although this is partly a selection effect for small $N(\text{H I})$, it is clear that the highest metallicities do arise in environments that do not have a large amount of neutral hydrogen nearby to dilute the metals (Fig. 7).

- At least two thirds of the absorbers have a separate, hotter and/or higher ionization phase with C IV and/or O VI absorption detected. In several cases C IV can arise in the same phase with the Si II/C II, but generally when it is detected a separate phase is needed. O VI must always arise in a different phase (Section 4.4).

- We find that the highest metallicity systems are the tiniest in size (Fig. 8). The majority of these absorbers have (gas) masses ($< 10^5 M_\odot$) too small to be in local hydrostatic equilibrium unless they are significantly dark matter dominated structures. In the absence of any confining medium these absorbers will be evaporated on the free expansion time-scale of $\sim 10^7$ yr.

- The weak absorbers outnumber bright galaxies by tens of thousands in one, suggesting that the population must be huge. Nonetheless, they carry a negligible fraction of cosmic baryons. Adopting the geometrical model for CGM absorbers prescribed by Richter et al. (2016a), we obtain a covering fraction of $\approx 30\%$ for the weak absorbers, assuming that the population extends out to the virial radii of galaxies with $L/L_* > 0.001$ (Section 5.2).

- The weak absorber population is found to be significantly more metal-rich compared to the H I-selected (Wotta et al. 2016) and galaxy-selected (Prochaska et al. 2017) samples of absorbers probing the CGM at similar redshift (Section 5.3).

- We have searched for galaxies around these absorbers in SDSS and in the literature and found that they live in regions of significant galaxy over-density. In about 80% of the cases, more than one galaxy is detected within 1 Mpc from the QSO sightline and within ± 500 km s^{-1} of the absorber's redshift. The impact parameters of the nearest known galaxies range from ≈ 31–850 kpc with a median of 166 kpc. In $\approx 70\%$ of the cases the nearest galaxy is detected within 200 kpc. It implies that the weak absorbers are abundant in the halos of galaxies that are in group environments (Section 5.4).

The origin of these metal-rich, compact structures, apart from galaxies, remains unclear, but we suggest that they are transient structures in the halos of galaxies most of which live in group environments and they are related to outflows and/or to stripping of metal-rich gas from the galaxies. A systematic search for galaxies in these fields and next generation cosmological simulations with the capability of resolving pc-scale structures are essential for further insights into the nature and origin of these fascinating cosmic structures.

REFERENCES

Adelberger K. L., Shapley A. E., Steidel C. C., Pettini M., Erb D. K., Reddy N. A., 2005, ApJ, 629, 636

Asplund M., Grevesse N., Sauval A. J., Scott P., 2009, ARA&A, 47, 481

Becker G. D., Sargent W. L. W., Rauch M., Carswell R. F., 2012, ApJ, 744, 91

Bergeron J., 1986, A&A, 155, L8

Bergeron J., Boissé P., 1991, A&A, 243, 344

Blanton M. R., Lin H., Lupton R. H., Maley F. M., Young N., Zehavi I., Loveday J., 2003a, AJ, 125, 2276

Blanton M. R., et al., 2003b, ApJ, 592, 819

Bond N. A., Churchill C. W., Charlton J. C., Vogt S. S., 2001, ApJ, 562, 641

Bordoloi R., et al., 2014, ApJ, 796, 136

Bosman S. E. I., Becker G. D., Haehnelt M. G., Hewett P. C., McMahon R. G., Mortlock D. J., Simpson C., Venemans B. P., 2017, MNRAS, 470, 1919

Bouché N., Hohensee W., Vargas R., Kacprzak G. G., Martin C. L., Cooke J., Churchill C. W., 2012, MNRAS, 426, 801

Charlton J. C., Churchill C. W., 1998, ApJ, 499, 181

Charlton J. C., Ding J., Zonak S. G., Churchill C. W., Bond N. A., Rigby J. R., 2003, ApJ, 589, 111

Chen H.-W., Mulchaey J. S., 2009, ApJ, 701, 1219

Chen H.-W., Helsby J. E., Gauthier J.-R., Shectman S. A., Thompson I. B., Tinker J. L., 2010, ApJ, 714, 1521

Chen S.-F. S., et al., 2016, preprint, (arXiv:1612.02829)

Churchill C. W., Rigby J. R., Charlton J. C., Vogt S. S., 1999, ApJS, 120, 51

Churchill C. W., Vogt S. S., Charlton J. C., 2003, AJ, 125, 98

Churchill C. W., Kacprzak G. G., Steidel C. C., 2005, in Williams P., Shu C.-G., Menard B., eds, IAU Colloq. 199: Probing Galaxies through Quasar Absorption Lines. pp 24–41, doi:10.1017/S1743921305002401

Churchill C. W., Kacprzak G. G., Steidel C. C., Spitler L. R., Holtzman J., Nielsen N. M., Trujillo-Gomez S., 2012, ApJ, 760, 68

Codoreanu A., Ryan-Weber E. V., Crighton N. H. M., Becker G., Pettini M., Madau P., Venemans B., 2017, preprint, (arXiv:1708.00304)

Cooksey K. L., Prochaska J. X., Chen H.-W., Mulchaey J. S., Weiner B. J., 2008, ApJ, 676, 262

Cooper J. L., Bicknell G. V., Sutherland R. S., Bland-Hawthorn J., 2009, ApJ, 703, 330

Costa T., Sijacki D., Haehnelt M. G., 2015, MNRAS, 448, L30

Crighton N. H. M., Morris S. L., Bechtold J., Crain R. A., Jannuzi B. T., Shone A., Theuns T., 2010, MNRAS, 402, 1273

Danforth C. W., Stocke J. T., Shull J. M., 2010, ApJ, 710, 613

Danforth C. W., et al., 2016, ApJ, 817, 111

Dutta R., Srianand R., Gupta N., Joshi R., 2017, MNRAS, 468, 1029

Fang T., Danforth C. W., Buote D. A., Stocke J. T., Shull J. M., Canizares C. R., Gastaldello F., 2014, ApJ, 795, 57

Ferland G. J., et al., 2013, Rev. Mexicana Astron. Astrofis., 49, 137

Ferrara A., Scannapieco E., 2016, ApJ, 833, 46

Field G. B., 1965, ApJ, 142, 531

Furniss A., et al., 2013, ApJ, 768, L31

Gaikwad P., Khaire V., Choudhury T. R., Srianand R., 2016, preprint, (arXiv:1605.02738)

Gauthier J.-R., 2013, MNRAS, 432, 1444

Green J. C., et al., 2012, ApJ, 744, 60

Gupta A., Mathur S., Krongold Y., Nicastro F., Galeazzi M., 2012, ApJ, 756, L8

Gustafsson B., Karlsson T., Olsson E., Edvardsson B., Ryde N., 1999, A&A, 342, 426

Haardt F., Madau P., 1996, ApJ, 461, 20

Haardt F., Madau P., 2012, ApJ, 746, 125

Heckman T., Borthakur S., Wild V., Schiminovich D., Bordoloi R., 2017, preprint, (arXiv:1707.05933)

Herenz P., Richter P., Charlton J. C., Masiero J. R., 2013, A&A, 550, A87

Hussain T., Muzahid S., Narayanan A., Srianand R., Wakker B. P., Charlton J. C., Pathak A., 2015, MNRAS, 446, 2444

Hussain T., Khaire V., Srianand R., Muzahid S., Pathak A., 2017, MNRAS, 466, 3133

Jenkins E. B., Bowen D. V., Tripp T. M., Sembach K. R., Leighly K. M., Halpern J. P., Lauroesch J. T., 2003, AJ, 125, 2824

Jenkins E. B., Bowen D. V., Tripp T. M., Sembach K. R., 2005, ApJ, 623, 767

Johnson S. D., Chen H.-W., Mulchaey J. S., 2015, MNRAS, 449, 3263

Joshi R., Srianand R., Petitjean P., Noterdaeme P., 2017, preprint, (arXiv:1706.03075)

Kacprzak G. G., Churchill C. W., Steidel C. C., Murphy M. T., 2008, AJ, 135, 922

Kacprzak G. G., Churchill C. W., Steidel C. C., Spitler L. R., Holtzman J. A., 2012a, MNRAS, 427, 3029

Kacprzak G. G., Churchill C. W., Nielsen N. M., 2012b, ApJ, 760, L7

Kacprzak G. G., Muzahid S., Churchill C. W., Nielsen N. M., Charlton J. C., 2015, ApJ, 815, 22

Keeney B. A., Danforth C. W., Stocke J. T., France K., Green J. C., 2012, PASP, 124, 830

Keeney B. A., et al., 2017, ApJS, 230, 6

Khaire V., Srianand R., 2015a, MNRAS, 451, L30

Khaire V., Srianand R., 2015b, ApJ, 805, 33

Klein R. I., McKee C. F., Colella P., 1994, ApJ, 420, 213

Kriss G. A., 2011, Technical report, Improved Medium Resolution Line Spread Functions for COS FUV Spectra

Lacki B. C., Charlton J. C., 2010, MNRAS, 403, 1556

Lanzetta K. M., Turnshek D. A., Wolfe A. M., 1987, ApJ, 322, 739

Lynch R. S., Charlton J. C., 2007, ApJ, 666, 64

Matejek M. S., Simcoe R. A., 2012, ApJ, 761, 112

Mathes N. L., Churchill C. W., Murphy M. T., 2017, preprint, (arXiv:1701.05624)

McCourt M., O'Leary R. M., Madigan A.-M., Quataert E., 2015, MNRAS, 449, 2

McCourt M., Oh S. P., O'Leary R. M., Madigan A.-M., 2016, preprint, (arXiv:1610.01164)

Meiring J. D., Tripp T. M., Werk J. K., Howk J. C., Jenkins E. B., Prochaska J. X., Lehner N., Sembach K. R., 2013, ApJ, 767, 49

Milutinović N., Rigby J. R., Masiero J. R., Lynch R. S., Palma C., Charlton J. C., 2006, ApJ, 641, 190

Misawa T., Charlton J. C., Narayanan A., 2008, ApJ, 679, 220

Morton D. C., 2003, ApJS, 149, 205

Mulchaey J. S., Chen H.-W., 2009, ApJ, 698, L46

Muzahid S., 2014, ApJ, 784, 5

Muzahid S., Srianand R., Savage B. D., Narayanan A., Mohan V., Dewangan G. C., 2012, MNRAS, 424, L59

Muzahid S., Srianand R., Arav N., Savage B. D., Narayanan A., 2013, MNRAS, 431, 2885

Muzahid S., Srianand R., Charlton J., 2015a, MNRAS, 448, 2840

Muzahid S., Kacprzak G. G., Churchill C. W., Charlton J. C., Nielsen N. M., Mathes N. L., Trujillo-Gomez S., 2015b, ApJ, 811, 132

Narayanan A., Charlton J. C., Masiero J. R., Lynch R., 2005, ApJ, 632, 92

Narayanan A., Misawa T., Charlton J. C., Kim T.-S., 2007, ApJ, 660, 1093

Narayanan A., Charlton J. C., Misawa T., Green R. E., Kim T.-S., 2008, ApJ, 689, 782

Narayanan A., Savage B. D., Wakker B. P., 2010, ApJ, 712, 1443

Narayanan A., et al., 2011, ApJ, 730, 15

Nestor D. B., Turnshek D. A., Rao S. M., 2005, ApJ, 628, 637

Nestor D. B., Turnshek D. A., Rao S. M., Quider A. M., 2007, ApJ, 658, 185

Nielsen N. M., Churchill C. W., Kacprzak G. G., Murphy M. T., 2013a, ApJ, 776, 114

Nielsen N. M., Churchill C. W., Kacprzak G. G., 2013b, ApJ, 776, 115

Osterman S., et al., 2011, Ap&SS, 335, 257

Petitjean P., Bergeron J., 1990, A&A, 231, 309

Pettini M., Ellison S. L., Steidel C. C., Bowen D. V., 1999, ApJ, 510, 576

Pettini M., Ellison S. L., Bergeron J., Petitjean P., 2002, A&A, 391, 21

Pointon S. K., Nielsen N. M., Kacprzak G. G., Muzahid S., Churchill C. W., Charlton J. C., 2017, ApJ, 844, 23

Prochaska J. X., Chen H.-W., Howk J. C., Weiner B. J., Mulchaey J., 2004, ApJ, 617, 718

Prochaska J. X., Weiner B. J., Chen H.-W., Mulchaey J. S., 2006, ApJ, 643, 680

Prochaska J. X., et al., 2017, ApJ, 837, 169

Prochter G. E., Prochaska J. X., Burles S. M., 2006, ApJ, 639, 766

Ribaudo J., Lehner N., Howk J. C., Werk J. K., Tripp T. M., Prochaska J. X., Meiring J. D., Tumlinson J., 2011, ApJ, 743, 207

Richter P., et al., 2016a, preprint, (arXiv:1611.07024)

Richter P., Wakker B. P., Fechner C., Herenz P., Tepper-García T., Fox A. J., 2016b, A&A, 590, A68

Rigby J. R., Charlton J. C., Churchill C. W., 2002, ApJ, 565, 743

Savage B. D., et al., 2010, ApJ, 719, 1526

Savage B. D., Narayanan A., Lehner N., Wakker B. P., 2011, ApJ, 731, 14

Savage B. D., Kim T.-S., Keeney B., Narayanan A., Stocke J., Syphers D., Wakker B. P., 2012, ApJ, 753, 80

Schaye J., 2001, ApJ, 562, L95

Schaye J., Carswell R. F., Kim T., 2007, MNRAS, 379, 1169

Schneider E. E., Robertson B. E., 2017, ApJ, 834, 144

Sembach K. R., Tripp T. M., Savage B. D., Richter P., 2004, ApJS, 155, 351

Shull J. M., Moloney J., Danforth C. W., Tilton E. M., 2015, ApJ, 811, 3

Steidel C. C., Sargent W. L. W., 1992, ApJS, 80, 1

Steidel C. C., Erb D. K., Shapley A. E., Pettini M., Reddy N., Bogosavljević M., Rudie G. C., Rakic O., 2010, ApJ, 717, 289

Stocke J. T., Keeney B. A., Danforth C. W., Shull J. M., Froning C. S., Green J. C., Penton S. V., Savage B. D., 2013, ApJ, 763, 148

Strauss M. A., et al., 2002, AJ, 124, 1810

Thompson T. A., Quataert E., Zhang D., Weinberg D. H., 2016, MNRAS, 455, 1830

Tripp T. M., Lu L., Savage B. D., 1998, ApJ, 508, 200

Tripp T. M., et al., 2011, Science, 334, 952

Tumlinson J., et al., 2011, ApJ, 733, 111

Turner M. L., Schaye J., Steidel C. C., Rudie G. C., Strom A. L., 2014, MNRAS, 445, 794

Voit G. M., Meece G., Li Y., O'Shea B. W., Bryan G. L., Donahue M., 2016, preprint, (arXiv:1607.02212)

Werk J. K., Prochaska J. X., Thom C., Tumlinson J., Tripp T. M., O'Meara J. M., Peeples M. S., 2013, ApJS, 204, 17

Werk J. K., et al., 2014, ApJ, 792, 8

Wotta C. B., Lehner N., Howk J. C., O'Meara J. M., Prochaska J. X., 2016, ApJ, 831, 95

Yoon J. H., Putman M. E., 2017, ApJ, 839, 117

Zahedy F. S., Chen H.-W., Gauthier J.-R., Rauch M., 2017, MNRAS, 466, 1071

Zhu G., Ménard B., 2013, ApJ, 770, 130

Zibetti S., Ménard B., Nestor D. B., Quider A. M., Rao S. M., Turnshek D. A., 2007, ApJ, 658, 161

Zubovas K., Nayakshin S., 2014, MNRAS, 440, 2625

This paper has been typeset from a TEX/LATEX file prepared by the author.

APPENDIX A: CONNECTION TO WEAK Mg II ABSORBERS

In this Appendix we revisit the connection between Si II and Mg II absorption and confirm that our selection criteria are indeed well suited for studying the weak Mg II absorbers at $z < 0.3$ in the absence of spectral coverage for the Mg II doublet.

In Section 1, we have argued that Si II is a good proxy for Mg II. The top panel of Fig. A1 further strengthens our argument. For typical $N(H I)$ and [X/H] it shows that Si II traces Mg II for a wide range of densities relevant for these absorbers. In the bottom panel, the $N(Mg II)$ values predicted by our adopted PI models are plotted against the observed $N(Si II)$. As expected, a statistically significant correlation is seen between these two quantities. The predicted $N(Mg II)$ values are in the range of $10^{11.6-13.8}$ cm^{-2} with a median of $10^{12.3}$ cm^{-2}. An equivalent width of 0.3 Å corresponds to a column density of $10^{12.84}$ cm^{-2} (indicated by the red horizontal line) for the Mg IIλ2796 line on the linear part of the COG. A vast majority (28/32) of the systems show $N(Mg II) < 12.84$, indicating that these are truly analogous to the weak Mg II absorbers that are primarily studied at high-z.

APPENDIX B: SUPPLEMENTARY LISTS

APPENDIX C: VELOCITY PLOTS AND SYSTEM DESCRIPTIONS
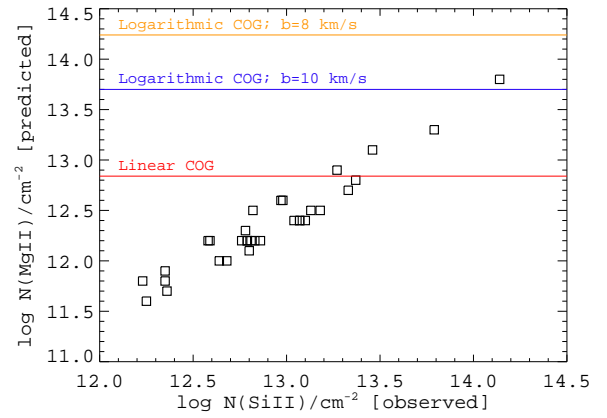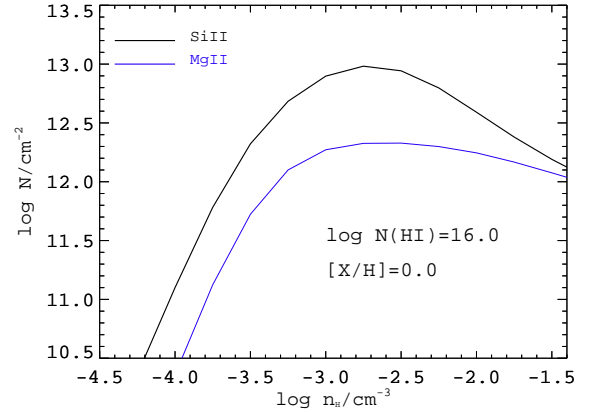
Figure A1. Top: CLOUDY predicted column densities of Si II (black) and Mg II (blue) as a function of density. The model is run with a stopping $N(H I)$ of 10^{16} cm^{-2} and with a solar metallicity. Si II and Mg II closely follow each other for a wide range in density. Bottom: The model predicted Mg II column densities, listed in the last column of Table 2, against the observed Si II column densities. As expected from the top panel, a tight correlation ($\rho_s = 0.92$, $\rho_s/\sigma = 5.2$) between $N(Mg II)$ and $N(Si II)$ is seen. The horizontal lines correspond to the maximum $N(Mg II)$ for an weak Mg II absorber with $W_r(Mg II\lambda2796) < 0.3$ Å, provided the line falls on the linear part of the COG or logarithmic part of the COG with $b = 10$ and 8 km s^{-1}. Clearly, all of these absorbers are consistent with being weak Mg II absorbers' analogs.

Table B1. List of QSO spectra with S/N > 5 per pixel searched for weak Mg II analogs. The full list is available as "online only" material.

QSO (1)	RA (2)	Dec (3)	z_{qso} (4)	Gratings (5)	z_{min} (6)	z_{max} (7)	$(S/N)_{G130M}$ (8)	$(S/N)_{G160M}$ (9)	Flag (10)	PID (11)
PHL2525	0.10167	-12.76333	0.199	3	0.000	0.179	12	8	1	12604
PG0003+158	1.49683	16.16361	0.451	3	0.000	0.343	15	9	1	12038
MRK335	1.58125	20.20278	0.025	3	0.000	0.008	16	11	1	11524
SDSSJ0012-1022	3.10004	-10.37403	0.228	3	0.000	0.208	5	3	0	12248
QSO-B0026+129	7.30712	13.26778	0.142	1	0.000	0.086	11	-1	1	12569
HS-0033+4300	9.09575	43.27786	0.120	3	0.025	0.101	6	6	1	11632
SDSSJ0042-1037	10.59287	-10.62883	0.424	3	0.000	0.343	6	5	0	11598
PG0044+030	11.77458	3.33194	0.623	1	0.000	0.099	6	-1	1	12275
IO-AND	12.07908	39.68656	0.134	3	0.025	0.115	8	7	1	11632
QSO-B0050+124	13.39567	12.69331	0.059	1	0.000	0.040	10	-1	1	12569
HE0056-3622	14.65567	-36.10133	0.164	3	0.000	0.145	17	13	1	12604
RBS144	15.11296	-51.23172	0.062	3	0.000	0.044	13	10	1	12604
J0101+4229	15.37971	42.49322	0.190	3	0.025	0.170	6	5	1	11632
Q0107-025A	17.55475	-2.33136	0.960	3	0.000	0.347	10	12	1	11585
Q0107-0232	17.56012	-2.28267	0.728	2	0.135	0.349	-1	10	1	11585
Q0107-025B	17.56771	-2.31417	0.956	3	0.000	0.346	9	11	1	11585
B0117-2837	19.89871	-28.35872	0.349	3	0.000	0.345	15	17	1	12204
TONS210	20.46463	-28.34939	0.116	3	0.000	0.097	28	18	1	12204
B0120-28	20.65317	-28.72258	0.436	3	0.086	0.342	12	8	1	12204
FAIRALL9	20.94071	-58.80578	0.047	3	0.000	0.030	27	26	1	12604

Notes– (1) QSO name sorted by increasing RA; (2) Right-ascension (J2000); (3) Declination (J2000); (4) QSO redshift; (5) COS gratings used for observations, 1: G130M, 2: G160M, 3: G130M+160M; (6) Minimum search redshift; (7) Maximum search redshift; (8) S/N of the G130M data estimated near 1400 Å (−1 when data are not available); (9) S/N of the G160M data estimated near 1600 Å (−1 when data are not available); (10) Spectrum flag, 1: part of the statistical sample, 2: not part of the statistical sample; (11) *HST* proposal ID.

Table B2. List of QSO spectra with S/N < 5 per pixel that are not used in this study. The full list is available as "online only" material.

QSO (1)	RA (2)	Dec (3)	z_{qso} (4)	Gratings (5)	z_{min} (6)	z_{max} (7)	$(S/N)_{G130M}$ (8)	$(S/N)_{G160M}$ (9)	Fl ag (10)	PID (11)
QSO-B0007+107	2.62925	10.97486	0.089	1	0.000	0.071	2	-1	1	12569
SDSSJ0242-0759	40.71188	-7.98728	0.172	3	0.000	0.152	4	4	0	12248
SDSSJ0843+4117	130.95620	41.29489	0.990	3	0.000	0.330	3	3	0	12248
VV2006J0852+0313	133.24675	3.22239	0.297	1	0.000	0.099	4	-1	0	12603
J0904P4007	136.09713	40.11797	0.411	2	0.108	0.323	-1	4	1	13423
SDSSJ0910+1014	137.62396	10.23711	0.463	3	0.000	0.345	4	4	0	11598
SDSSJ0912+2957	138.14758	29.95706	0.305	3	0.000	0.283	4	3	0	12248
VV2006J0914+0837	138.63238	8.62853	0.648	1	0.000	0.100	4	-1	0	12603
SDSSJ0930+2848	142.50791	28.81622	0.487	1	0.000	0.102	3	-1	0	12603
SDSSJ0935+0204	143.82578	2.07097	0.650	3	0.000	0.345	4	3	0	11598
VV2000J0936+3207	144.01617	32.11925	1.150	1	0.000	0.097	2	-1	0	12603
SDSSJ0937+1700	144.27854	17.00597	0.506	1	0.000	0.098	4	-1	0	12603
SDSSJ0943+0531	145.88170	5.52539	0.564	3	0.000	0.344	4	4	0	11598
SDSSJ0951+3307	147.78800	33.12939	0.644	1	0.000	0.102	3	-1	1	12486
BZBJ1001+2911	150.29254	29.19375	0.558	3	0.000	0.324	3	3	1	13008
VV96J1002+3240	150.72713	32.67753	0.829	1	0.000	0.100	3	-1	0	12603
2MASXJ1005-2417	151.38628	-24.28781	0.154	3	0.000	0.135	3	2	0	13347
J1010P2559	152.62725	25.99706	0.512	2	0.108	0.319	-1	4	1	13423
2MASSJ1013+0500	153.32487	5.00950	0.266	1	0.000	0.101	3	-1	0	12603
2MASSJ1015-2748	153.99683	-27.80800	0.102	3	0.000	0.084	4	2	0	13347

Notes– (1) QSO name; (2) Right-ascension (J2000); (3) Declination (J2000); (4) QSO redshift; (5) COS gratings used for observations, 1: G130M, 2: G160M, 3: G130M+160M; (6) Minimum search redshift; (7) Maximum search redshift; (8) S/N of the G130M data estimated near 1400 Å (−1 when data are not available); (9) S/N of the G160M data estimated near 1600 Å (−1 when data are not available); (10) Spectrum flag, 1: part of the statistical sample, 2: not part of the statistical sample; (11) *HST* proposal ID.

Table B3. List of strong C II/Si II systems. These systems are *not* part of the sample studied here.

QSO	RA	Dec	z_{qso}	z_{abs}	Gratings	z_{min}	z_{max}	$(S/N)_{G130M}$	$(S/N)_{G160M}$	Flag	PID
(1)	(2)	(3)	(4)	(5)	(6)	(7)	(8)	(9)	(10)	(11)	(12)
SDSSJ0012-1022	3.10004	-10.37403	0.228	0.22936	3	0.000	0.208	5	3	0	12248
SDSSJ0042-1037	10.59287	-10.62883	0.424	0.09487	3	0.000	0.343	6	5	0	11598
B0120-28	20.65317	-28.72258	0.436	0.18538	3	0.086	0.342	12	8	1	12204
PHL1226	28.61662	4.80519	0.404	0.01795	1	0.000	0.101	8	-1	1	12536
SDSSJ0155-0857	28.87509	-8.95111	0.165	0.16412	3	0.000	0.146	6	5	0	12248
VV2006J0159+1345	29.97067	13.76511	0.503	0.04419	1	0.000	0.100	6	-1	0	12603
Q0244-303	41.70779	-30.12814	0.530	0.00461	1	0.000	0.099	5	-1	1	12988
PG0832+251	128.89917	24.99472	0.329	0.01750	3	0.000	0.307	7	8	1	12025
Q0850+440	133.39266	43.81730	0.515	0.16368	3	0.000	0.329	13	6	0	13398
SDSSJ0925+4004	141.47793	40.07058	0.471	0.24766	3	0.000	0.344	4	5	0	11598
SDSSJ0928+6025	142.15824	60.42250	0.295	0.15384	3	0.000	0.273	4	5	0	11598
SDSSJ0930+2848	142.50791	28.81622	0.487	0.02284	1	0.000	0.102	3	-1	0	12603
SDSSJ0950+4831	147.50304	48.52481	0.589	0.21168	3	0.000	0.345	7	5	0	11598
SDSSJ0951+3307	147.78800	33.12939	0.644	0.00534	1	0.000	0.102	3	-1	1	12486
2MASSJ0951+3542	147.84971	35.71361	0.398	0.04435	1	0.009	0.103	7	-1	0	12603
SDSSJ0959+0503	149.81521	5.06531	0.162	0.05888	3	0.000	0.143	6	5	0	12248
SDSSJ1001+5944	150.26062	59.73730	0.746	0.30358	3	0.000	0.345	10	5	0	12248
SDSSJ1009+0713	152.25858	7.22883	0.456	0.11398	3	0.000	0.345	5	5	0	11598
J1010P2559	152.62725	25.99706	0.512	0.24464	2	0.108	0.319	-1	4	1	13423
SDSSJ1016+4706	154.09417	47.11203	0.821	0.16582	3	0.000	0.345	5	5	0	11598
SDSSJ1016+4706	154.09417	47.11203	0.821	0.25257	3	0.000	0.345	5	5	0	11598
Q1022+393	155.65591	39.53069	0.603	0.25225	2	0.121	0.328	4	-1	0	12593
SDSSJ1047+1304	161.79096	13.08183	0.400	0.00279	1	0.000	0.079	4	-1	1	12198
SDSSJ1112+3539	168.16296	35.65783	0.653	0.02480	3	0.000	0.345	4	4	0	11598
SDSSJ1117+2634	169.47630	26.57128	0.421	0.04747	3	0.000	0.326	6	5	0	12248
VV2006J1120+0413	170.02078	4.22314	0.544	0.04993	1	0.000	0.101	5	-1	0	12603
SDSSJ1133+0327	173.36576	3.45531	0.524	0.23733	3	0.000	0.345	5	3	0	11598
PG1216+069	184.83720	6.64403	0.331	0.00634	3	0.000	0.309	14	7	1	12025
SDSSJ1233+4758	188.39613	47.96678	0.381	0.22193	3	0.000	0.344	8	4	0	11598
SDSSJ1241+2852	190.37350	28.87000	0.589	0.06667	1	0.000	0.098	5	-1	0	12603
SDSSJ1241+5721	190.47508	57.35203	0.583	0.20558	3	0.000	0.345	7	6	0	11598/13033
VV2006J1305+0357	196.35108	3.95858	0.545	0.00144	1	0.000	0.101	7	-1	0	12603
CSO-0873	199.98433	27.46894	1.015	0.28899	2	0.252	0.329	10	-1	0	11667
SDSSJ1330+2813	202.68813	28.22261	0.417	0.19227	3	0.000	0.345	6	5	0	11598
SDSSJ1342+0505	205.52733	5.08994	0.266	0.13943	3	0.000	0.245	7	5	0	12248
SDSSJ1342-0053	205.71500	0.89592	0.326	0.07133	3	0.000	0.304	7	6	0	11598
SDSSJ1342-0053	205.71500	0.89592	0.326	0.22745	3	0.000	0.304	7	6	0	11598
SDSSJ1407+5507	211.88437	55.12378	1.026	0.00477	1	0.000	0.101	8	-1	1	12486
SDSSJ1410+2304	212.66001	23.07978	0.795	0.20962	3	0.000	0.340	7	6	1	12958
QSO-B1411+4414	213.45137	44.00389	0.089	0.08286	1	0.000	0.071	13	-1	1	12569
SDSSJ1415+1634	213.92876	16.57050	0.742	0.00770	1	0.000	0.085	10	-1	1	12486
SDSSJ1435+3604	218.79803	36.07700	0.428	0.20267	3	0.000	0.345	5	3	0	11598
SDSSJ1512+0128	228.15438	1.47944	0.265	0.02938	1	0.000	0.100	3	-1	0	12603
SDSSJ1553+3548	238.27050	35.80795	0.721	0.08292	3	0.000	0.344	7	4	0	11598
SDSSJ1555+3628	238.76830	36.48000	0.714	0.18915	3	0.000	0.345	5	3	0	11598
SDSSJ1616+4154	244.20590	41.90453	0.440	0.32098	3	0.077	0.345	6	5	0	11598
SDSSJ1619+3342	244.81894	33.71067	0.470	0.09638	3	0.000	0.345	10	10	0	11598
IRAS-F22456-5125	342.17165	-51.16475	0.100	0.09937	3	0.000	0.082	32	16	1	11686

Notes– (1) QSO name; (2) Right-ascension (J2000); (3) Declination (J2000); (4) QSO redshift; (5) Absorption redshift; (6) COS gratings used for observations, 1: G130M, 2: G160M, 3: G130M+160M; (7) Minimum search redshift; (8) Maximum search redshift; (9) S/N of the G130M data estimated near 1400 Å; (10) S/N of the G160M data estimated near 1600 Å. S/N is −1 when data are not available; (11) Spectrum flag, 1: part of the statistical sample, 0: not part of the statistical sample; (12) *HST* proposal ID.

Table B4. List of weak Mg ɪɪ analogs that are intrinsic to the background QSO. These systems are *not* part of the sample studied here.

QSO (1)	RA (2)	Dec (3)	z_{qso} (4)	z_{abs} (5)	Gratings (6)	z_{min} (7)	z_{max} (8)	$(S/N)_{G130M}$ (9)	$(S/N)_{G160M}$ (10)	Flag (11)	PID (12)
SDSSJ0012-1022	3.10004	-10.37403	0.228	0.22936	3	0.000	0.208	5	3	0	12248
SDSSJ0155-0857	28.87509	-8.95111	0.165	0.16412	3	0.000	0.146	6	5	0	12248
QSO-B1411+4414	213.45137	44.00389	0.089	0.08286	1	0.000	0.071	13	–	1	12569
IRAS-F22456-5125	342.17165	-51.16475	0.100	0.09937, 0.09592	3	0.000	0.082	32	16	1	11686

Notes– (1) QSO name; (2) Right-ascension (J2000); (3) Declination (J2000); (4) QSO redshift; (5) Absorption redshift; (6) COS gratings used for observations, 1: G130M, 2: G160M, 3: G130M+160M; (7) Minimum search redshift; (8) Maximum search redshift; (9) S/N of the G130M data estimated near 1400 Å; (10) S/N of the G160M data estimated near 1600 Å (blank when data are not available); (11) Spectrum flag, 1: part of the statistical sample, 0: not part of the statistical sample; (12) *HST* proposal ID.

PG0003+158 (z_{abs} = 0.16512)
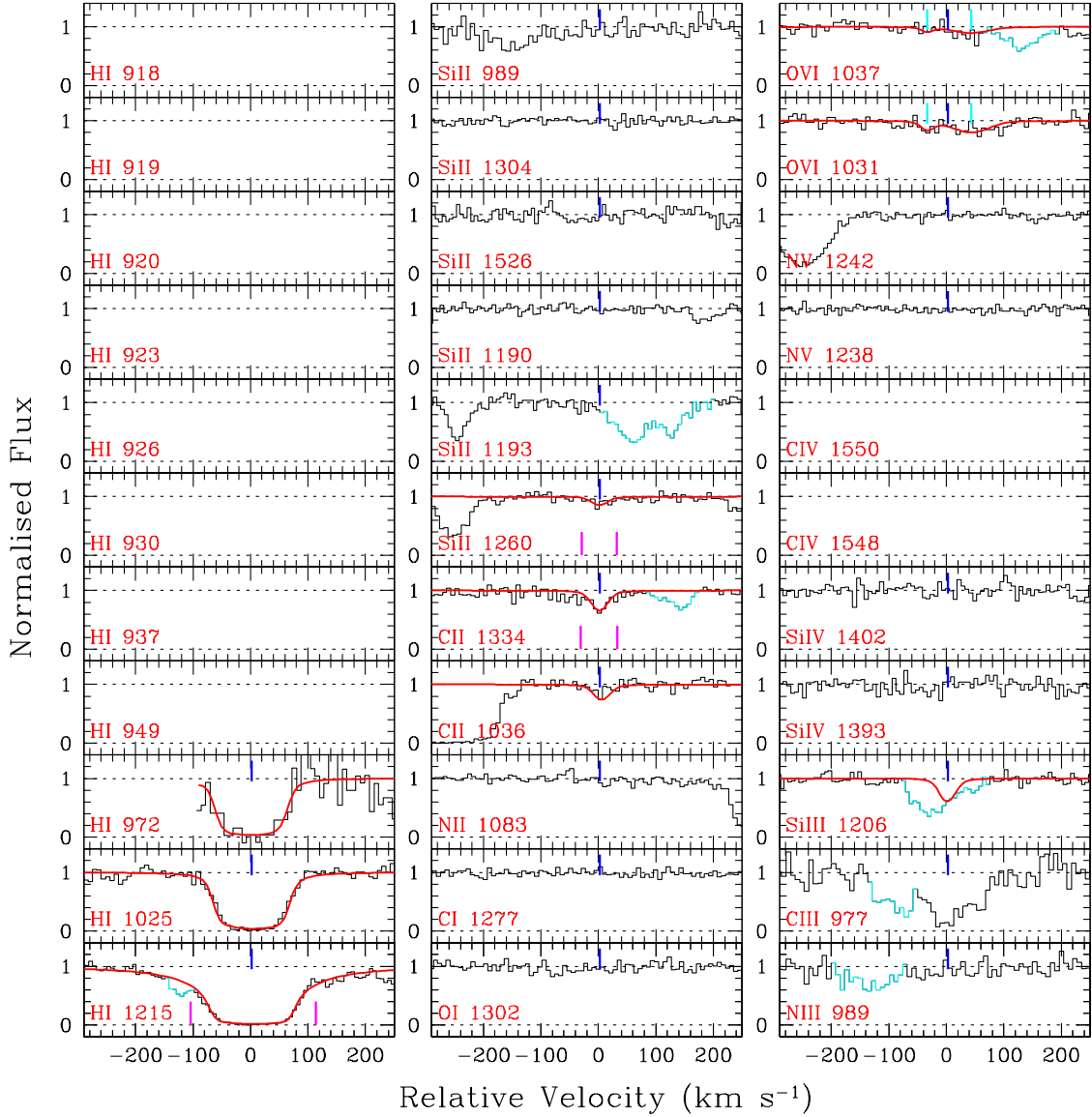
Figure C1. Velocity plot of the z_{abs} = 0.16512 system towards QSO PG 0003+158. Relevant parts of the COS spectrum covering various important transitions from the absorber are shown on a velocity scale. The zero velocity corresponds to the absorption redshift, mentioned on the top. The smooth red curves overplotted on top of the data (black histogram) are the best fitting Voigt profile models. No data are displayed when a line is not covered by the COS spectrum. The blue vertical ticks mark the line centroids of the model Voigt profiles and the pairs of vertical magenta lines in Lyα, Si IIλ1260, and C II λ1334 panels mark the region over which W_r of the corresponding line is measured. Unrelated absorption lines are shown in cyan. Very weak Si IIλ1260 and C IIλ1334 absorption lines are seen. The Si IIIλ1206 line is heavily blended with the Lyβ from the z_{abs} = 0.37037 system. The Lyγ and C IIIλ977 lines fall at the blue edge of the spectrum. Both the lines require a velocity shift of $\sim$ +30 km s^{-1} in order to be properly aligned with the other lines. The Lyβ, C IIλ1036, and O VI doublets, on the other hand, require a velocity shift of $\sim$ −10 km s^{-1}. The C II and Si II lines are fitted simultaneously keeping the z and Doppler-parameter (b) tied to each other. Since the Si III line is blended, we estimate the maximum allowed column density, using a z and b-parameter same as the C II/Si II line, that do not exceed the observed profile. The simultaneous and single component fit to the Lyman series lines explains the observed profiles adequately. We believe that the N(H I) of $10^{18.16\pm0.03}$ cm^{-2} is adequately constrained from the wing of the Lyα line along with the Lyβ and Lyγ profiles. We thus assign a quality factor of Q = 3 for this system.

Q0107−025A (z_{abs} = 0.22722)
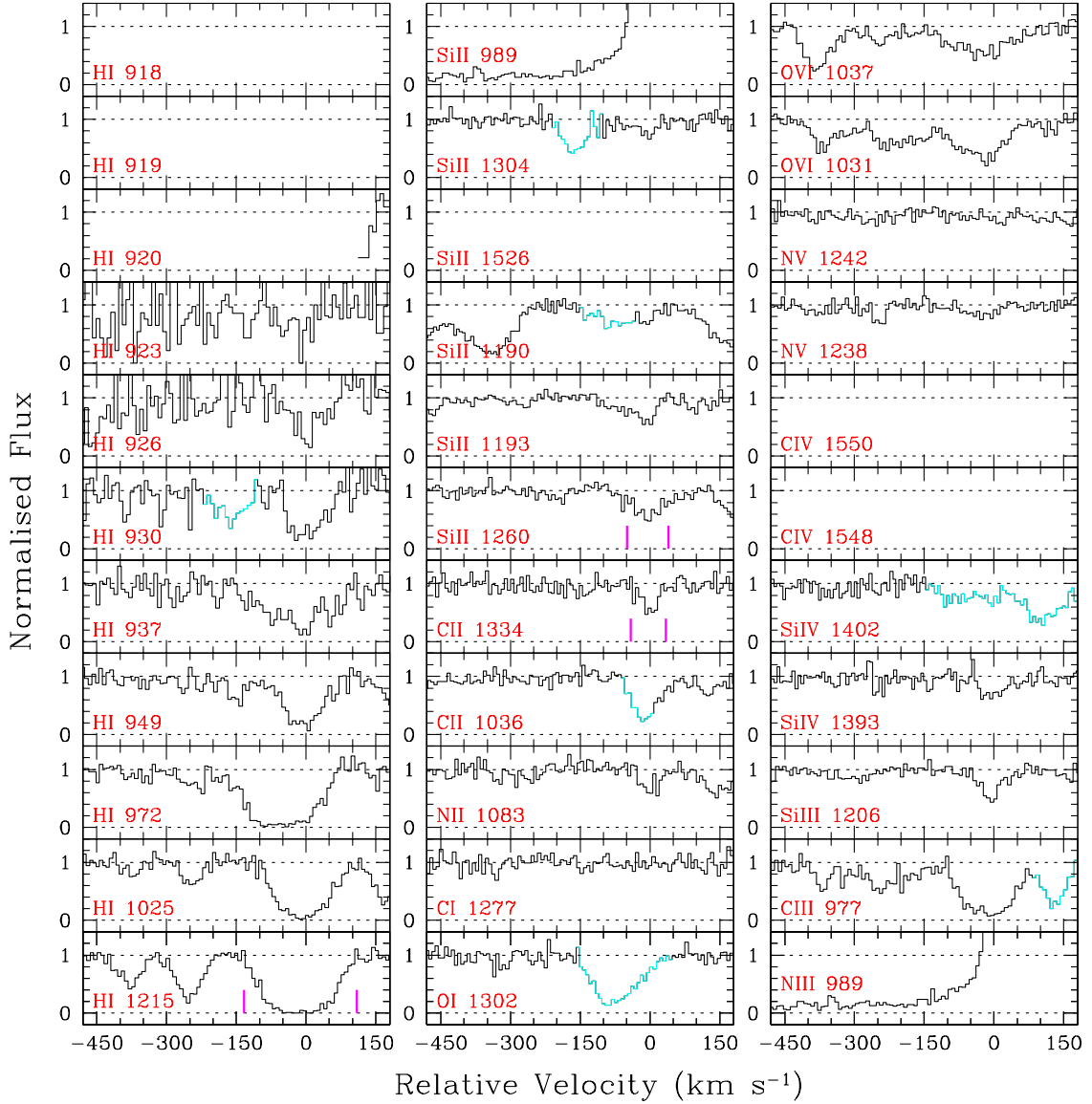
Figure C2. Similar to Fig. C1 but for the z_{abs} = 0.22722 system towards Q0107–025A. The Lyman series lines below H Iλ937 fall at the blue edge of the spectrum. These lines require 10–20 km s^{-1} velocity shifts in order to be properly aligned with other members of the Lyman series lines. The blue wing of the Lyγ line is blended with Galactic Si IIλ1193 absorption. The wavelength range corresponding to the Si IIλ989 and N IIIλ989 is affected by geo-coronal Lyα emission. A full-blown multiphase analysis of this absorber is presented in Muzahid (2014). Here we adopt the column densities of relevant ions from Table 1 of Muzahid (2014). Since several unsaturated higher order Lyman series lines are available for this system, the measured log N(H I) = 15.92 ± 0.08 has the highest quality factor of Q = 5.

HE0153−4520 ($z_{abs} = 0.22597$)
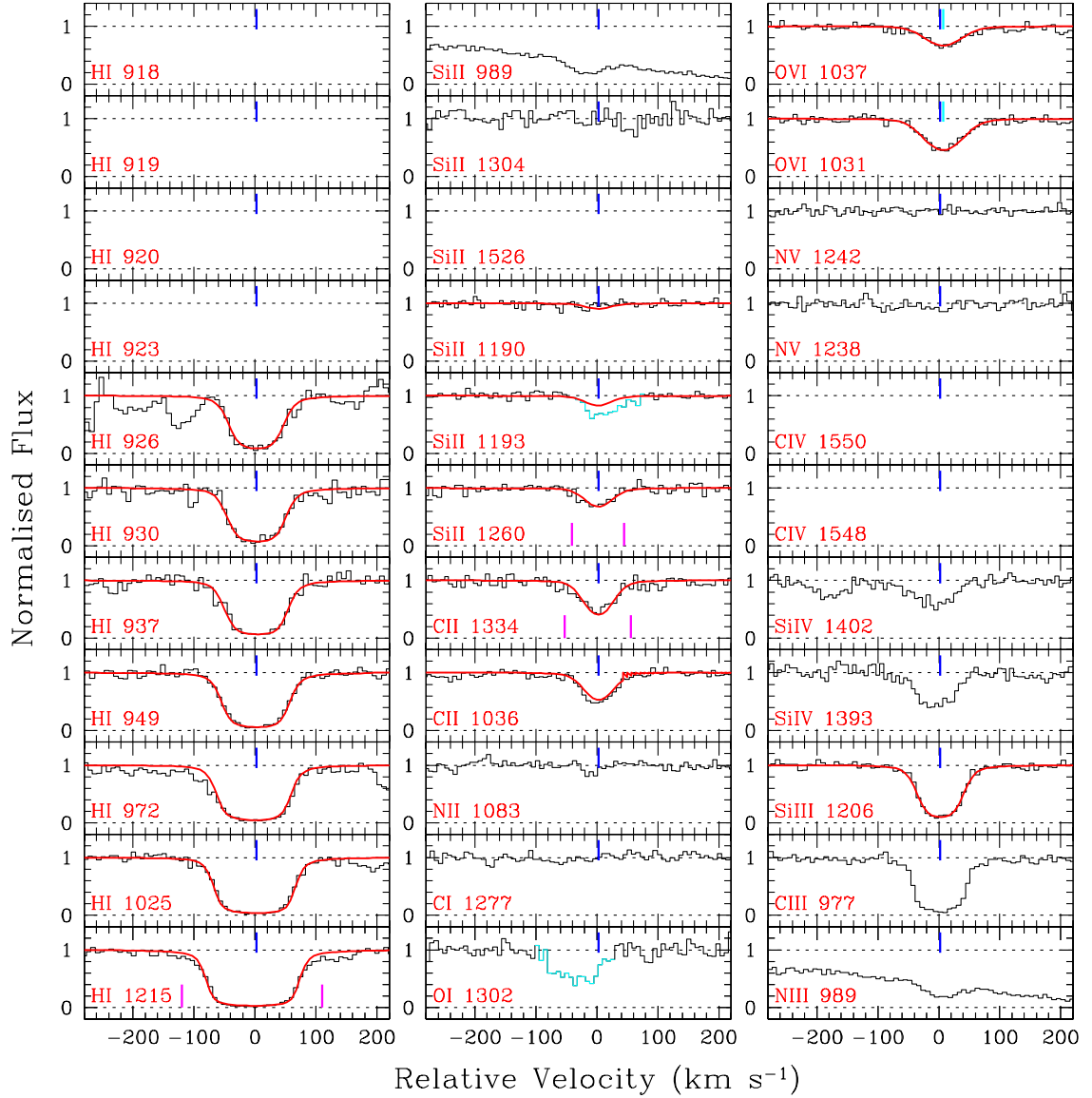
Figure C3. Similar to Fig. C1 but for the $z_{abs} = 0.22597$ system towards HE0153–4520. The wavelength range corresponding to the Si IIλ989 and N IIIλ989 is affected by Galactic Lyα absorption. The Si IIλ1193 line is blended with an unknown contaminant. The H Iλ1937, λ930, and λ926 lines fall at the extreme edge of the spectrum. These lines require ~7, ~15, and ~30 km s^{-1} velocity shifts, respectively, in order to be aligned with the other Lyman series lines. Voigt profile fitting of the metal lines (i.e., C IIλ1036, λ1334, Si IIλ1260, and Si IIIλ1206) is performed simultaneously by keeping the z and b-parameter of each line tied to the others. Note that the Si IIIλ1206 line is strongly saturated. We consider the measured N(Si III) to be a lower limit. A full-blown multiphase analysis of this absorber is presented in Savage et al. (2011). The column densities we obtained for the metal lines are consistent with the values reported in Savage et al. (2011). From the partial Lyman limit break seen in the FUSE spectrum they have constrained log N(H I) = $16.61^{+0.12}_{-0.17}$. Our single-component, simultaneous fit to the available Lyman series line provides a somewhat higher N(H I) value (i.e., log N(H I) = 16.83 ± 0.07) but the two values are consistent within 1.6σ. We thus assign a quality factor of $Q = 4$ for the N(H I) that we obtained.
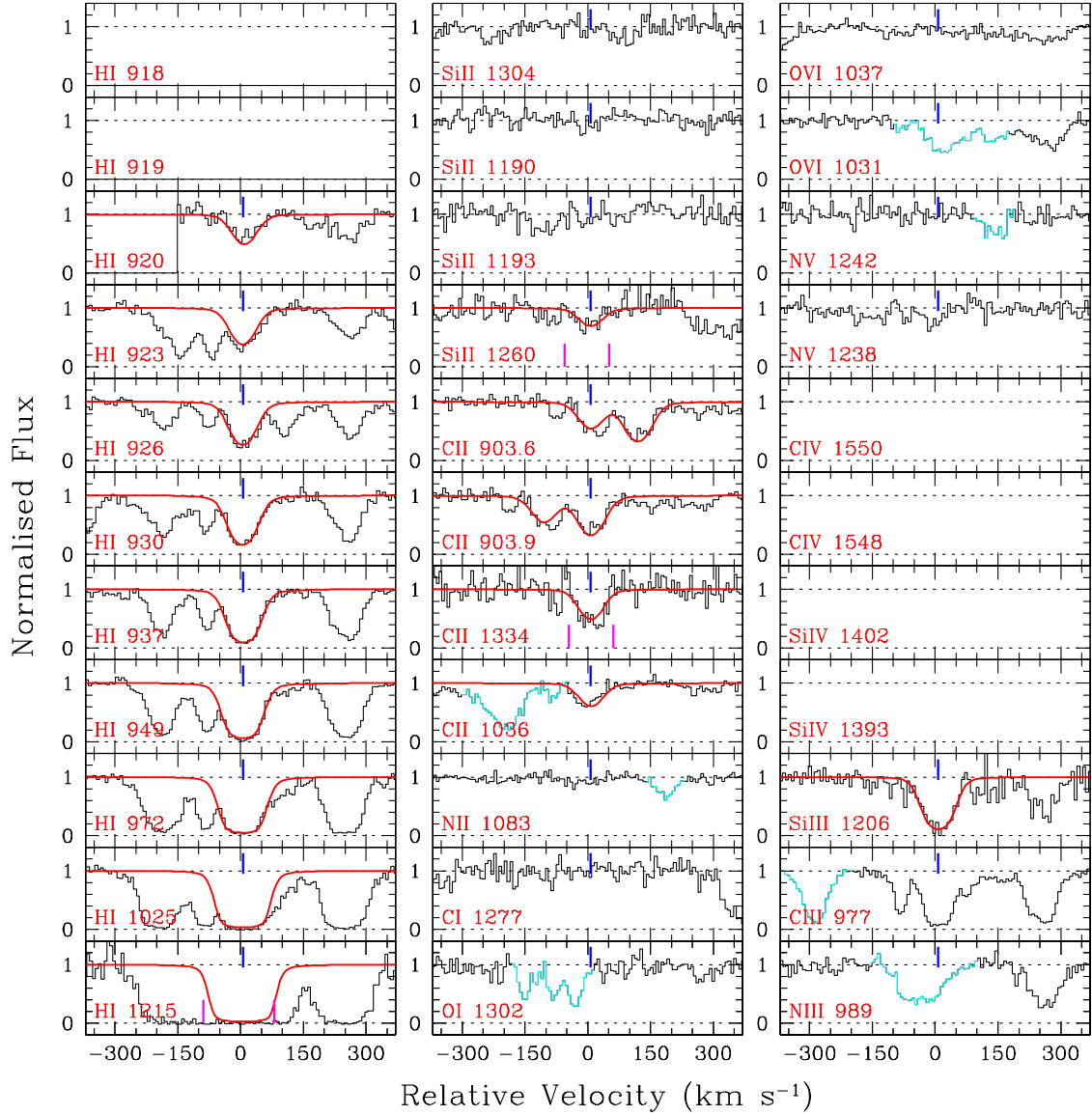
Figure C4. Similar to Fig. C1 but for the z_{abs} = 0.32338 system towards 3C57. The presence of several unsaturated Lyman series lines permits an accurate $N(\text{H I})$ measurement for the component that shows weak Si II and C II absorption. We assign a quality factor of Q = 5 for this system. The lack of any detectable absorption in the O VIλ1037 line near 0 km s^{-1} indicates that the absorption seen in the O VIλ1031 must be a blend. Voigt profile fitting for the metal lines is done simultaneously keeping the z and b-parameter tied. Note that the Si III line is strongly saturated and hence the measured $N(\text{Si III})$ is considered to be a conservative lower limit.

SDSSJ0212−0737 (z$_{abs}$ = 0.01603)
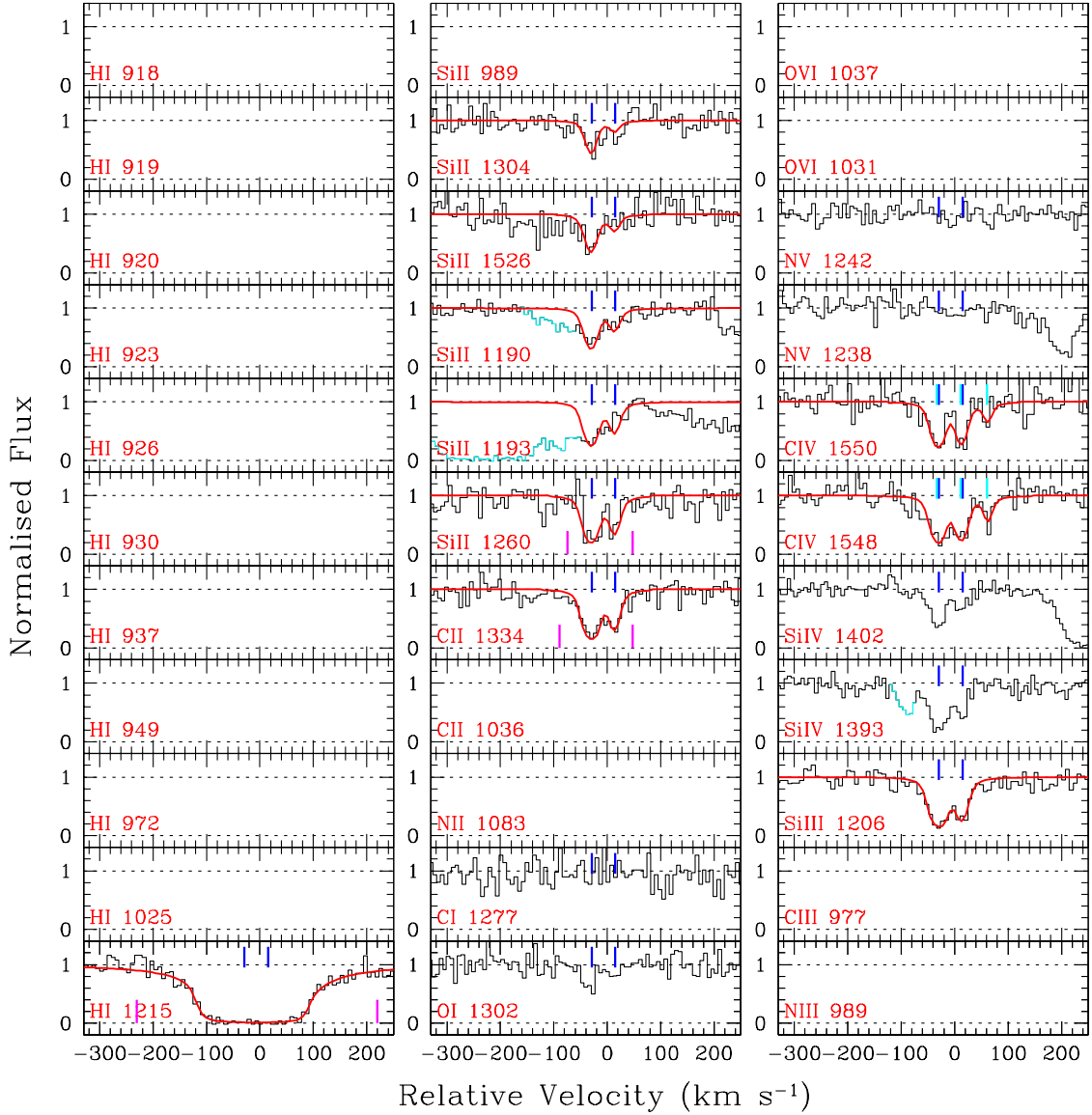
Figure C5. Similar to Fig. C1 but for the z_{abs} = 0.01603 system towards SDSSJ0212–0737. Besides low-ions, strong C IV and Si IV lines are detected. The Si IIλ1193 line is blended with the strong O VI λ1031 absorption at z_{abs} = 0.17403, intrinsic to the background QSO. We note that the Si IIλ1304 and O Iλ1302 lines require a velocity shift of ∼ −7 km s^{-1} with respect to the Si III. Additionally, the C IIλ1334 line is shifted by ∼ −3 km s^{-1}. All the metal lines are fitted simultaneously using two Voigt profile components. The component at ∼ −30 km s^{-1} is strongly saturated for both the C IIλ1334 and Si IIIλ1206 lines. In fact, the C IIλ1334 line is heavily saturated in both components. However, N(Si II) is adequately determined due to the presence of weaker Si II lines (e.g. λ1304). The Lyα profile and the presence of the O Iλ1302 line indicate a high N(H I). We believe that the estimated N(H I), using a two-component fit, is reasonably constrained from the wings of the Lyα absorption. We assign Q = 3 for this system.

SDSSJ0212−0737 (z$_{\mathrm{abs}}$ = 0.13422)
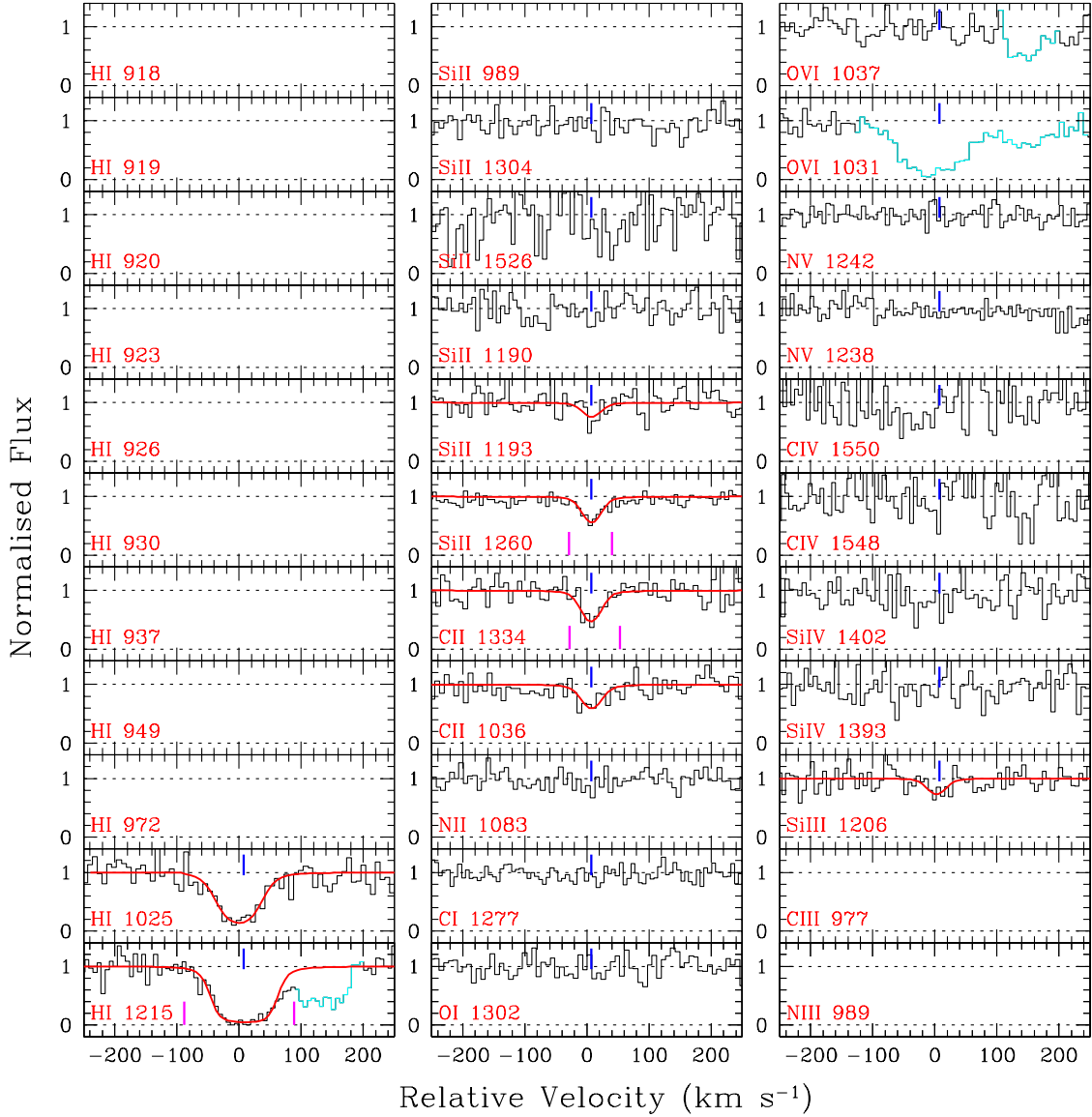
Figure C6. Similar to Fig. C1 but for the z_{abs} = 0.13422 system towards SDSSJ0212–0737. The absorption seen in the O VIλ1031 panel is actually Lyβ from the z_{abs} = 0.14107 system. We note that there is a velocity offset of ∼10 km s^{-1} between the Lyα and Lyβ absorption lines. The metal lines are fitted simultaneously keeping z and b-parameter tied. Similarly, we perform a simultaneous fit to the Lyα and Lyβ lines. Because the Lyβ absorption is only mildly saturated, with total log N(H I) = 14.95 ± 0.08, we assign a quality factor of Q = 3.

UKS−0242−724 (z$_{abs}$ = 0.06376)
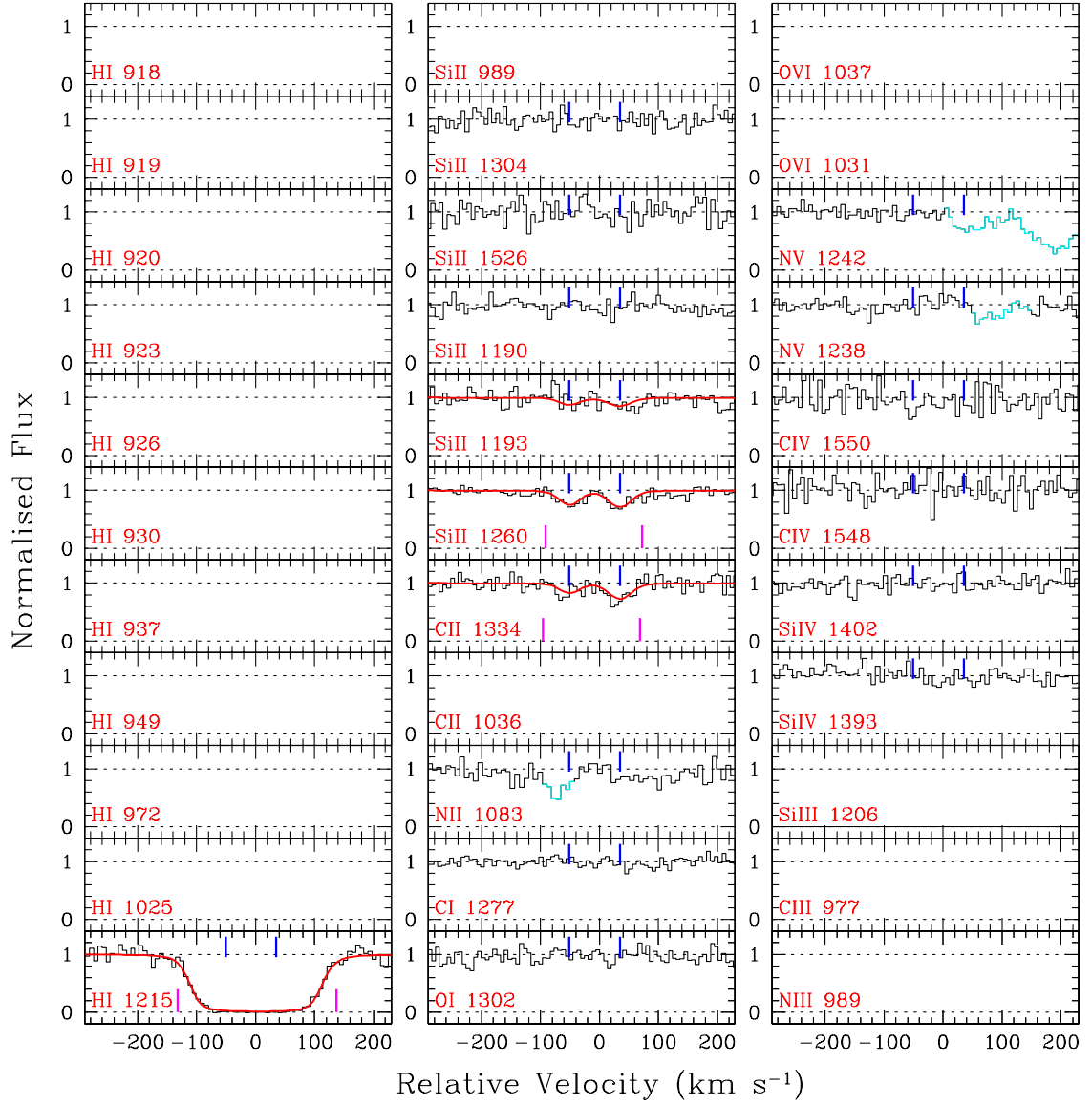
Figure C7. Similar to Fig. C1 but for the z_{abs} = 0.06376 system towards UKS–0242–724. The Si IIIλ1206 line falls on a spectral gap. Both the Si II and C II lines show a two-component structure. All three metal transitions are fitted simultaneously keeping the z and b-parameter tied to each other. Apart for Lyα, no other Lyman series lines are covered by the spectrum. We have used two components to fit the Lyα line using component redshifts obtained from the metal line fitting. Since the Lyα profile is heavily saturated and no higher order Lyman series lines are available, the estimated N(H I) is assigned the lowest quality factor of Q = 1.
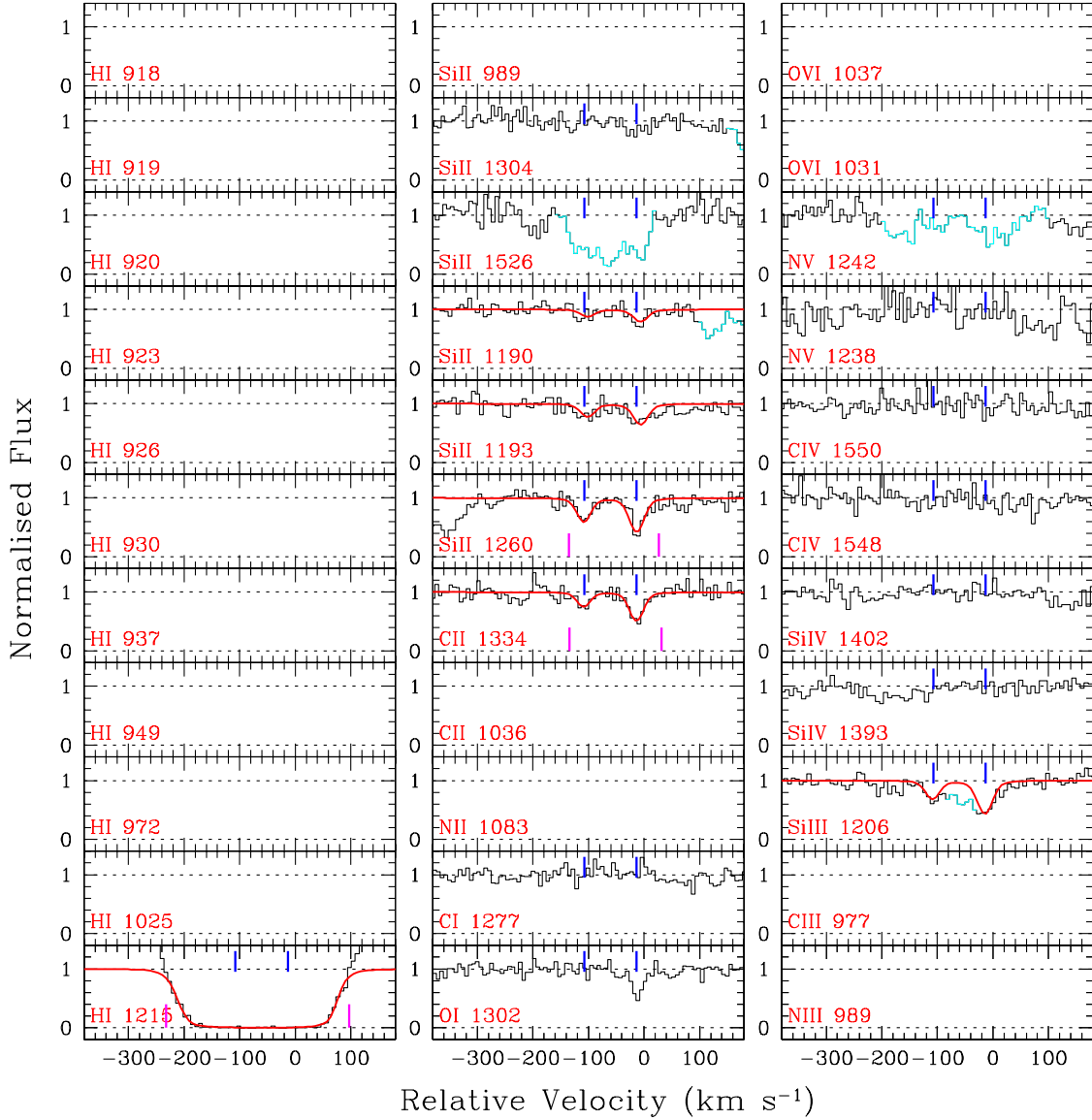
Figure C8. Similar to Fig. C1 but for the z_{abs} = 0.07256 system towards Q0349–146. The absorption seen in the Si IIλ1526 panel is the Si IIIλ1206 line of the z_{abs} = 0.35687 system. The Si IIλ1260 and C IIλ1334 lines are ∼ +8 km s^{-1} and ∼ −13 km s^{-1} offset with respect to the Si III line, respectively. The Si II and C II lines show two-component absorption kinematics. There is some absorption in-between the two components in the Si III line which is likely to be a blend. All the metal lines are fitted simultaneously. The presence of narrow O I line in the stronger component indicates a high N(H I) value. The Lyα line falls in between the geo-coronal O Iλ1302 and Si IIλ1304 emission lines. We used two Voigt profile components, as seen in the C II/Si II lines, with redshifts locked at the values obtained from the metal-line fitting, in order to fit the Lyα profile. This system is assigned a quality factor of Q = 1, since we could not determine the H I column density adequately.

PKS0405−123 (z_{abs} = 0.16710)
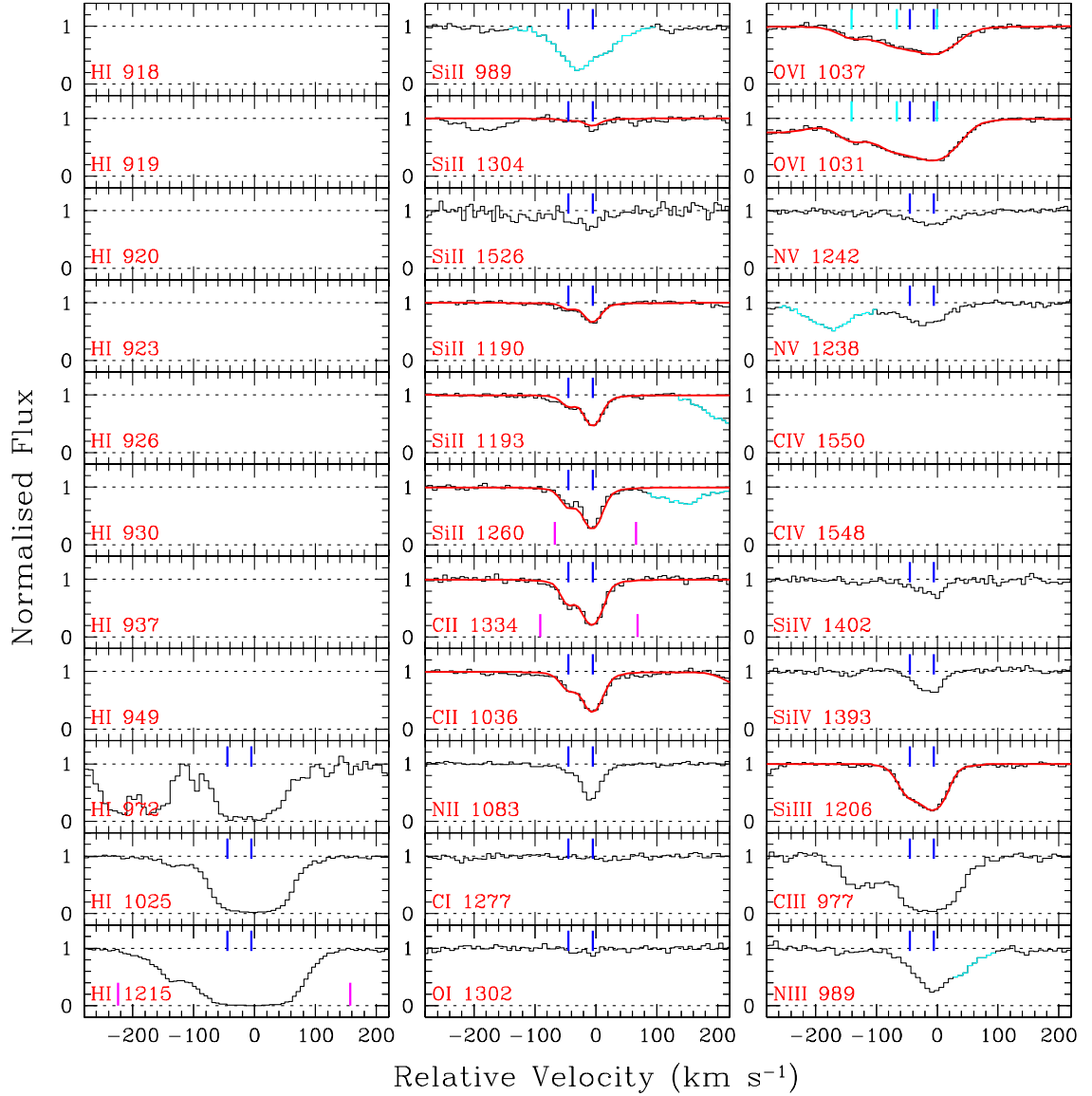
Figure C9. Similar to Fig. C1 but for the z_{abs} = 0.16710 system towards PKS0405–123. This system has been studied by several authors (e.g., Prochaska et al. 2004; Savage et al. 2010). A full-blown multiphase analysis of this absorber is presented in Savage et al. (2010). This particular spectrum has a serious wavelength-alignment problem. However, the high spectral S/N, and relatively simple and uncontaminated absorption kinematics make it easy to understand the nature of the wavelength calibration uncertainty. From the partial Lyman limit break observed in a FUSE spectrum, Prochaska et al. (2004) have constrained the total log $N(\text{H\,I})$ = 16.45 ± 0.05. Here we adopt this $N(\text{H\,I})$ value and do not attempt to estimate $N(\text{H\,I})$ from the COS spectrum since all three Lyman series lines are heavily saturated. We assign Q = 5 for this absorber. The different transitions of C\,II and Si\,II are fitted simultaneously keeping z and b-parameters tied. Si\,III, however, requires somewhat higher b-values. The total column densities we estimate for the metal lines are consistent with the measurements of Savage et al. (2010). Both the C\,II and Si\,III lines are strongly saturated. We consider both $N(\text{C\,II})$ and $N(\text{Si\,III})$ as conservative lower limits (see also Savage et al. 2010).

IRAS−F04250−5718 (z_{abs} = 0.00369)
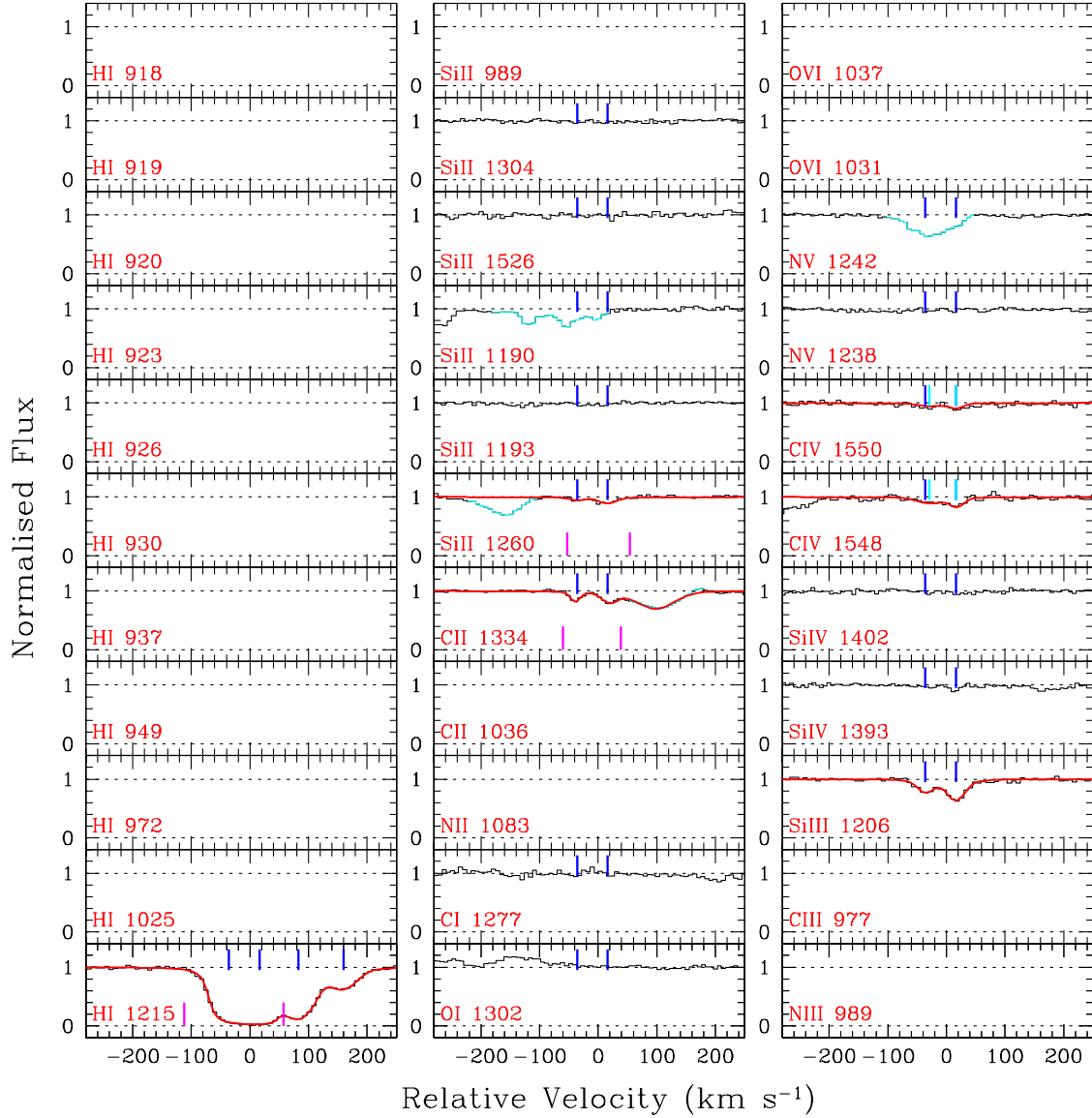
Figure C10. Similar to Fig. C1 but for the z_{abs} = 0.00369 system towards IRAS–F04250–5718. Very weak C IIλ1334, Si IIλ1260, Si III, and C IV doublet lines are detected. The red wing of the C IIλ1334 line is blended, possibly with the Lyα of an associated absorber at z_{abs} = 0.10220. Our fit to the C IIλ1334 line is corrected for the contaminating absorption. Except for the Lyα, no other Lyman series lines are covered. We use the line centroids and b-parameters of the Si III lines to fit the main Lyα absorption clump. In addition, two weak Lyα components are required to fit the red wing. Since the main Lyα absorption clump which is related to the metal lines is heavily saturated, we assign a quality factor of Q = 1 for this system.

FBQS0751+2919 (z_{abs} = 0.20399)
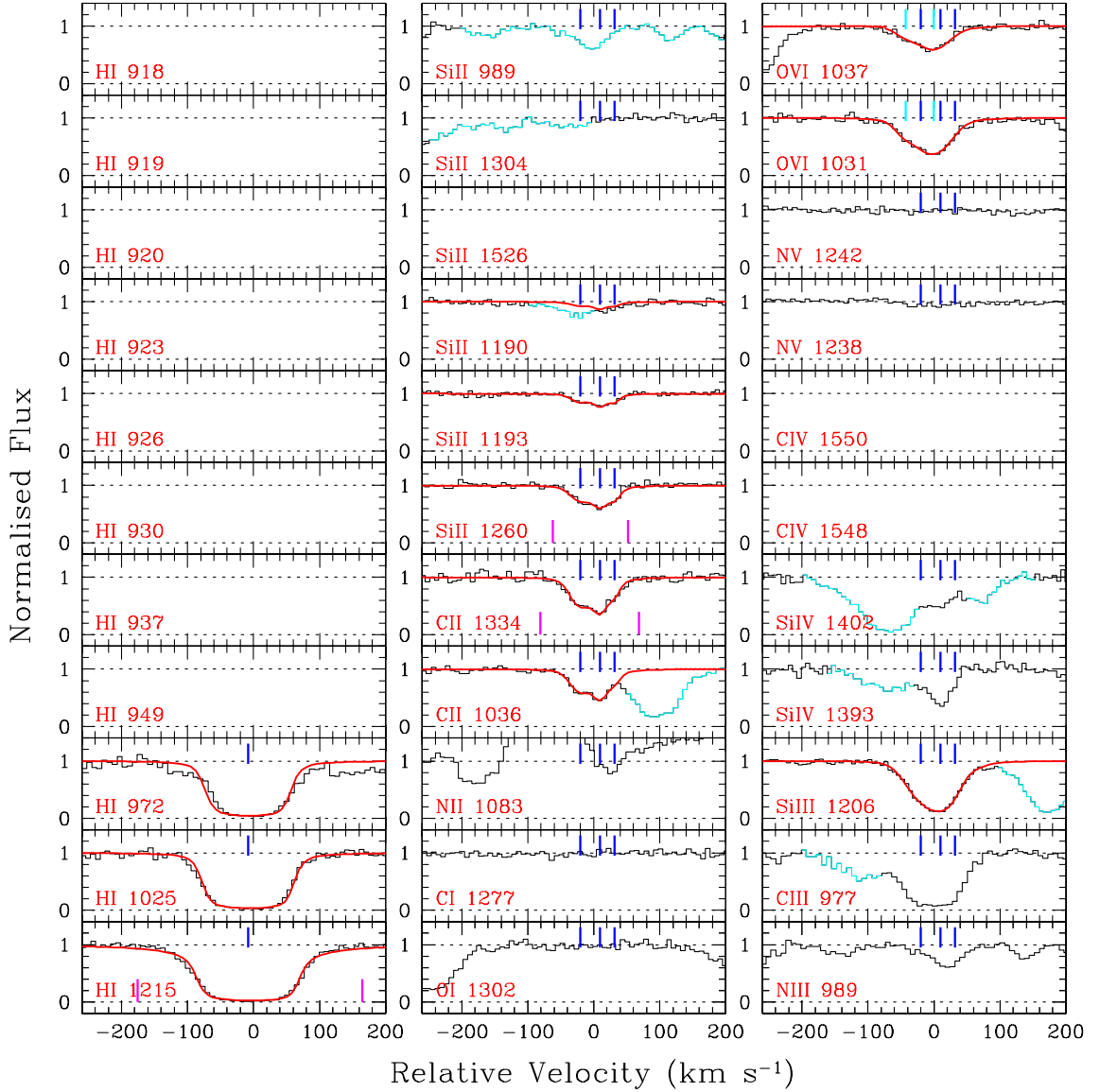
Figure C11. Similar to Fig. C1 but for the z_{abs} = 0.20399 system towards FBQS 0751+2919. Besides several weak low-ionization lines, strong O VI is detected, however, no N V is present. The N IIλ1083 absorption is severely affected by the geo-coronal O I emission. The blue wing of the C III line is possibly blended with the Lyβ of the z_{abs} = 0.14644 system. The strong absorption redward of the C IIλ1036 line is the Lyα from the z_{abs} = 0.02673 system. The blue wings of the Si IVλ1393 and λ1402 are blended by the higher order Lyman series lines (i.e., H Iλ917 and λ923, respectively) from the z_{abs} = 0.82912 system. We note that the lines with rest-frame wavelength $\lesssim$ 1050 Å require a velocity shift of $\sim$ −12 km s^{-1}. A minimum of three components is required to fit the C II and Si II lines simultaneously. The Si III line is strongly saturated and required larger component b-values compared to the singly ionized metal ions, suggesting an additional contribution from other gas phase(s). The measured N(Si III) should be treated as a lower limit. The available Lyman series lines are heavily saturated. We have performed both single-component and three-component fits to the Lyman series lines. A single-component fit gives log N(H I) = 17.77 ± 0.05 and b(H I) = 24 km s^{-1}. A three-component fit, on the other hand, gives an order of magnitude lower N(H I) of $10^{16.67\pm0.08}$ cm^{-2}. We adopted the single component fit results keeping in mind that the true N(H I) could only be less. We assign a quality factor of Q = 2 for the system.
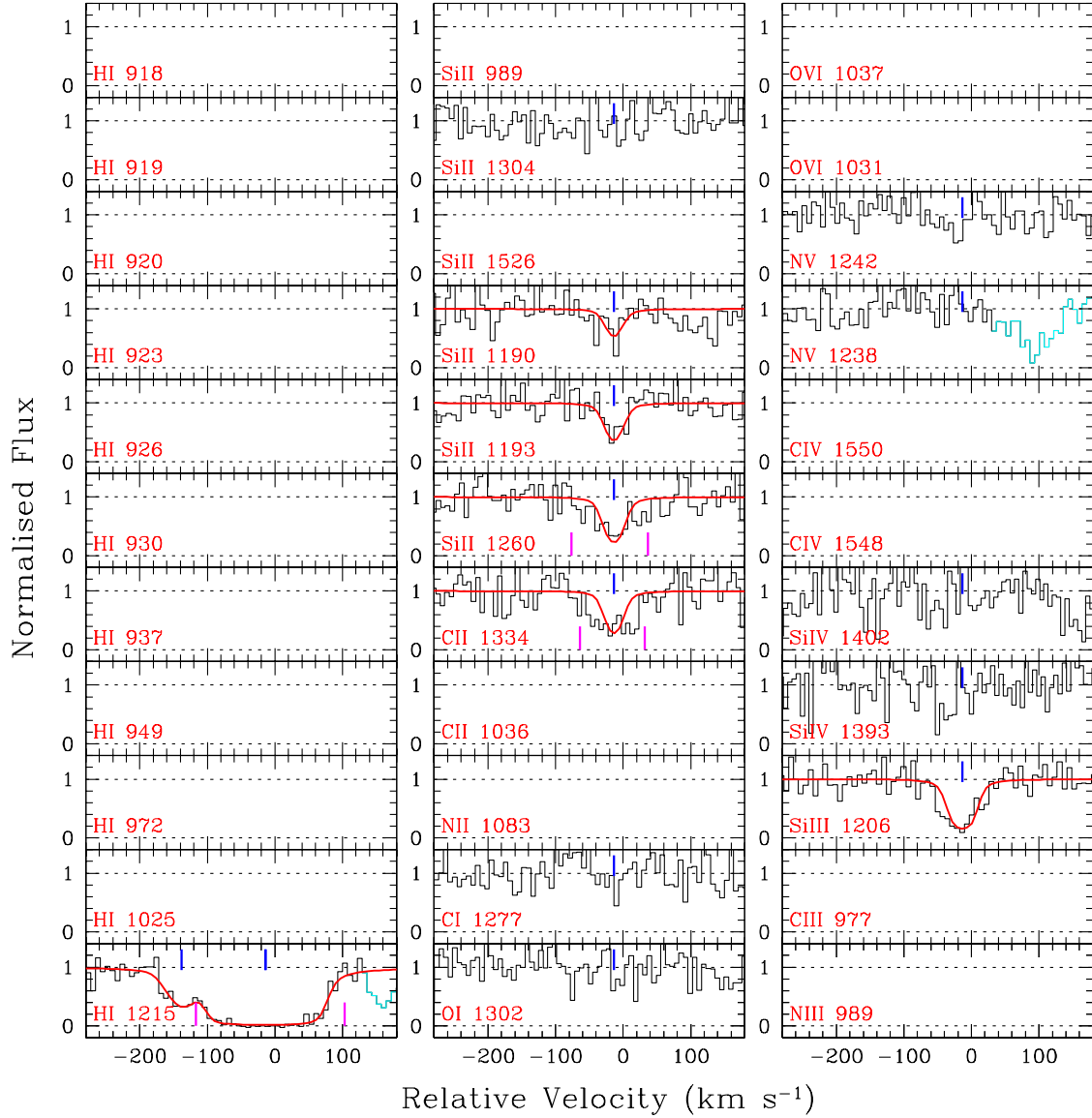
Figure C12. Similar to Fig. C1 but for the $z_{abs} = 0.02930$ system towards VV2006 J0808+0514. The C IV doublet is not covered since the spectrum is taken only with the G130M grating covering up to 1460 Å (observed). The spectrum looks noisy, however, consistent metal absorption lines are detected. First we fit the Si II lines ($\lambda 1190$, $\lambda 1193$, and $\lambda 1260$) simultaneously. We then use the best-fitting z and b-parameter to fit the C II$\lambda 1334$ and Si III$\lambda 1206$ lines. The C II line might have contributions from other unknown and unrelated absorption. We consider the measured N(C II) as a conservative upper limit. The Si III line is heavily saturated and hence N(Si III) should be treated as a lower limit. The N(H I) we estimate from the Lyα profile alone (log N(H I) = 17.57 ± 0.43) is highly uncertain. We assign a quality factor of $Q = 1$ for this system.

PG0832+251 (z_{abs} = 0.02811)
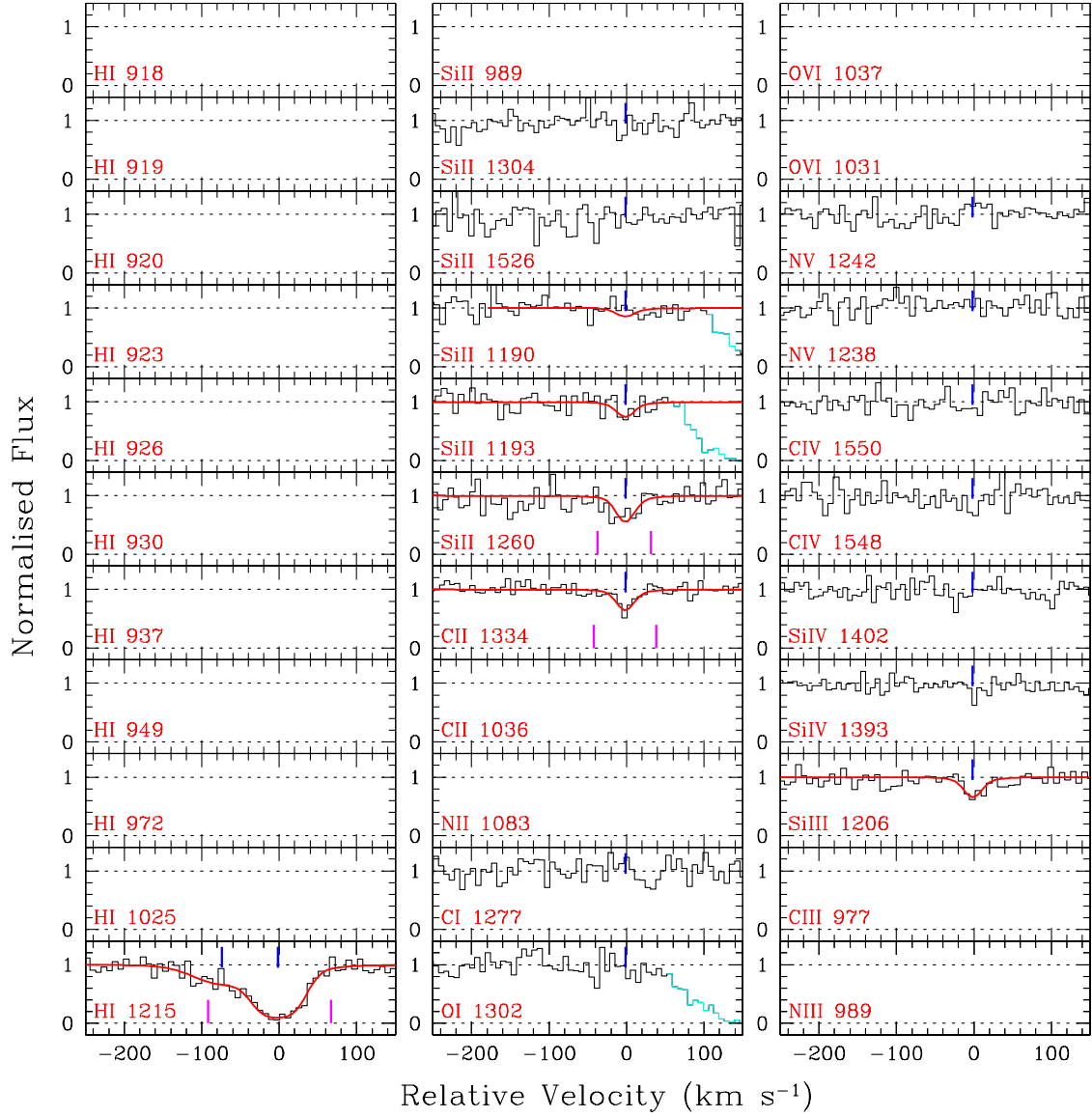
Figure C13. Similar to Fig. C1 but for the z_{abs} = 0.02811 system towards PG 0832+251. This is a very weak metal line absorber. Except for the C IIλ1334, which requires a velocity shift of ∼ +5 km s^{-1}, all other lines are well aligned. The Lyα line, which is only mildly saturated, exhibits an extra broad, weak component in the blue wing. Since the Lyα is not heavily saturated we assign a quality factor of Q = 2 for this system.

SDSSJ0929+4644 ($z_{abs} = 0.06498$)
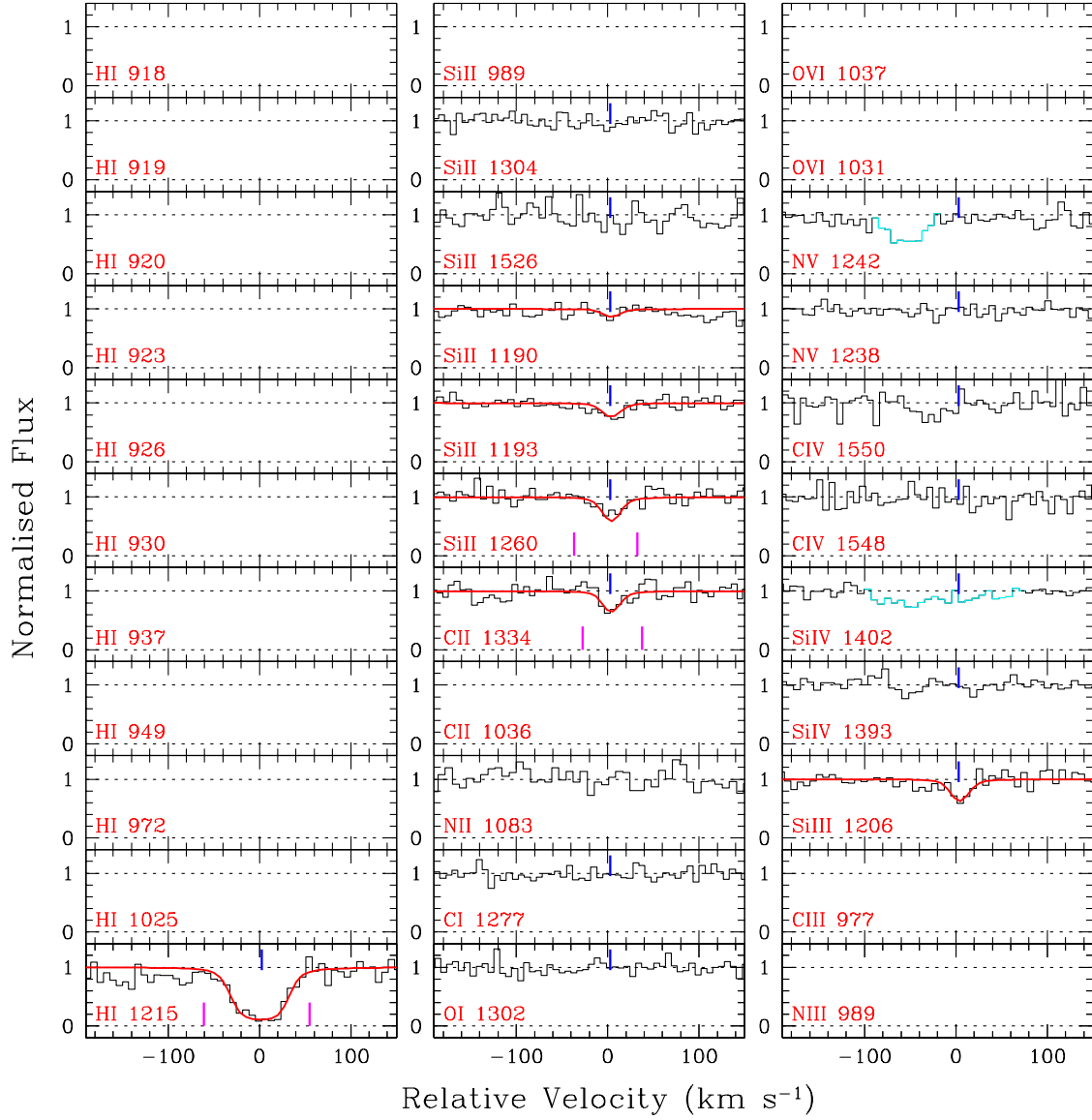
Figure C14. Similar to Fig. C1 but for the $z_{abs} = 0.06498$ system towards SDSS J0929+4644. Single-component, weak metal lines are fitted simultaneously keeping z and b-parameter tied. The Lyα is narrow, only mildly saturated, and off center by 8 km s^{-1} with respect to C II/Si II. We assign a quality factor of $Q = 2$ for this system.

PMNJ1103−2329 (z_{abs} = 0.08352)
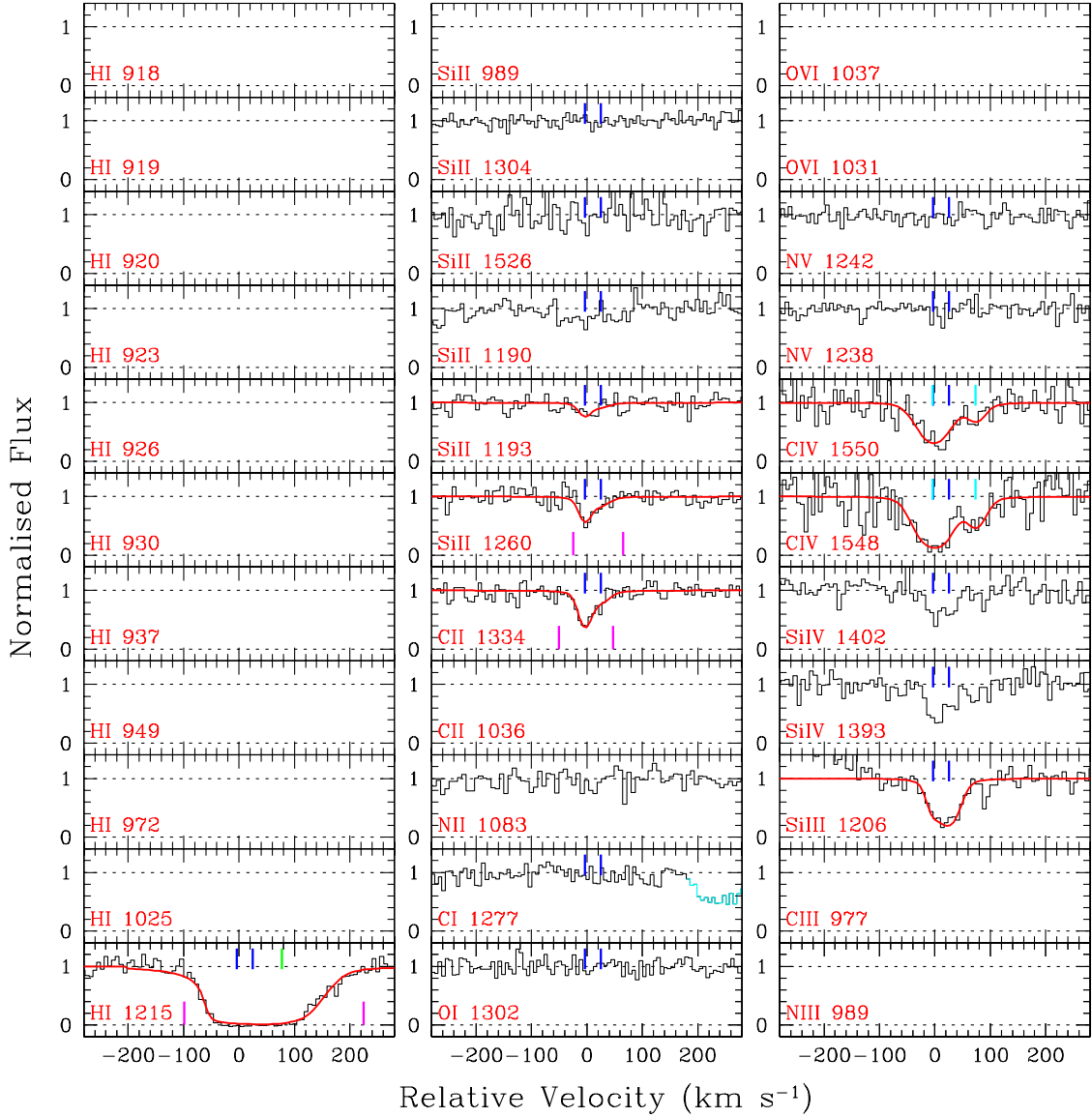
Figure C15. Similar to Fig. C1 but for the z_{abs} = 0.08352 system towards PMNJ1103–2329. Besides the low-ionization lines, multi-component, strong C IV and Si IV lines are present. The spectrum at ∼ −200 km s⁻¹ in the Si IIIλ1206 panel is affected by the geo-coronal O I+Si II emission lines. A minimum of two components is required to fit the metal lines simultaneously. The strength of the Si III absorption indicates that the line is heavily saturated. Therefore, the N(Si III) should treated as a lower limit. In addition to the two components seen in the low-ionization lines, the heavily saturated Lyα line requires a broad component at ∼ +80 km s⁻¹, corresponding to the C IV/Si IV component seen at the same velocity. Some amount of Si III may be present in this component as indicated by the spiky absorption we ignored in our analysis. However, the contribution of such a weak component to the total N(Si III) would be negligible. A free b-parameter fit to the Lyα profile was unstable. Thus, for estimating N(H I) associated with the two components that are aligned with the low-ions, we assumed b(H I) = 18.2, corresponding to T = 2 × 10⁴ K, for each component and determined the maximum N(H I) that can be accommodated within the observed profile, one-by-one. This allow us to put an upper limit on the N(H I). Due to the absence of the higher order Lyman series lines, we assign the lowest quality factor (i.e. Q = 1) for this system.

PG1116+215 ($z_{abs} = 0.13850$)
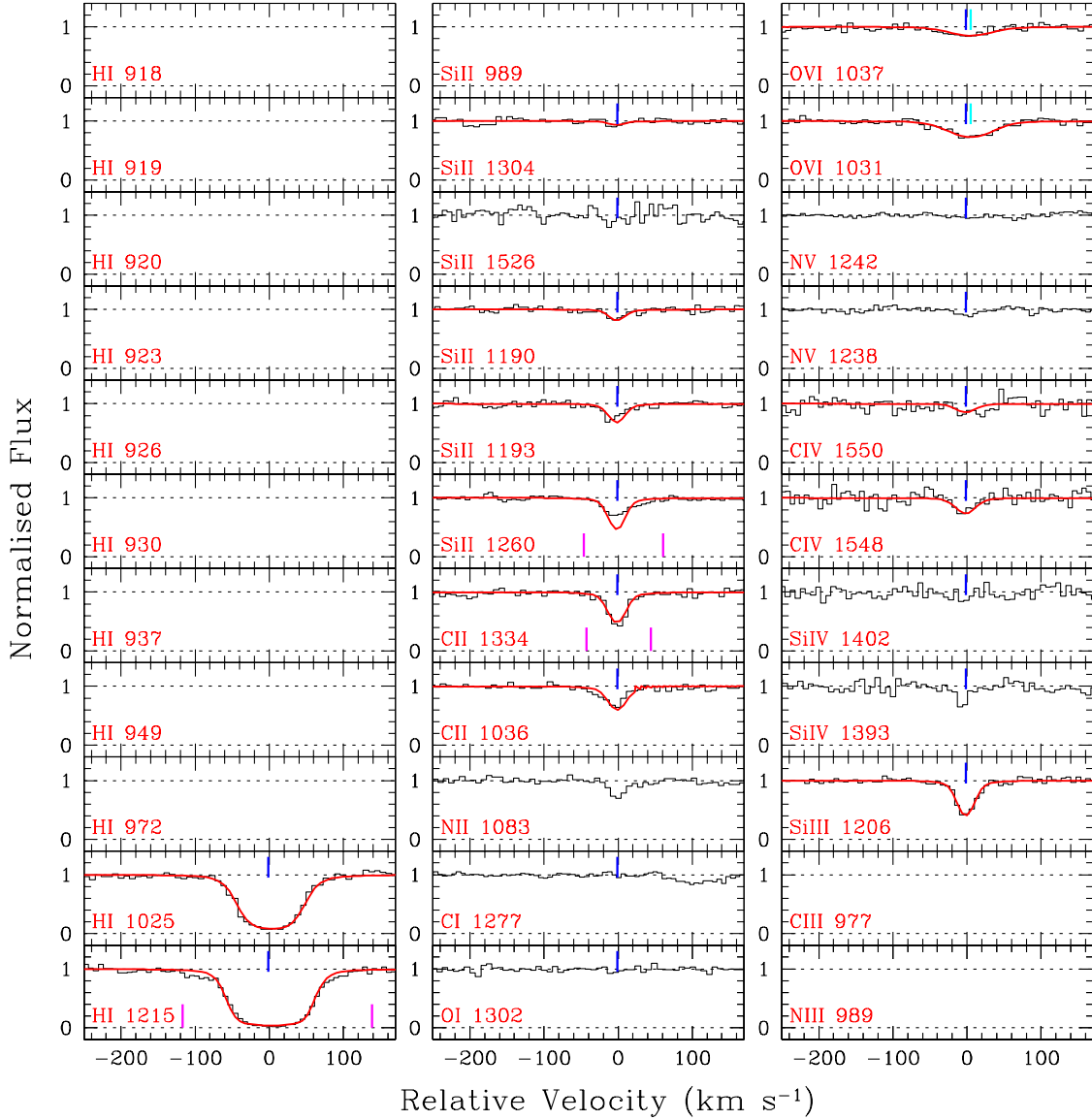
Figure C16. Similar to Fig. C1 but for the $z_{abs} = 0.13850$ system towards PG1116+215. This is a narrow, weak, single component system. We note that the lines with rest-frame wavelength < 1040 Å require a ~ −9 km s⁻¹ velocity shift. The metal lines are fitted simultaneously keeping the z and b-parameter tied. We notice that the Si IIλ1260 line falls on top of the QSO's Lyα+N V emission line. The apparent mismatch between the data and the model profile for the Si IIλ1260 line could be due to the fact that the absorber is not fully covering the broad emission line region of the background QSO (i.e., the partial coverage effect, see e.g., Muzahid et al. (2012)). This would indicate that the size of the absorber is very small. However, the possibility of unresolved saturation of the Si IIλ1260 line and/or uncertainty in the continuum placement also cannot be ruled out. The constraint on N(Si II) comes from the other weaker transitions, in particular, from the Si IIλ1190 line. FUSE and STIS observations of the full Lyman series lines (i.e., Lyα–H Iλ916) are presented by Sembach et al. (2004). Here we adopted their best-fitting COG value of log N(H I) = 16.20 ± 0.05 and assign the highest quality factor of $Q = 5$.

SDSSJ1122+5755 (z_{abs} = 0.05319)
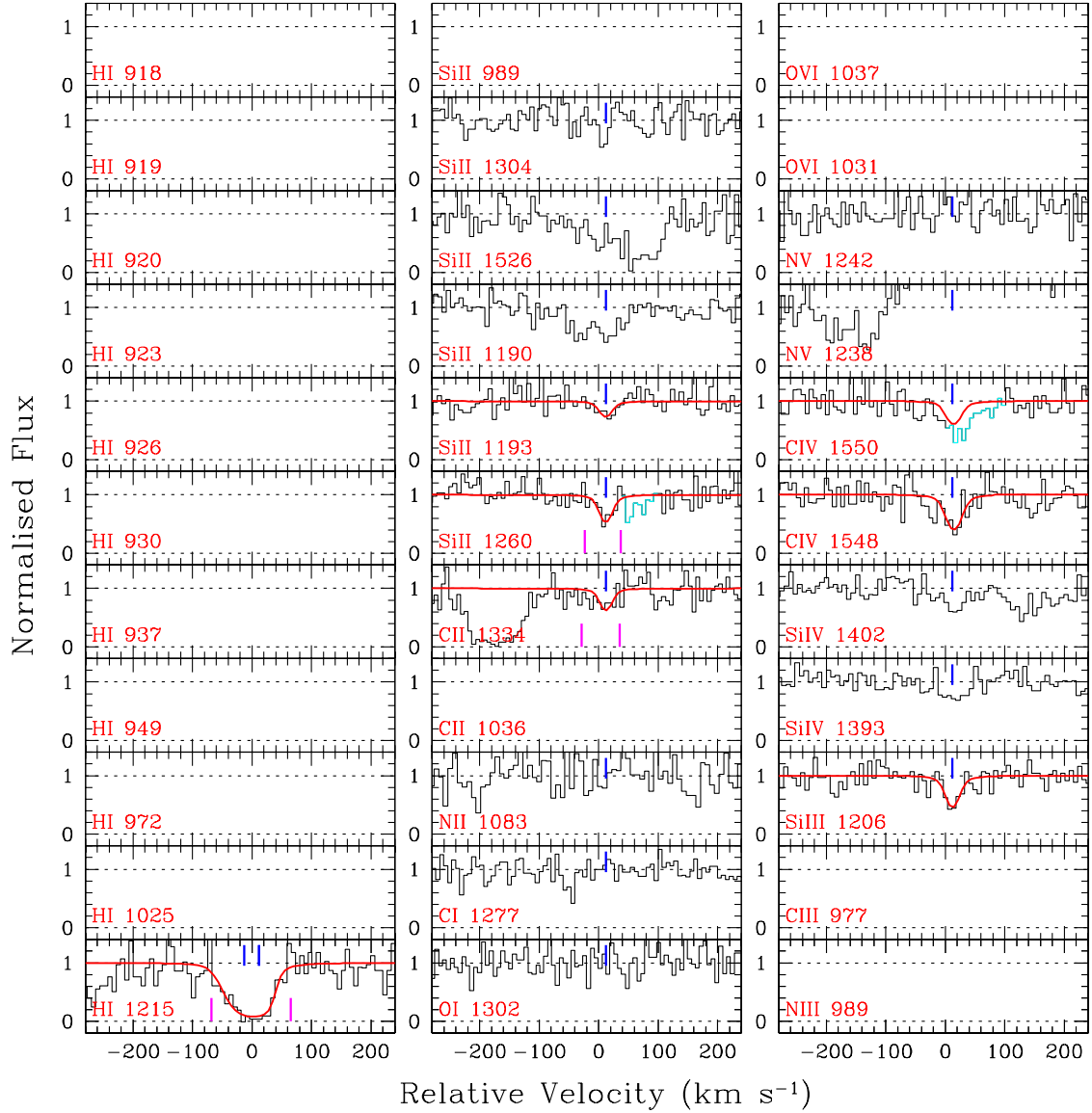
Figure C17. Similar to Fig. C1 but for the z_{abs} = 0.05319 system towards SDSSJ1122+5755. The absorption seen in the Si IIλ1190 and λ1526 panels actually arise from the Galactic S IIλ1253 and Fe IIλ1608 lines, respectively. The wavelength rage of N Vλ1238 is affected by the geo-coronal O I+Si II emission lines. The single component, weak metal lines are fitted simultaneously keeping z and b-parameters tied. Besides the weak low-ionization lines, strong C IV and weaker Si IV lines are detected. The Lyα absorption shows an asymmetric profile indicating the presence of more than one component. We used two components to fit the Lyα profile. VPFIT returns a large error ($\sim$ 1.5 dex) in N(H I). We assigned Q = 1 for this system.

PG1121+422 (z_{abs} = 0.19238)
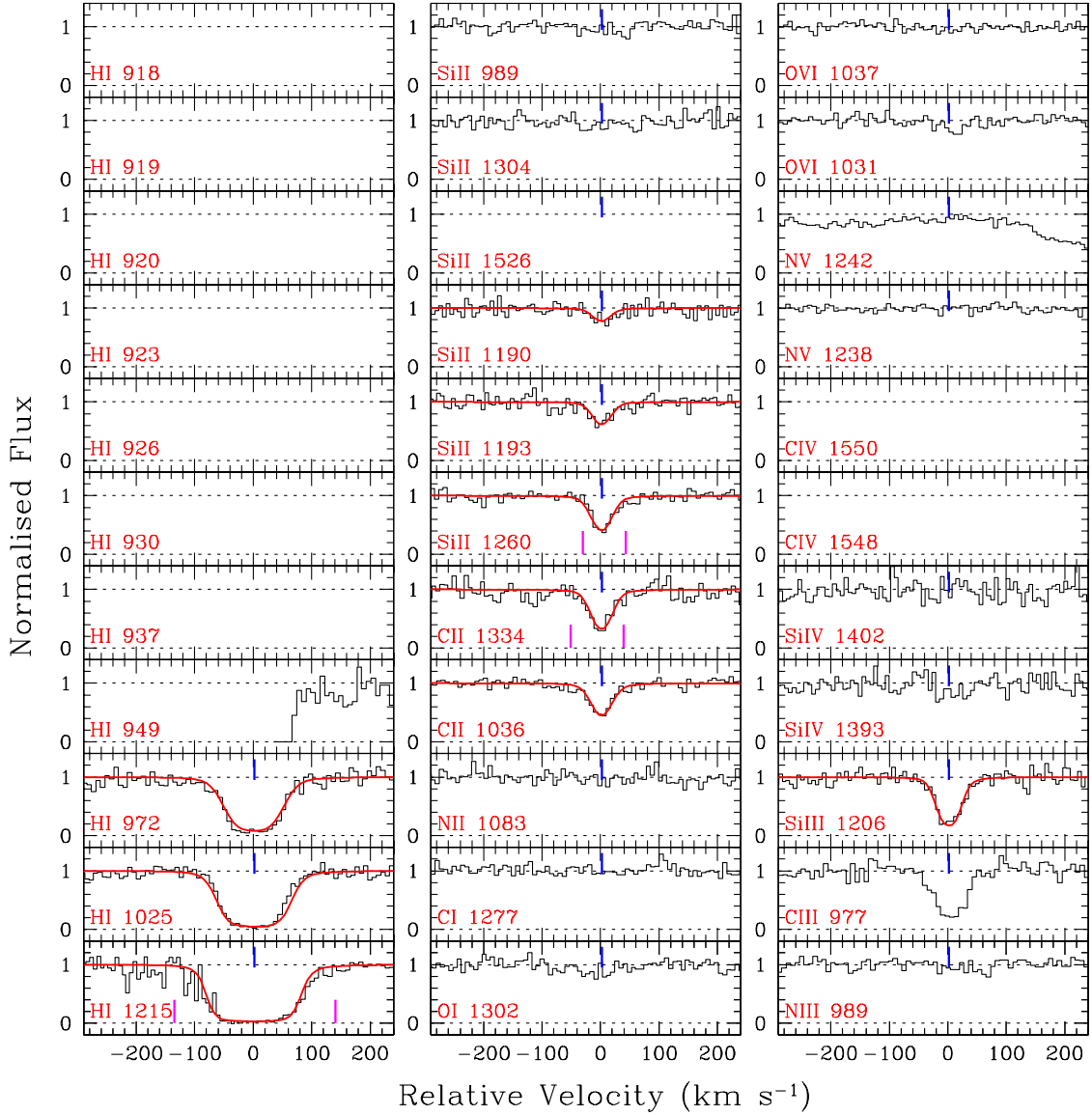
Figure C18. Similar to Fig. C1 but for the z_{abs} = 0.19238 system towards PG1121+422. Single-component metal lines are fitted simultaneously keeping z and b-parameters tied with each other. The Si III line is mildly saturated. We note that the C IIλ1036 and Lyβ lines require a velocity shift of ~ -11 km s^{-1} in order to be aligned with the other metal lines. All three Lyman series lines are heavily saturated. We obtained a solution with log N(H I) = 15.64 $\pm$ 0.05 and b(H I) = 37 $\pm$ 1 km s^{-1} using a simultaneous, single-component fit. Since all three Lyman series lines are saturated we assign Q = 2 for this system.
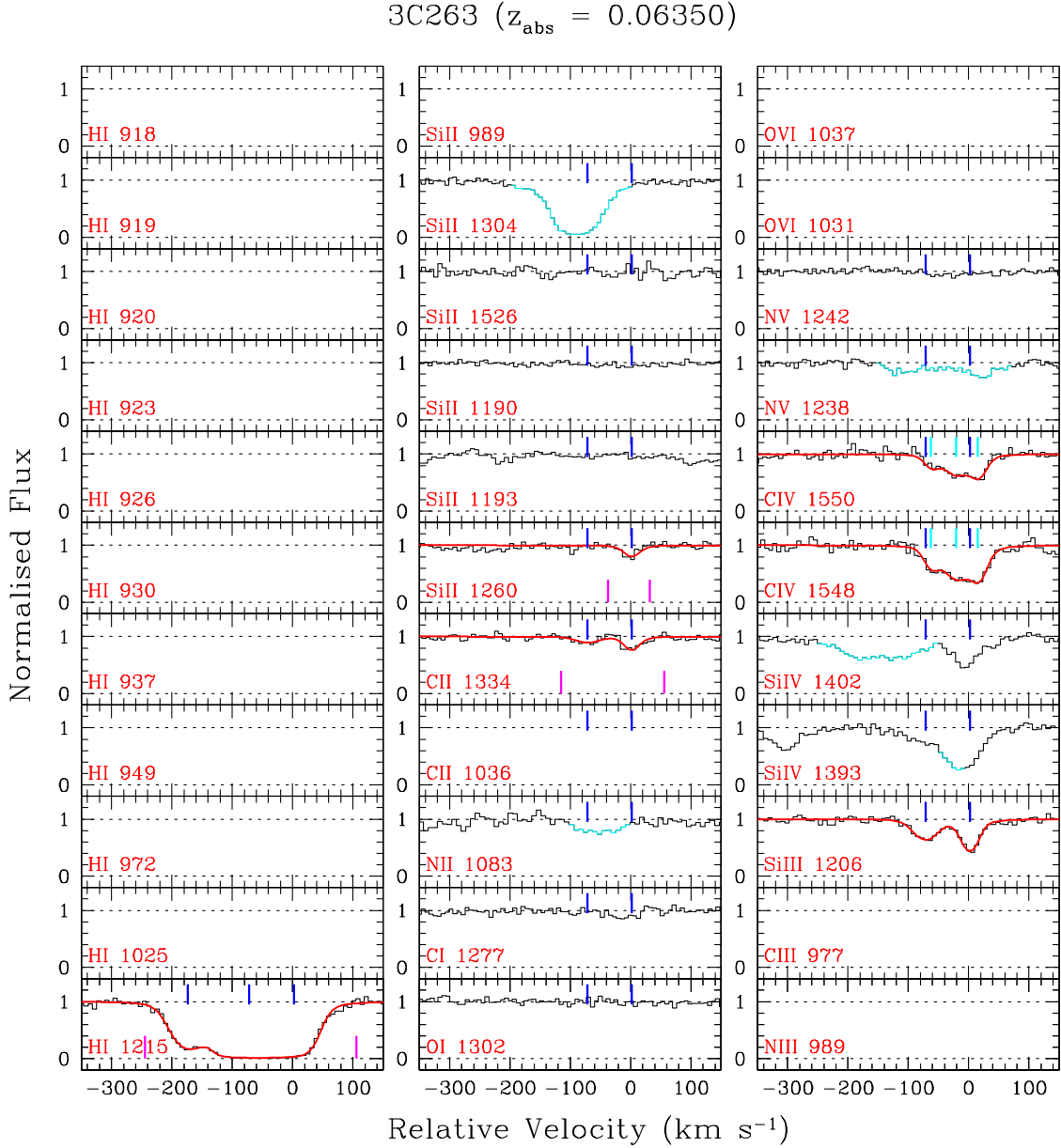
3C263 (z$_{abs}$ = 0.06350)

Figure C19. Similar to Fig. C1 but for the $z_{abs} = 0.06350$ system towards 3C263. Both the Si III and C IIλ1334 lines clearly show a two-component structure. The component at ~ -70 km s^{-1}, however, is not detected in the Si IIλ1260 line. Strong C IV$\lambda\lambda$1548, 1550 lines are present along with Si IV$\lambda\lambda$1393, 1402. The Si IVλ1393 line is possibly blended with the Lyα of the $z_{abs} = 0.21926$ system. The blue wing of the Si IVλ1402 line is blended with the Lyβ of the $z_{abs} = 0.45374$ system. Metal lines are fitted simultaneously. The Lyα line is fitted using three components, with two of them locked at the redshifts of the metal line components. An extra H I component is required to fit the weak absorption seen at ~ -180 km s^{-1}. However, we adopted the total log N(H I) = 15.40 ± 0.12 as measured by the Savage et al. (2012) from the unsaturated Lyγ profile using FUSE data. We thus assign a quality factor of $Q = 4$ for this system.

PG1202+281 (z_abs = 0.13988)
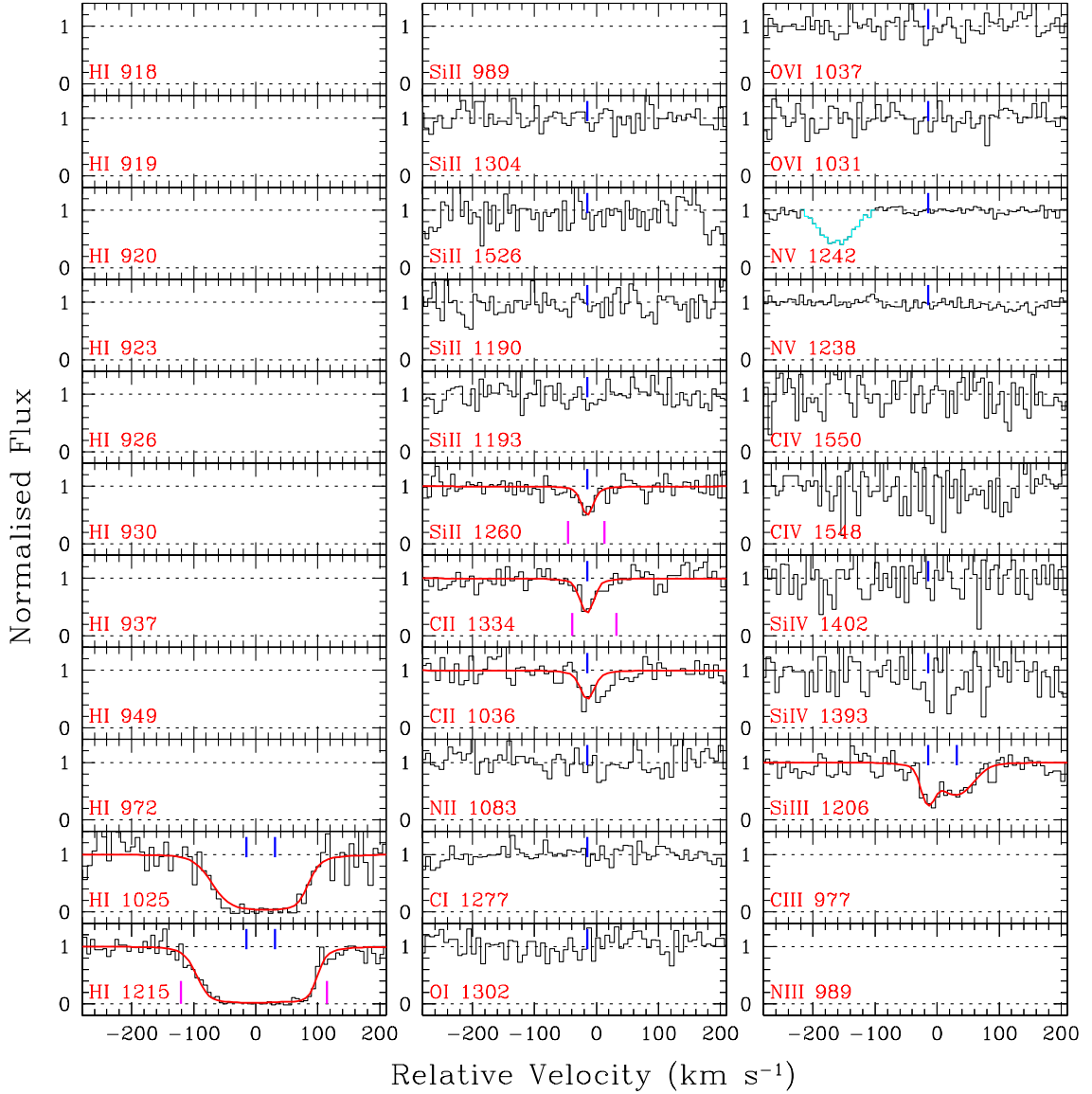
Figure C20. Similar to Fig. C1 but for the $z_{abs} = 0.13988$ system towards PG 1202+281. None of the high ionization lines are detected. The Si III line shows a two component absorption kinematics. The component at +40 km s^{-1} is not detected in the Si IIλ1260, C IIλ1334, and C II1036 lines. We note that the C IIλ1334 line is offset by ~ +10 km s^{-1} with respect to the Lyα/Si III line whereas the Lyβ and C II1036 lines are offset by ~ +20 km s^{-1}. The metal lines are fitted simultaneously keeping z and b tied for the component present in all of the transitions. A simultaneous fit is also performed for the Lyα and Lyβ lines using two Voigt profile components. The redshifts of the components are locked at the values obtained from the Si III fit. Since both the lines are heavily saturated we assign a quality factor of $Q = 1$.

PG1206+459 (z$_{abs}$ = 0.21439)
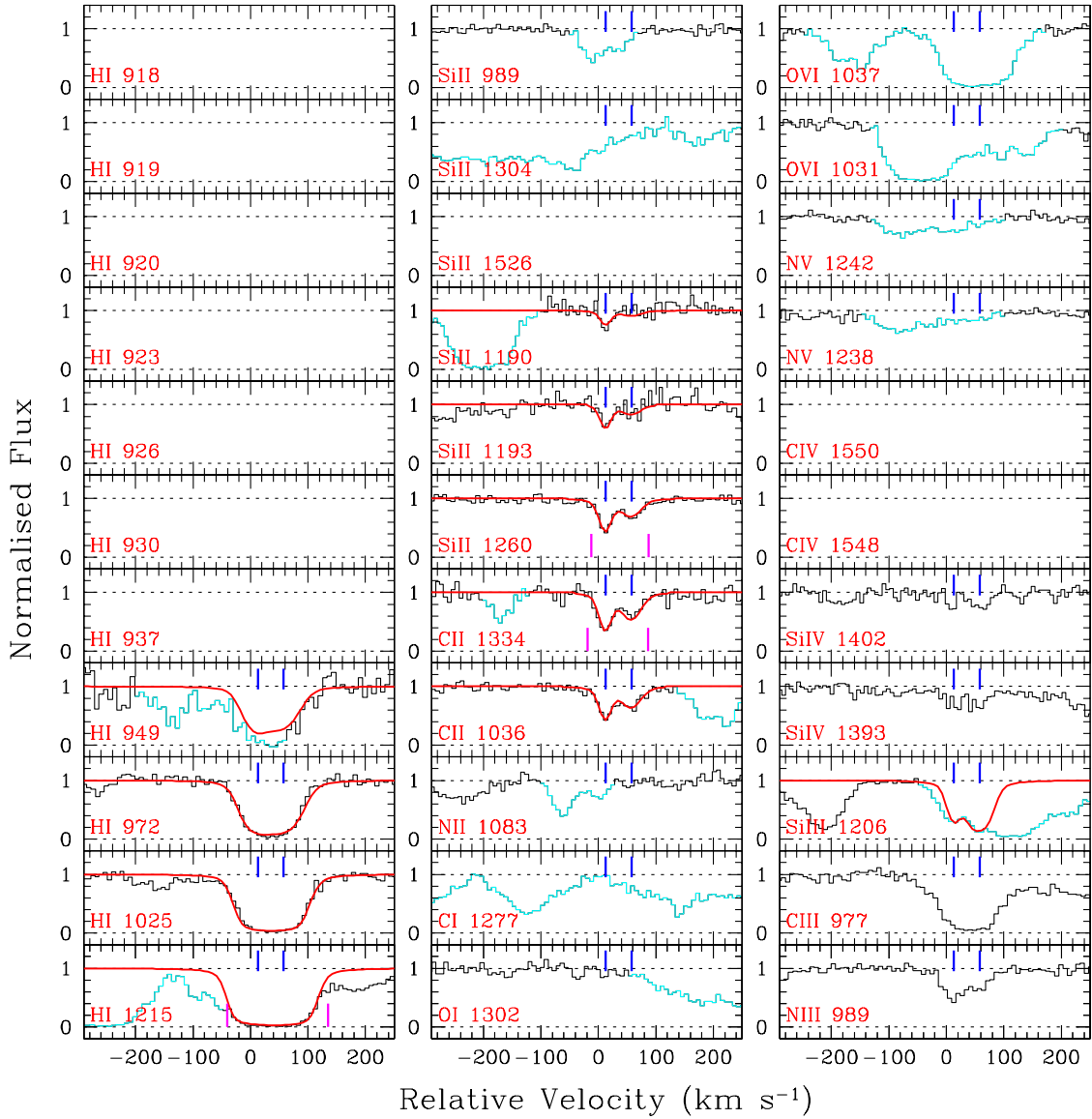
Figure C21. Similar to Fig. C1 but for the z_{abs} = 0.21439 system towards PG 1206+459. The narrow absorption seen in the blue wing of the Lyα line is the S IIλ765 from the z_{abs} = 0.9276 system. The absorption seen in the N Vλ1238 panel is actually the Ne VIII λ780 line from the same system (see Tripp et al. 2011, for details). The Si IIIλ1206 line is severely blended with the Lyα from the z_{abs} = 0.20575 system. The absorption in the Si IIλ1304 panel is actually the Ne VIII λ780 line from a known intrinsic absorber at z_{abs} 1.028 studied by Muzahid et al. (2013). The O VI λ1031 line is blended with the Galactic S IIλ1253 line and the Lyβ of the z_{abs} = 0.22156 system. The absorption in the O VI λ1037 panel is the Galactic Si II λ1260 line. So we could not confirm the presence/absence of O VI absorption in this system. This spectrum suffers from a complex velocity alignment problem. However the clean two component structure makes it possible to gauge the uncertainty. The two components seen in the weak metal lines are fitted simultaneously. Since the Si III line is heavily blended, we have estimated the maximum column density allowed by the profile by keeping the z and b-parameters locked at the values we obtained from the fitting of Si II and C II lines. The Lyman series lines are also fitted simultaneously using two components with the redshifts locked at the values we obtained for the metal lines. The H I λ949 line is partially blended by an unknown contaminant. However, we believe we have an adequate N(H I) measurement for this system with Q = 3.

SDSSJ1210+3157 (z_{abs} = 0.05974)
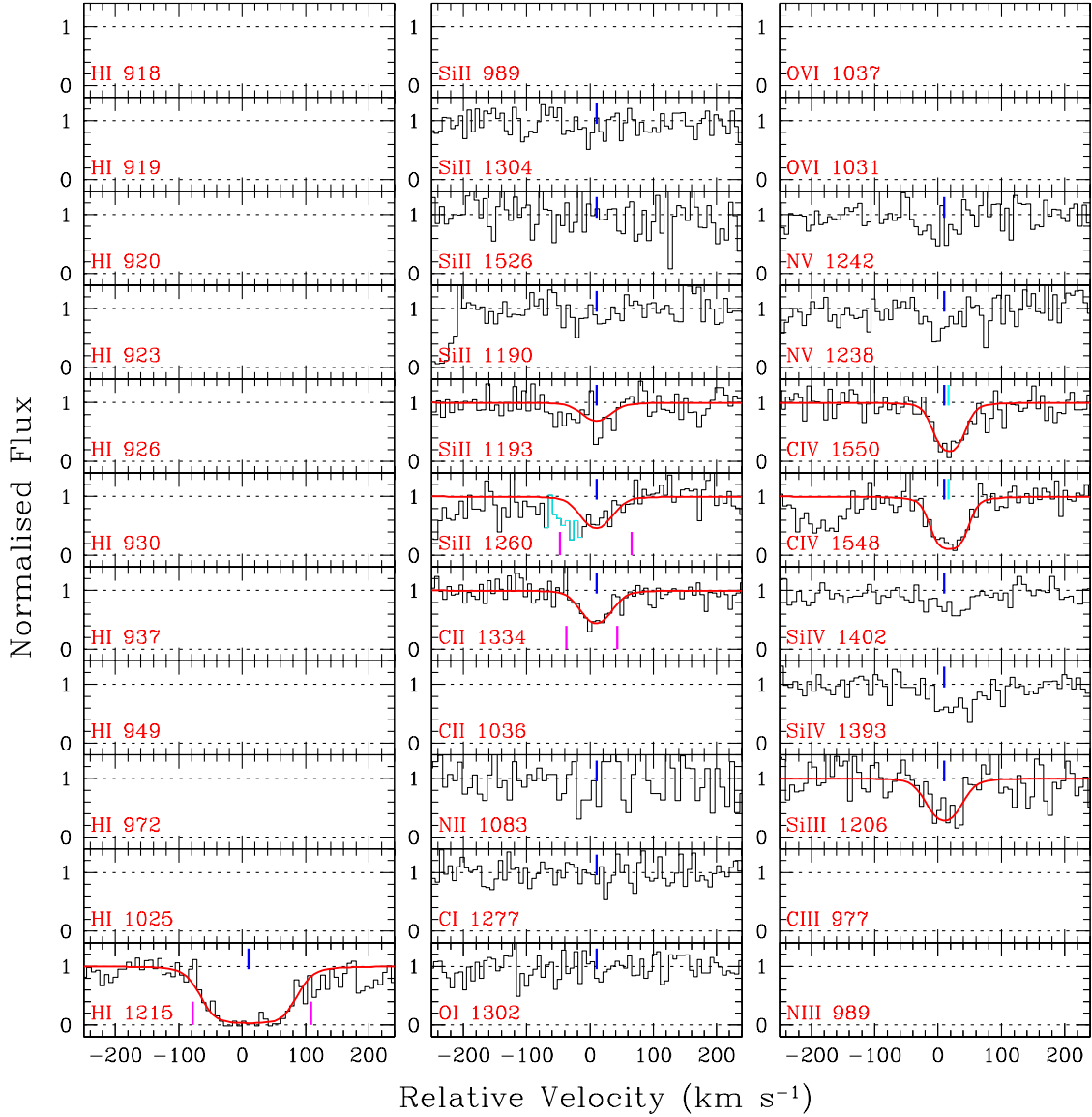
Figure C22. Similar to Fig. C1 but for the z_{abs} = 0.05974 system towards SDSSJ1210+3157. In addition to the low-ionization lines, strong C IV, and weaker Si IV, and N V lines are detected. The blue wing of the Si IIλ1260 is blended with the Galactic C II*λ1335 absorption. The equivalent width of the Si II line is, thus, calculated from the model profile. The spectrum is very noisy at the position of the Si IIλ1193 line. A single component, simultaneous fit is performed for all the metal line transitions. The Lyα line is fitted with a single component with redshift locked with the metal line component. Due to the lack of higher order unsaturated Lyman series lines, we assign Q = 1 for this system.

SDSSJ1210+3157 (z_{abs} = 0.14964)
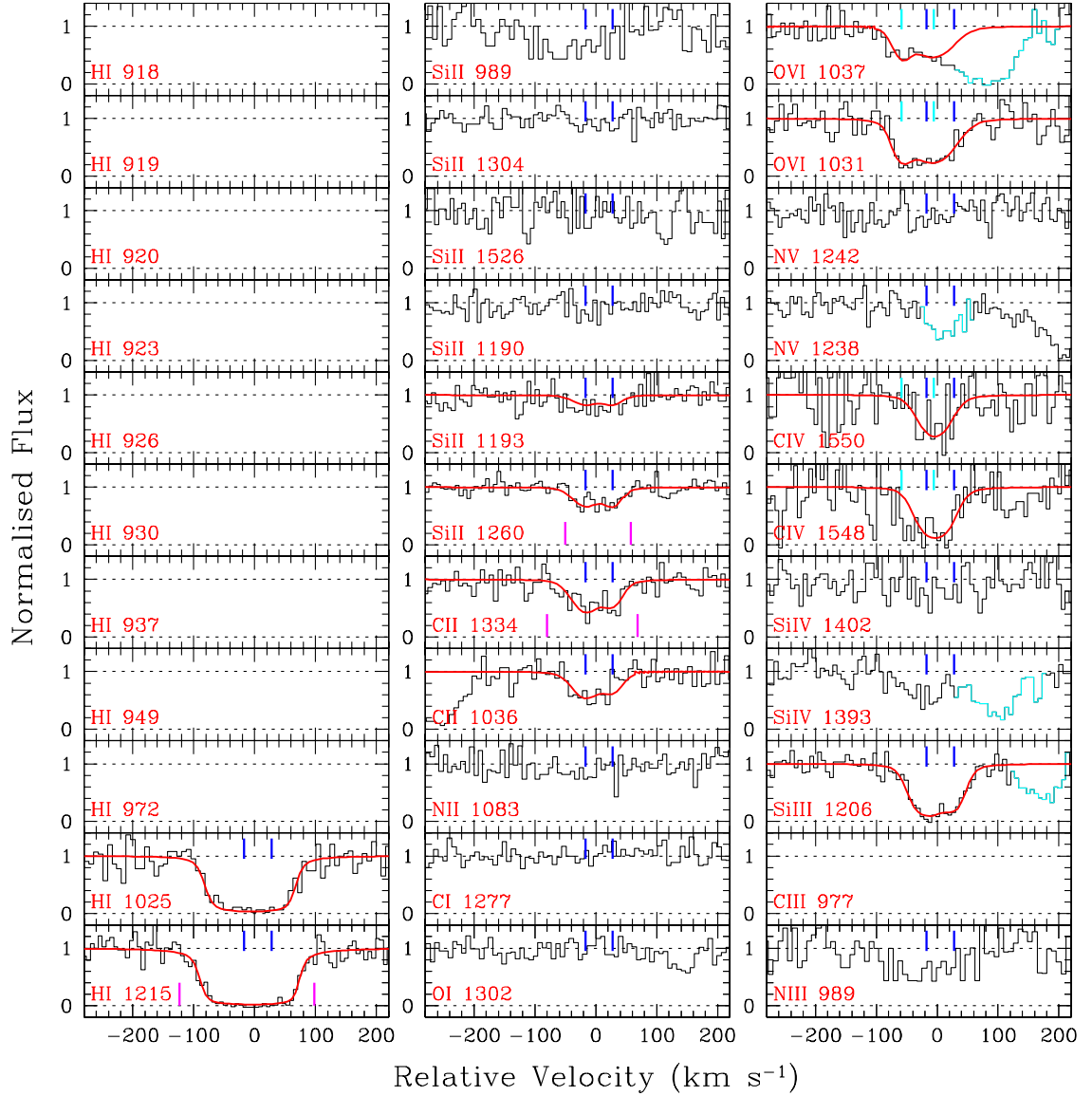
Figure C23. Similar to Fig. C1 but for the z_{abs} = 0.14964 system towards SDSSJ1210+3157. Besides several low-ionization lines, strong O VI and C IV lines are detected. The O VIλ1037 line is blended with the Galactic Si IIλ1193 absorption. The absorption seen in the N Vλ1238 panel is the Lyβ from the z_{abs} = 0.38854 associated system. Though the spectrum is noisy, a two component absorption kinematics is clearly seen in the Si III line. Note that the Si III line is strongly saturated. Thus the N(Si III) we obtained from VPFIT should be considered as lower limit. Both the Lyman series lines are heavily saturated. We performed simultaneous fitting keeping both z and b-parameters locked at the values we obtained from metal line fit. Since both the lines are heavily saturated we assign Q = 1 for this system.
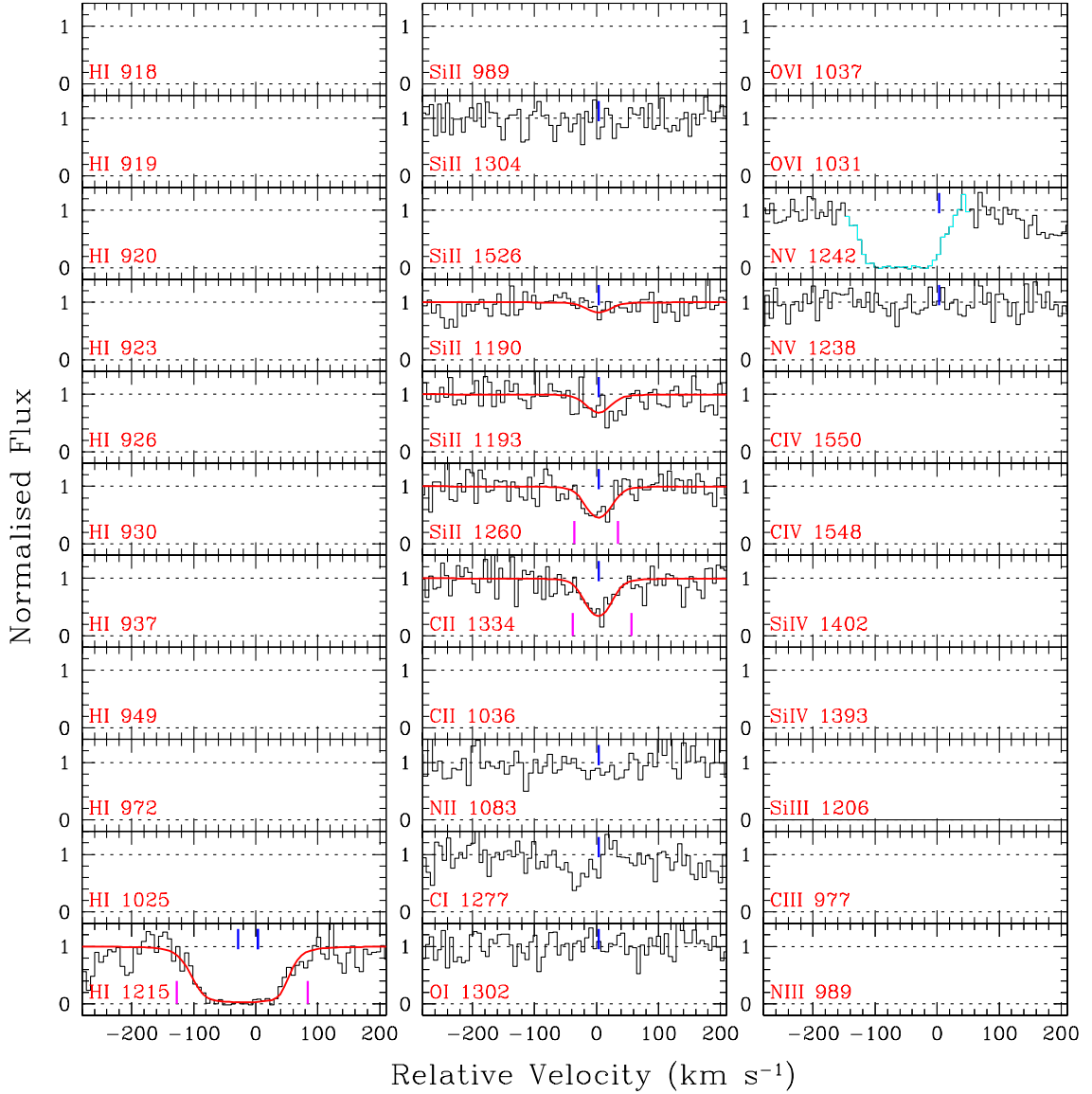
Figure C24. Similar to Fig. C1 but for the z_{abs} = 0.07407 system towards SDSSJ1214+0825. Only G130M data are available. Si III falls in the spectral gap. Lyα falls on top of galactic O I+Si II emission lines. We combined the "night-only" data separately for the Lyα absorption. The C II and Si II lines can be fitted simultaneously using only one component. The Lyα absorption require one more component at ~ -28 km s^{-1}. Note that for the component at 0 km s^{-1} we determine the maximum column density allowed by the profile to be log N(H I) = 15.0, using a Doppler-parameter that we obtained for the metal lines (b = 22 km s^{-1}). We assign a quality factor of Q = 1 for the N(H I) upper limit. Because of the lack of Si III coverage, we do not consider this system for PI modeling.

RXJ1230.8+0115 (z_{abs} = 0.00575)
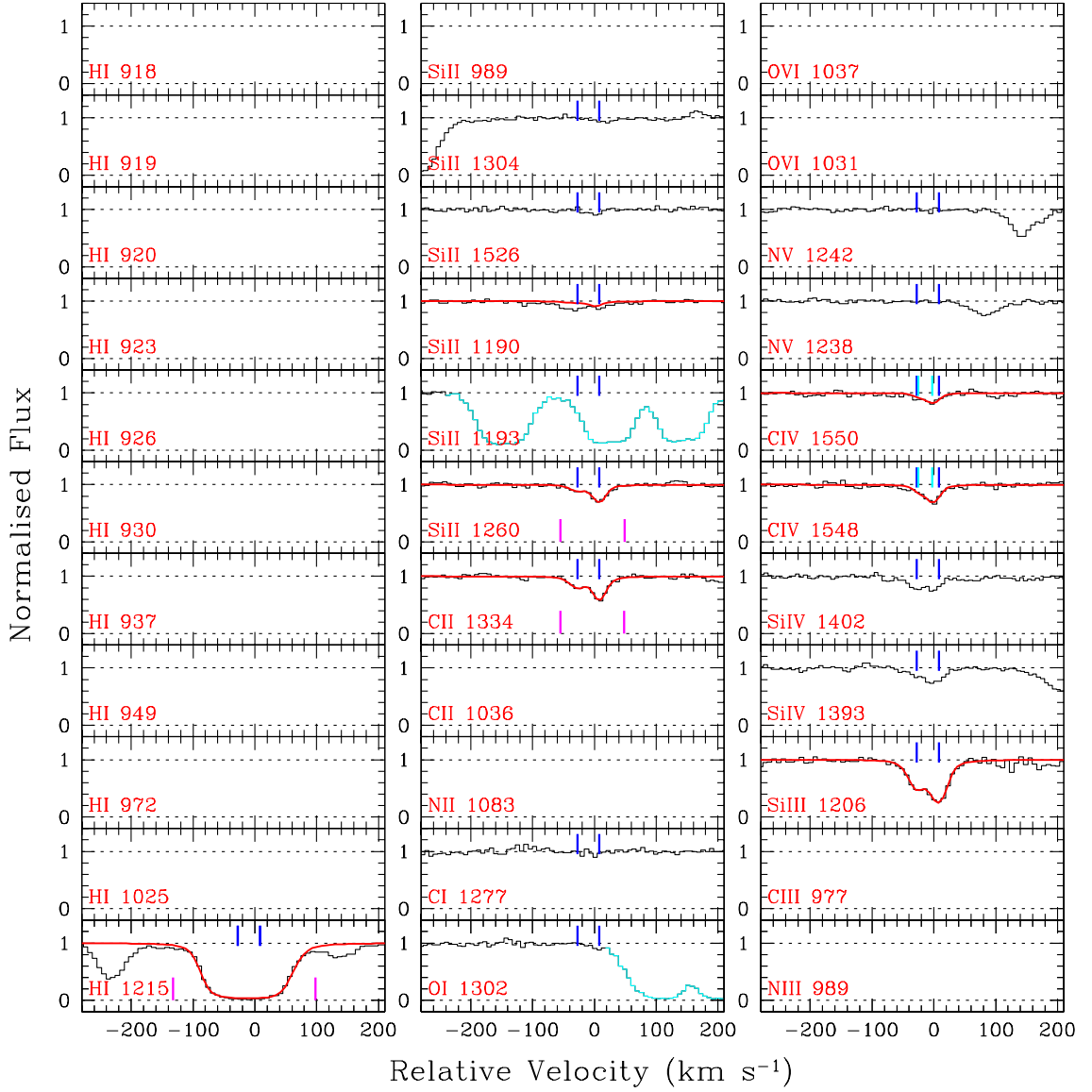
Figure C25. Similar to Fig. C1 but for the z_{abs} = 0.00575 system towards RXJ 1230.8+0115. Besides low-ions, high-ionization metal lines (C IV and Si IV) are also detected. The Si IIλ1260 and C IIλ1334 lines are ~ +6 and +4 km s^{-1} offset, respectively, with respect to the Si III line. The Si IIλ1193 line is lost due to the strong Galactic N Iλ1200 line. The strong line seen in the O I panel is actually Lyα absorption from the z_{abs} = 0.07770 system. A clear two-component kinematics is seen in the low-ionization metal lines. The metal lines are fitted simultaneously. The Lyα line is fitted using two components with redshifts locked at the values obtained from the metal line fitting. Due to the lack of unsaturated, higher order Lyman series lines, the estimated N(H I) is uncertain, and we assign a quality factor of Q = 1.
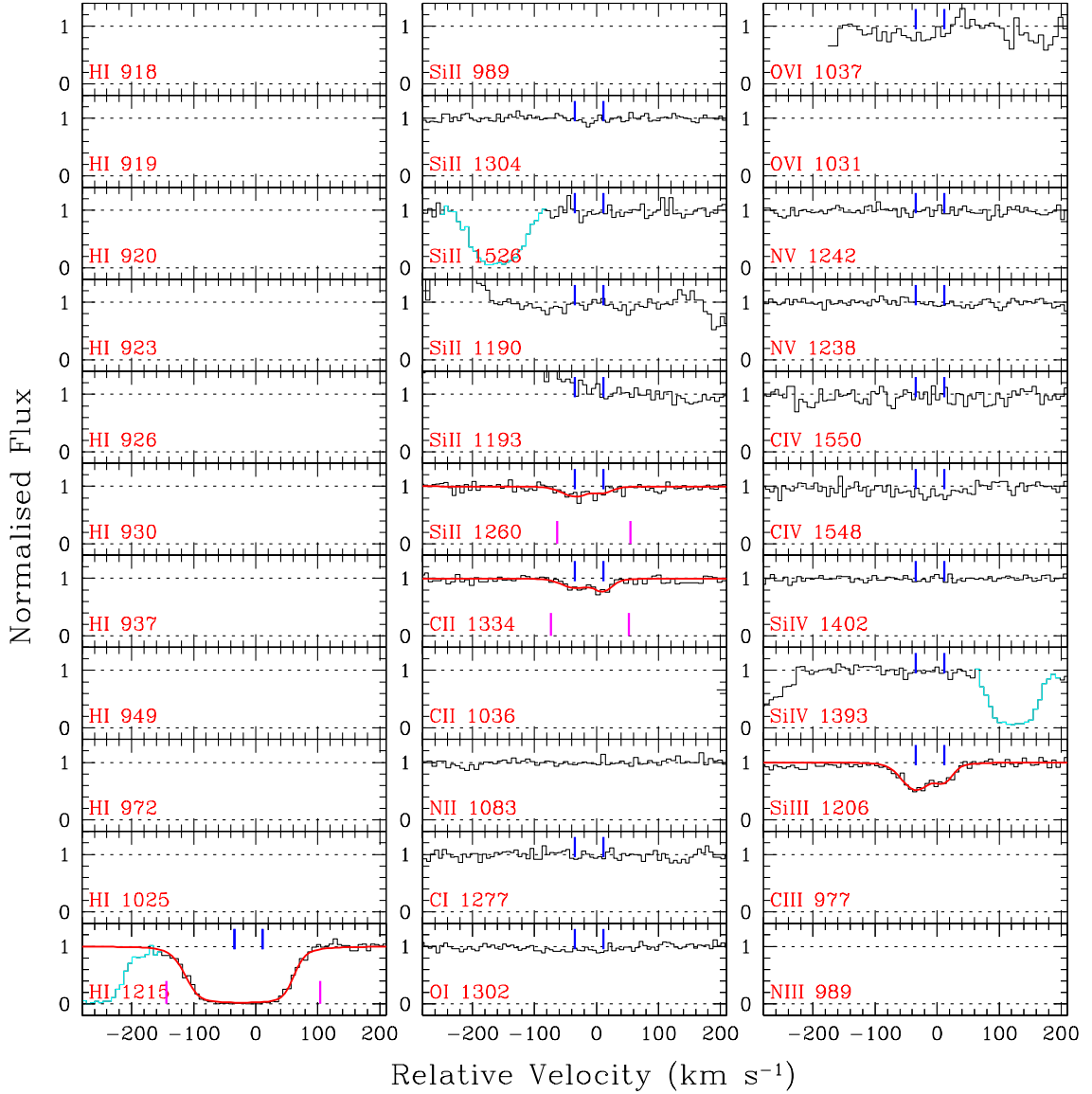
Figure C26. Similar to Fig. C1 but for the z_{abs} = 0.09495 system towards PKS 1302–102. The presence of high-ionization lines (e.g. C IV/O VI) is not obvious. A minimum of two components is required to fit the low-ionization lines. The C IIλ1334 line shows a velocity offset of $\sim$ −7 km s^{-1} with respect to the other lines. The metal lines (C II/Si II) are fitted simultaneously. We use two Voigt profile components to fit the Lyα absorption with line centroids locked at the values we obtained from the metal line fit. This is a partial-Lyman-limit system with log N(H I) = 16.88 ± 0.03 as measured by Cooksey et al. (2008) from the COG analysis of the full Lyman series lines using FUSE data. We adopted their N(H I) value and assign the highest quality factor of Q = 4.
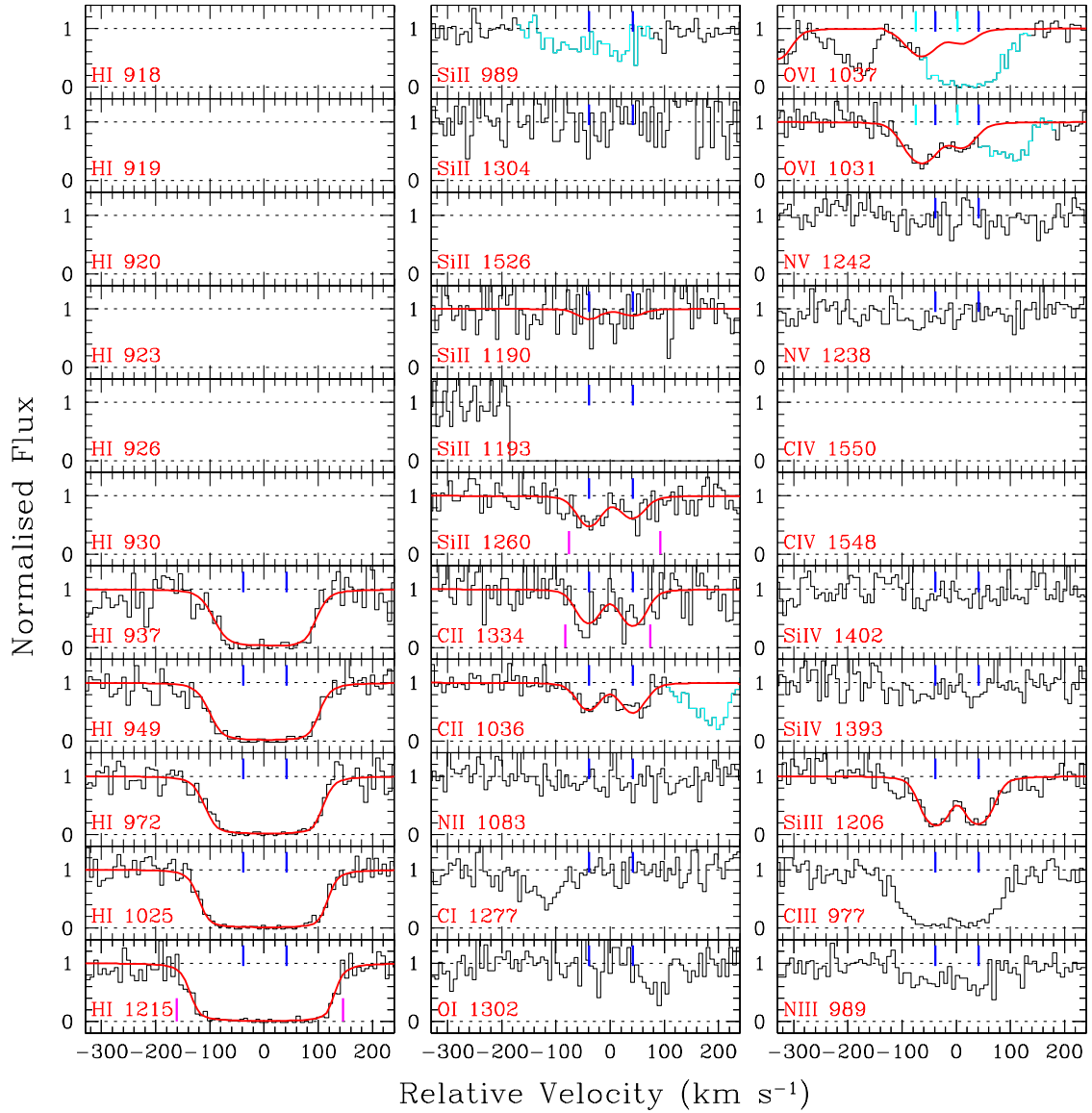
Figure C27. Similar to Fig. C1 but for the z_{abs} = 0.21451 system towards SDSSJ1322+4645. The Si IIλ1193 line falls in the spectral gap. The O VIλ1031 line is blended with the Galactic S IIλ1253 line, whereas, the O VIλ1037 line is lost in the strong Galactic Si IIλ1260 absorption. The spectrum is noisy. We used two components to fit the metal lines simultaneously. Both the C IIλ1334 and λ1036 lines are shifted by ∼ −10 km s^{-1} with respect to the Si III/Si II lines. We consider N(Si III) as upper limit since the Si III line is strongly saturated. The H Iλ937 line falls at the extreme blue end of the spectrum. The line require a velocity shift of ∼ +12 km s^{-1}. The Lyman series lines are also fitted simultaneously using two components by keeping redshifts locked but allowing b-parameters to vary. We, however, adopt the N(H I) value obtained from the Lyman limit break by Prochaska et al. (2017). We assign Q = 4 for this system.

SDSSJ1357+1704 (z_{abs} = 0.09784)
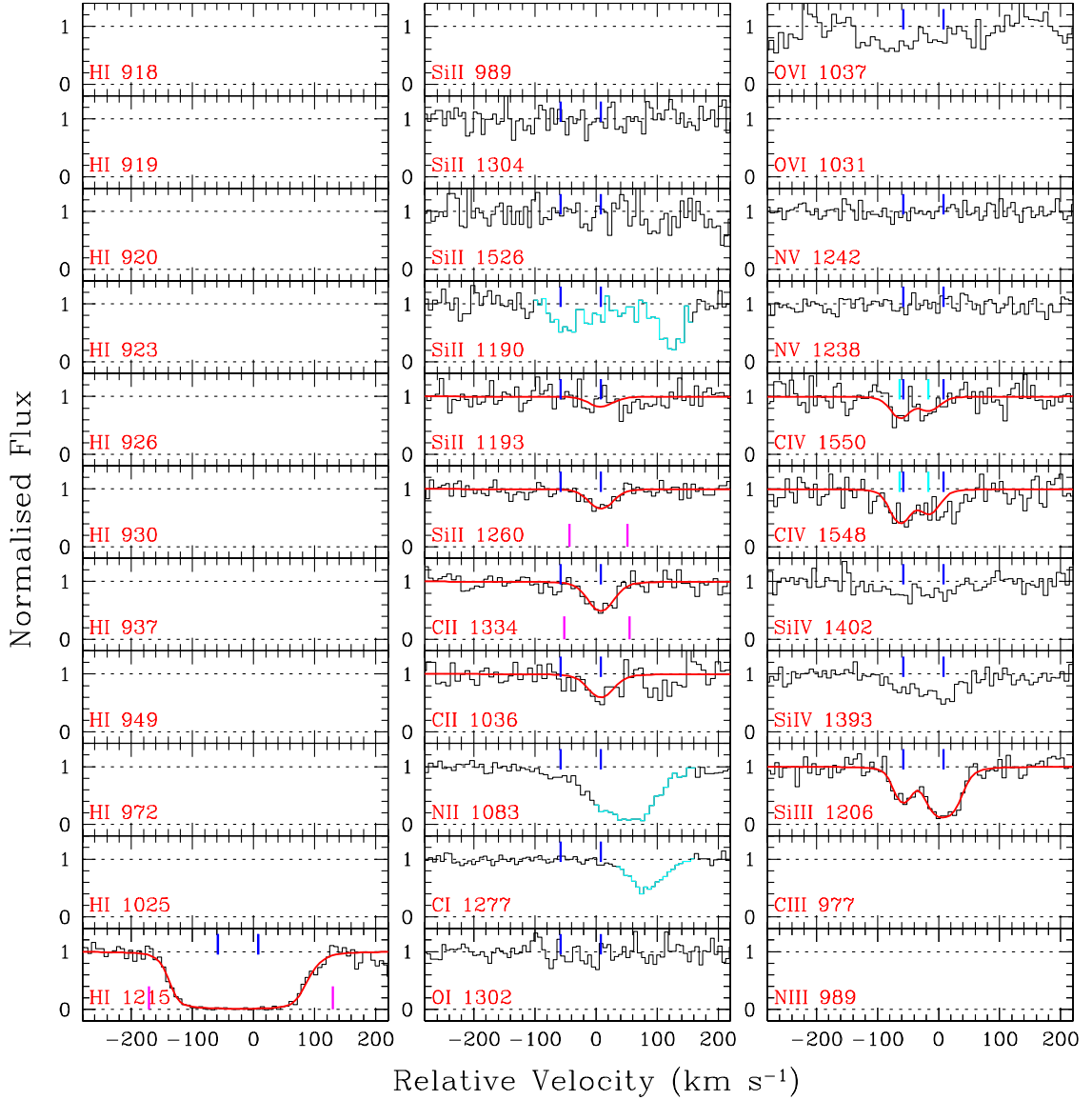
Figure C28. Similar to Fig. C1 but for the z_{abs} = 0.09784 system towards SDSSJ1357+1704. A two-component absorption kinematics, as seen in the Si III line, is also present in the Si IV and C IV doublets. However the N V doublet is not detected. The O VIλ1031 is not covered. Both C IIλ1036 and O VIλ1037 fall at the extreme blue end of the spectrum. We note that the C IIλ1036 (and hence the O VIλ1037) line require a velocity shift of $\sim$ +15 km s^{-1}. Although some absorption is seen in the O VIλ1037 panel, we could not confirm its association with this system. The N IIλ1083 line is blended with the Galactic Si IIλ1190 line. Note that the Si III component at $\sim$ 0 km s^{-1} is strongly saturated. The other component is not detected in the singly ionized carbon and silicon lines. The component at $\sim$ 0 km s^{-1} is fitted simultaneously keeping z and b-parameter tied. Due to saturation, we consider N(Si III) as a lower limit. The Lyα line is fitted with two components as seen in the Si III line. We note that the Lyα line is contaminated with Galactic C IIλ1334. Therefore, the N(H I) in this system is highly uncertain. We thus assign Q = 1 for this system.

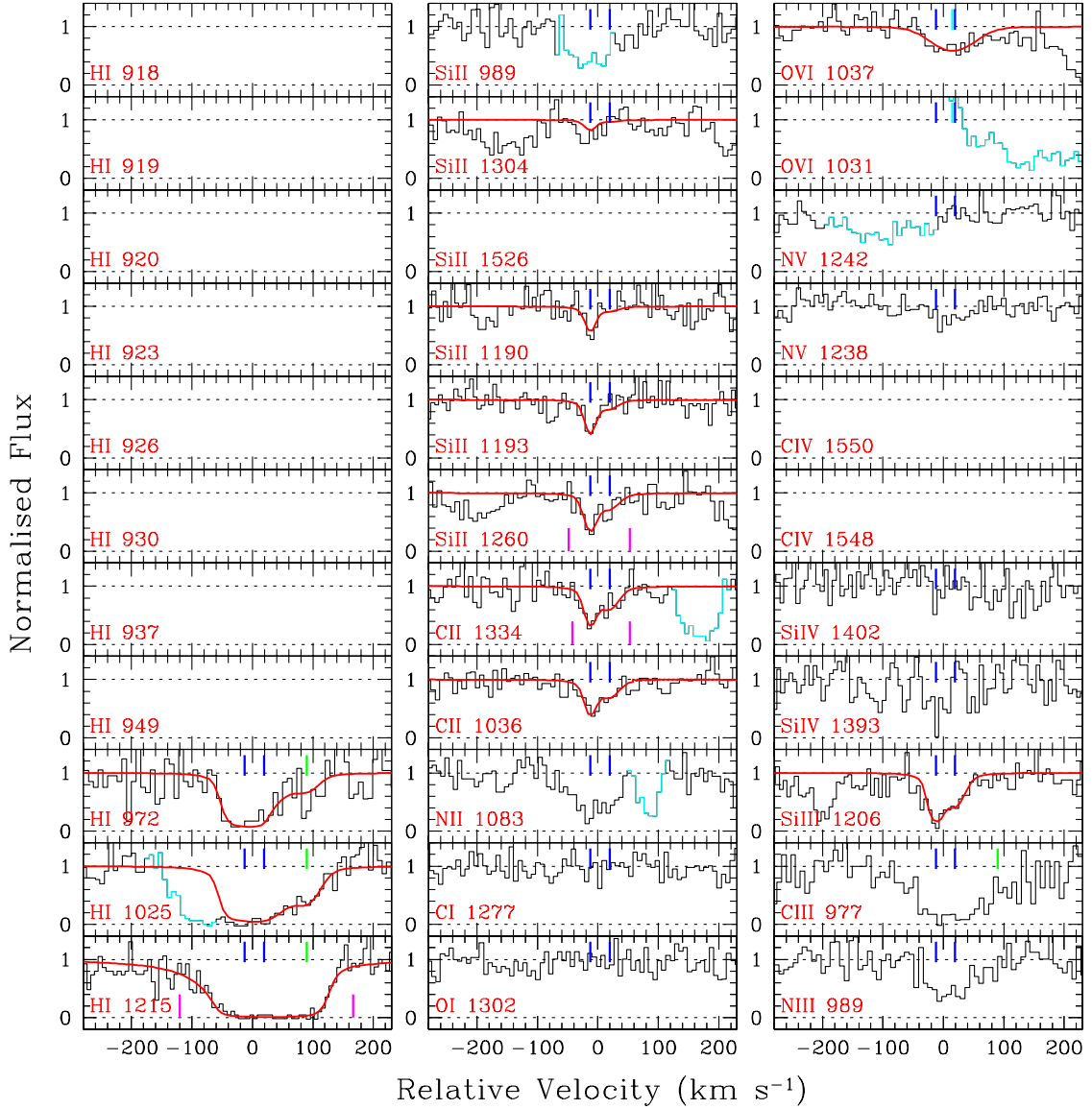SDSSJ1419+4207 (z_{abs} = 0.17885)

Figure C29. Similar to Fig. C1 but for the z_{abs} = 0.17885 system towards SDSSJ1419+4207. The Si III and Lyα lines fall at the red edge of the G130M grating data. Both these lines require a velocity shift of ~ -11 km s^{-1}. The Si III, C IIλ1036 and λ1334 lines show one narrow and one broad component. The presence of the broad component is not obvious in the Si II lines, particularly in the weaker lines. Metal lines are fitted simultaneously using two Voigt profile components. Note that we did not use the Si IIλ1304 and λ989 lines for fitting, because of blends. The Si IIλ989 is blended with the N IIIλ989 line. The blue wing of the Lyβ line is blended with the H Iλ937 line of another intervening system at z_{abs} = 0.28901. The narrow component is saturated in the C II and Si III lines. Thus, both N(C II) and N(Si III) are considered as lower limits. Besides the two components seen in the metal lines, the Lyman series lines require an extra component at $\sim +80$ km s^{-1}, as indicated by the green tick. This additional component may be present in the C III line. Recently, Prochaska et al. (2017) have published new N(H I) measurement for this system using the Lyman limit break seen in the G140L spectrum. We adopt their N(H I) value of $10^{16.63^{+0.09}_{-0.30}}$ cm^{-2} and assign Q = 4.

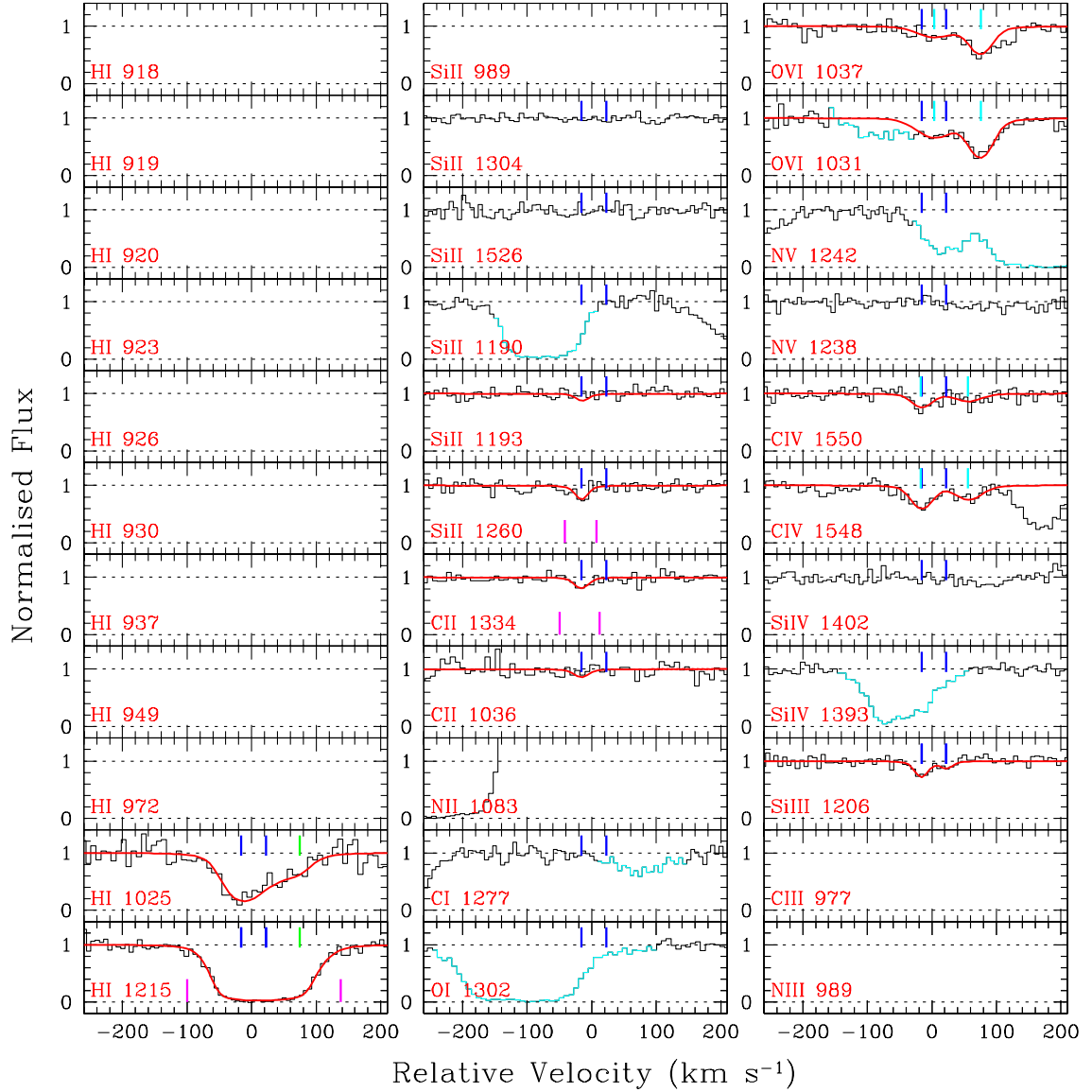## PG1424+240 (z_abs = 0.12126)

Figure C30. Similar to Fig. C1 but for the $z_{abs} = 0.12126$ system towards PG 1424+240. Two very weak components are detected in the Si III absorption. The weaker component at $\sim +20$ km s^{-1}, however, is not present in the C II/Si II absorption. We note that the C IIλ1334 line requires a ~ -10 km s^{-1} velocity shift. Metal lines are fitted simultaneously keeping z and b-parameters tied for the component seen in all three transitions. Besides the weak low-ionization metal lines, C IV and O VI are also detected in this system, but Si IV is not detected. The absorption seen in the Si IVλ1393 panel is the Lyα of the $z_{abs} = 0.28523$ system. The N IIλ1083 line is lost due to geo-coronal Lyα emission. In addition to the two low-ionization metal line components, one more component, shown by the green tick, is required to fit the Lyα and Lyβ lines simultaneously. This additional component is also evident in the O VI absorption. Since the Lyβ line is only mildly saturated we assign $Q = 3$ for this system.
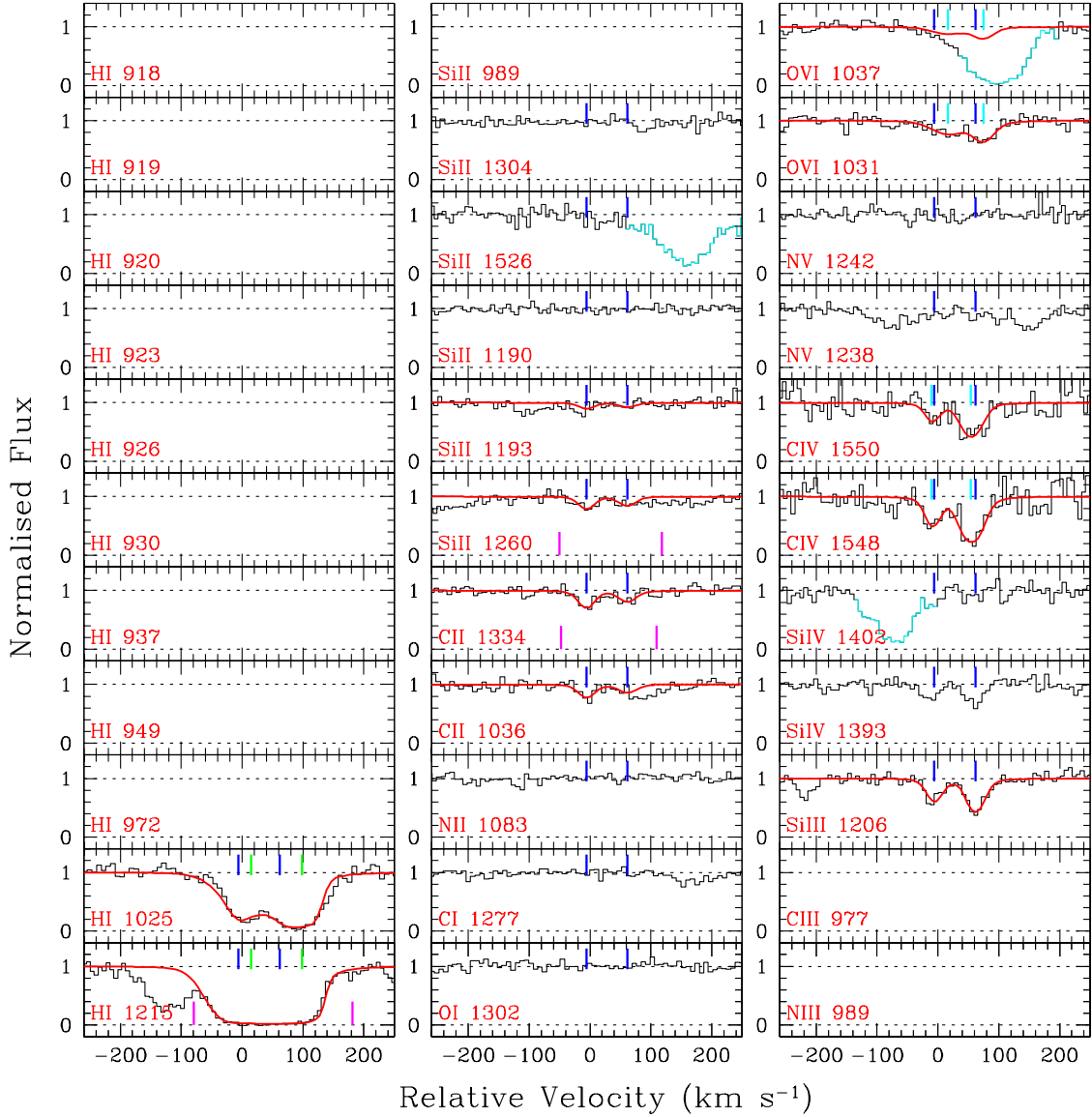
PG1424+240 (z_{abs} = 0.14683)

Figure C31. Similar to Fig. C1 but for the z_{abs} = 0.14683 system towards PG 1424+240. This is a very weak metal line system with high-ionization lines (Si IV, C IV, and O VI) detected. The O VIλ1031 line is blended with the Galactic Si IIλ1190 line. Two-component absorption kinematics is evident from the Si III line. Metal lines are fitted simultaneously by keeping z and b-parameters tied. Interestingly, the centroids of the metal line components are not centered around the Lyα and Lyβ lines. In fact, they are shifted towards the blue wings. This is not due to the wavelength calibration uncertainty since the C IIλ1036 (close to the Lyβ wavelength) and the Si III (close to the Lyα wavelength) lines are properly aligned. Consequently, the Lyα/Lyβ lines require two additional components, as marked by the green ticks, for an adequate fit. Since there are not enough Lyman series lines to constrain our four-component fit, we assign Q = 1 for this system.
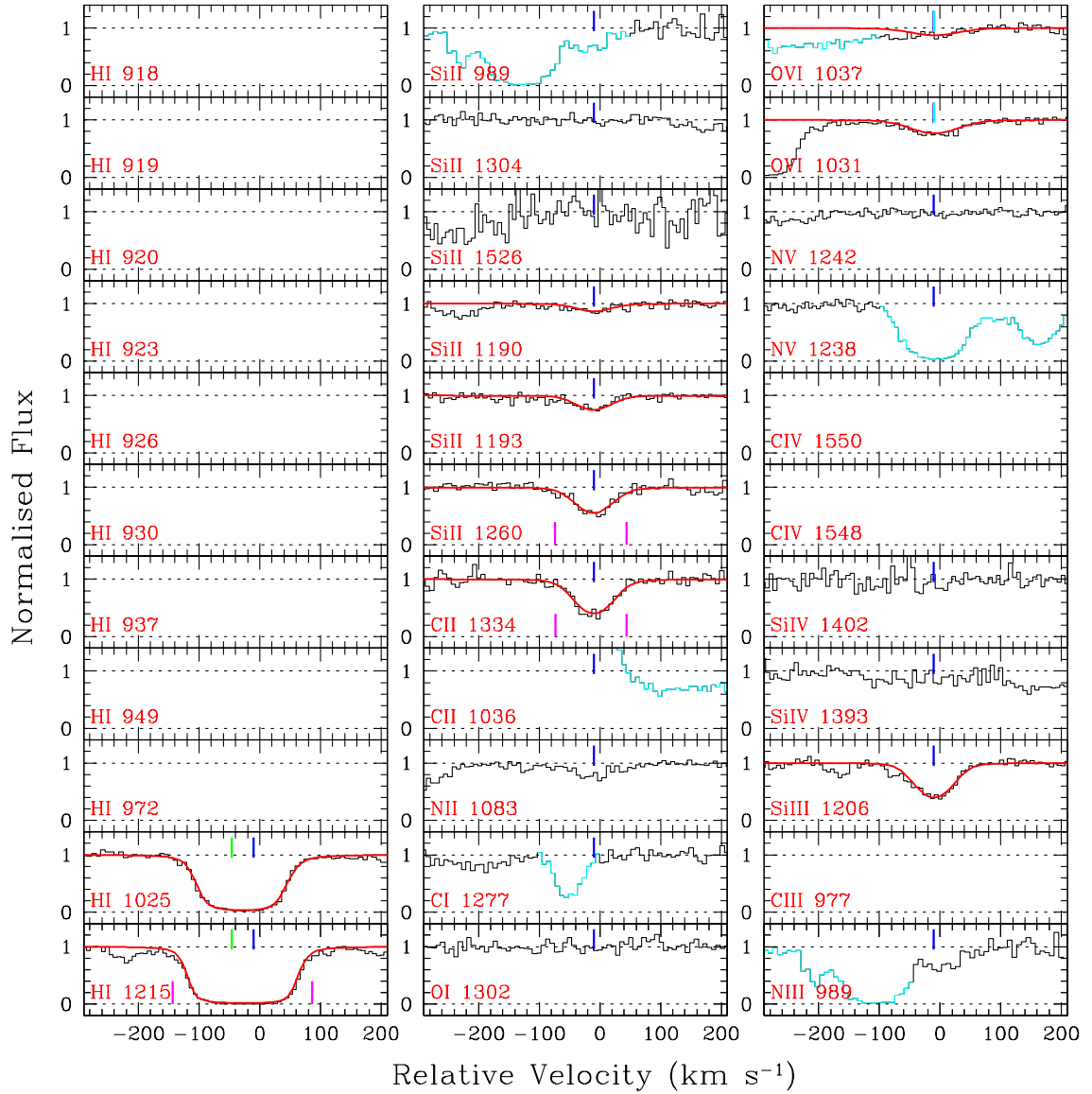
Figure C32. Similar to Fig. C1 but for the $z_{abs} = 0.17388$ system towards PG 1630+377. In addition to low-ionization metal lines, O VI is detected. The O VIλ1031 (and C IIλ1036) line is affected by Galactic Lyα absorption. The strong absorption seen in the N Vλ1238 panel is the Lyβ of the $z_{abs} = 0.41778$ system. We note that the Lyβ and O VI lines require a ~ -20 km s^{-1} velocity shift for properly alignment with the Lyα line. The metal lines are fitted simultaneously. The Doppler parameter of 35 km s^{-1} for our adopted single-component fit probably indicates the presence of multiple unresolved components. Two components are required to fit the Lyα and Lyβ absorption simultaneously. One of them is locked at the redshift corresponding to the low-ionization metal line component. The other component is possibly arising from the O VI bearing gas phase as indicated by the green vertical tick. Since both the Lyman series lines are heavily saturated we assign $Q = 1$ for this system.
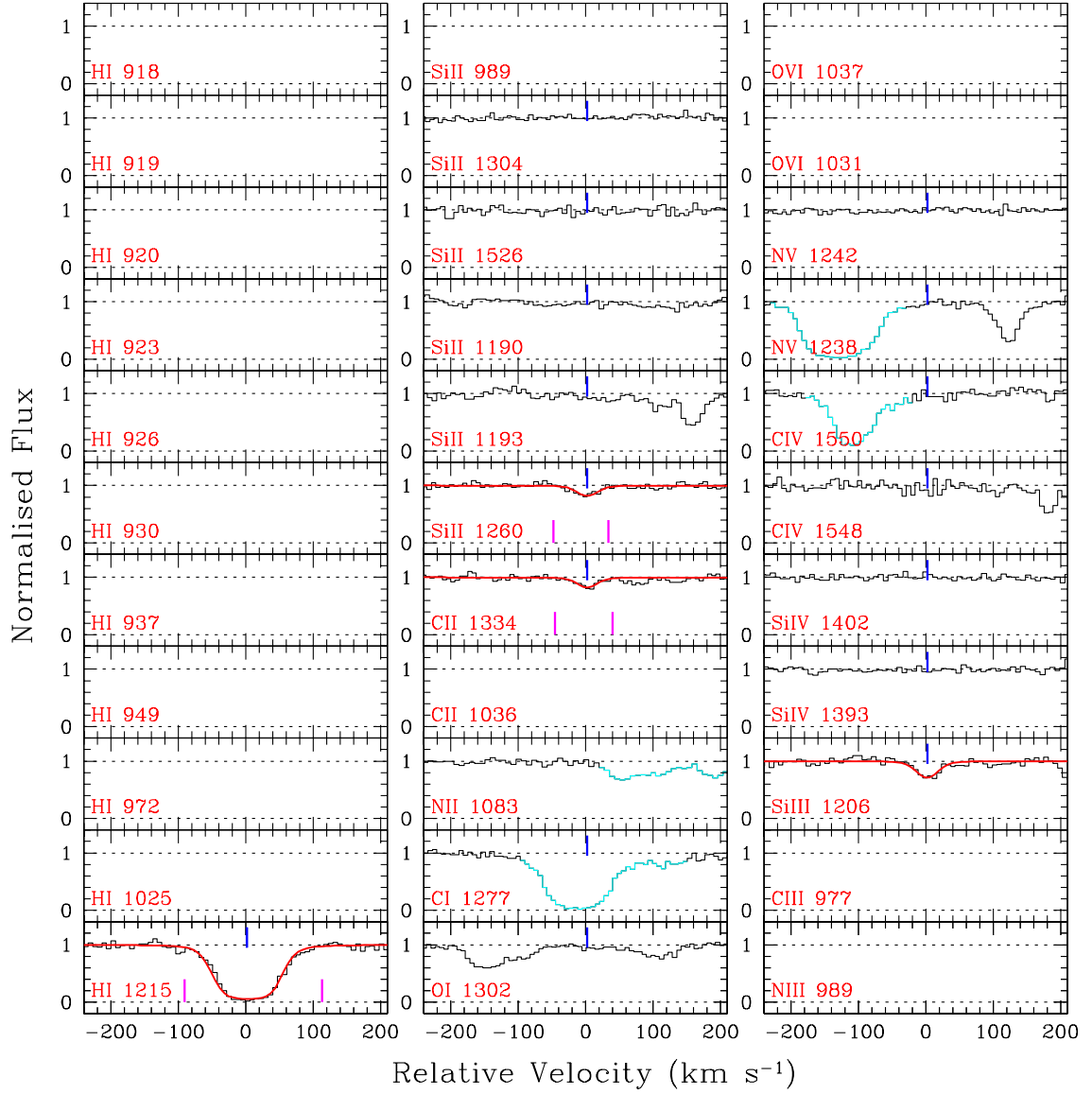
PHL1811 (z_{abs} = 0.07774)

Figure C33. Similar to Fig. C1 but for the z_{abs} = 0.07774 system towards PHL1811. The low ionization metal lines are very weak. No high ionization metal lines are detected. Using unsaturated higher-order Lyman series lines (up to H Iλ923) covered by FUSE data and Lyα from STIS data, Lacki & Charlton (2010) have derived log N(H I) = 16.00 ± 0.05. Here we adopt their value and assign Q = 5 for this system.
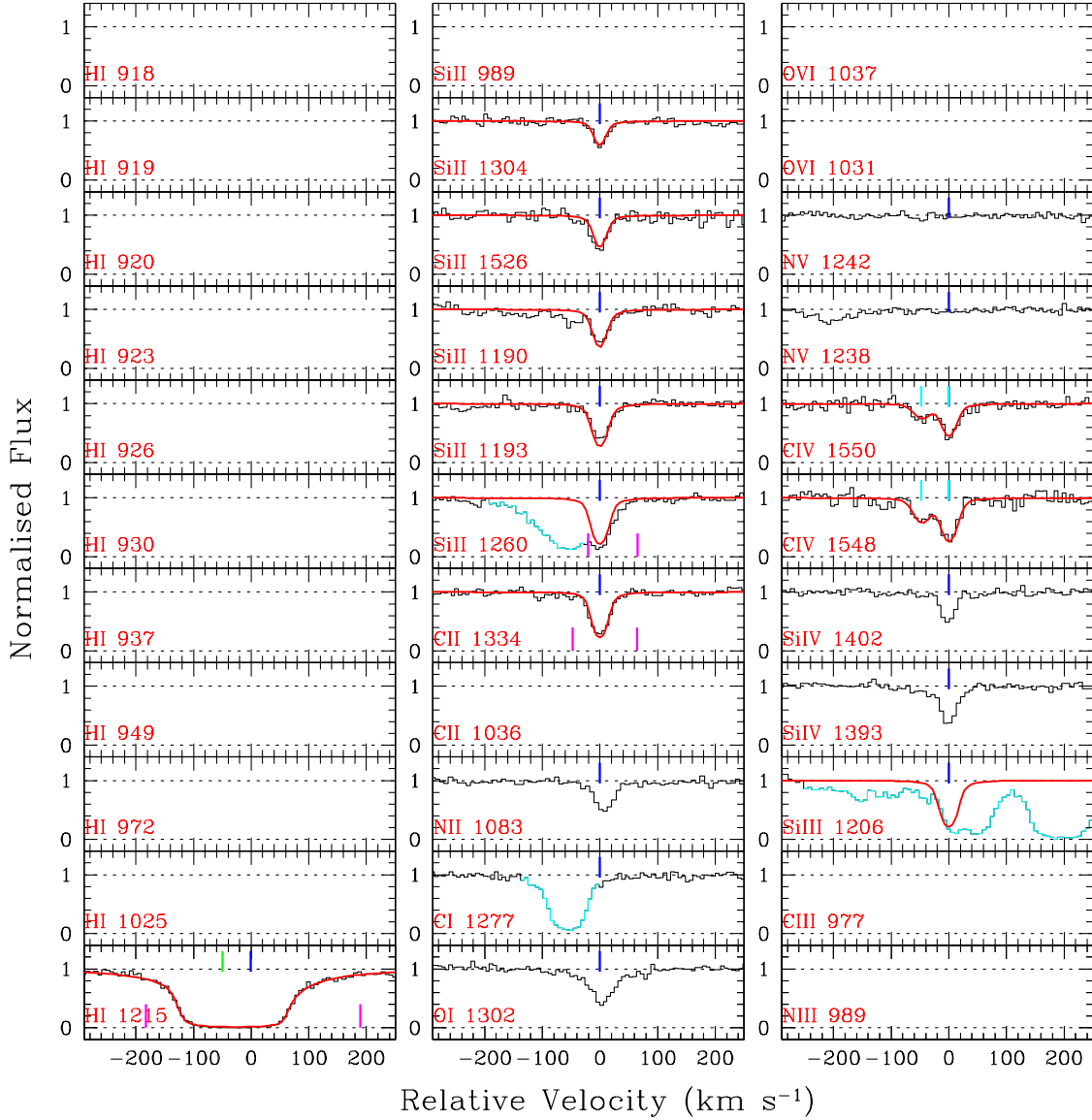
PHL1811 (z_{abs} = 0.08091)

Figure C34. Similar to Fig. C1 but for the z_{abs} = 0.08091 system towards PHL1811. The Si III line is blended with Galactic Si IIλ1304. The Si IIλ1260 line is blended with the Lyα of the z_{abs} = 0.12051 system. The single component C II and Si II lines are fitted simultaneously. We did not use the Si IIλ1260 line for fitting because of the blend; but the model profile corresponding to the best fitting parameters is shown. The C IIλ1034 line is heavily saturated. The Si IIλ1193 also shows an unresolved saturation effect. However the weaker, unsaturated Si IIλ1304 line gives an accurate N(Si II) estimate. Due to a severe blend in the Si III line we use the best fitting metal line parameters and estimate the maximum N(Si III) allowed by the observed profile. In addition to the component seen in the low ionization metal lines, Lyα requires another component at ~ -50 km s^{-1}. This component is seen in the high-ionization C IV lines and is indicated by the green ticks. A strong Lyman limit break corresponding to this system is seen in a FUSE spectrum (see Fig. 1 of Jenkins et al. 2003). Ignoring the blue component Jenkins et al. (2005) have derived log N(H I) = 17.98 ± 0.05 for the red component at 0 km s^{-1}. It is consistent with our measurement (i.e. log N(H I) = 17.94 ± 0.07) for that component. We therefore assign Q = 4 for this system.